ABSTRACT

Title of Document: ANALYSIS OF DRUG DELIVERY IN THE EYE USING MAGNETIC RESONANCE IMAGING

Heekyong Stephanie Kim, Doctor of Philosophy, 2007

Directed By: Associate Professor Nam Sun Wang, Department of Chemical and Biomolecular Engineering

With the rapid increase in the elderly population, the number of Americans afflicted with vision impairment due to ocular disease is projected to rise substantially by the year 2020. Ocular disorders are becoming a major public health problem, and efforts have increased in recent years to develop methods of efficient drug delivery. Currently, the most effective method for treating serious ocular disorders is to inject drug solutions directly into the vitreous. However, injecting in this manner carries a high risk of severe side effects. As a safer alternative, researchers in recent years have been investigating transscleral drug delivery, in which the drug is administered to the outer coat of the eye. Various methods of transscleral drug delivery have been proposed, but it is still clinically not as effective as intravitreal drug delivery. In order to design improved transscleral drug delivery systems, the ocular barriers to drug transport must be accurately understood.

While various barrier types have been identified in the eye, the significance and contribution of individual barriers have not been investigated and are still widely unknown. A reason for this lack of understanding is due to the inability to acquire concentration measurements in the eye *in vivo*. In this study, magnetic resonance imaging (MRI) was employed to obtain drug concentration measurements *in vivo* after transscleral drug delivery.

To address the current needs of the ocular drug delivery community, several goals have been achieved in this work: (1) to evaluate transscleral drug delivery *in vivo* using MRI, (2) to assess MRI as a technique for evaluating drug delivery in the eye, and (3) to better understand the significance of individual barriers in the eye by quantitatively analyzing experimental (MRI) data and by pharmacokinetic modeling. While encompassing many advantages, it is found that MRI has limitations in spatial and temporal resolution that may restrict its use in measuring parameters with low sensitivity. However, the MRI results in parallel with analysis from the pharmacokinetic model give new insight into the barriers to drug transport in the eye.

ANALYSIS OF DRUG DELIVERY IN THE EYE USING MAGNETIC RESONANCE IMAGING

By

Heekyong Stephanie Kim

Dissertation submitted to the Faculty of the Graduate School of the
University of Maryland, College Park, in partial fulfillment
of the requirements for the degree of
Doctor of Philosophy
2007

Advisory Committee:
Professor Nam Sun Wang, Chair
Dr. Robert J. Lutz
Professor Srinivasa R. Raghavan
Professor Yang Tao
Professor Evanghelos Zafiriou

Dedication

To those who have faithfully supported and encouraged me through the entire course of my thesis work by covering every detail in prayer.

Acknowledgements

I have had the honor and privilege to work with many advisors and collaborators from the University of Maryland and the National Institutes of Health, all of whom have contributed to the successful completion of this dissertation. I am grateful for the support from my advisor, Dr. Nam Sun Wang, who graciously gave me this opportunity to pursue a research project at the NIH, which has been an invaluable experience. I also thank Dr. Michael Robinson for being a mentor and for teaching me the current needs in ocular drug delivery. Dr. Karl Csaky has contributed significantly to this project financially and also by providing strong guidance and direction from an ophthalmology viewpoint.

I also appreciate the support from the senior scientists at the Drug Delivery and Kinetics Resource within the National Institute of Biomedical Imaging and Bioengineering at the NIH. Dr. Robert Lutz has been a wonderful research advisor and I am grateful to have been able to work under his supervision as I have learned how to approach drug delivery and pharmacology as a chemical engineer. I am also thankful for Dr. Peter Bungay, Dr. Robert Dedrick, and Dr. Paul Morrison, who have always been extremely kind and available to help with my questions and interpretation of data. I thank Dr. Bungay especially for his direction and guidance in pharmacokinetic modeling.

I would also like to acknowledge the technical assistance I have received from Dr. Craig Galban and Dr. Martin Lizak. Craig has been an incredible help in processing and analyzing image data, and Marty has been very kind in helping us

during our MR imaging sessions. I would also like to thank the staff at the animal MRI facility at the NIH, as I have greatly appreciated their eager willingness always to help. I thank Dr. Ginger Tansey and the veterinary technicians: Denise Parker, Mark Lawson, Carrie Silver, Beth Case, Mark Szarowicz and Chris Hillman for their flexibility and faithful support and care of our rabbits. They have always been very willing to assist with our animal experiments, which has been a tremendous help.

I am also thankful for the other members of Wang lab, especially for offering their ideas and suggestions for my research. I have thoroughly enjoyed our lab meetings, which have helped me broaden my knowledge of current chemical engineering research and have also refined my critical thinking skills as a scientist.

Finally, I would like to thank the members of this dissertation committee for their input and recommendations from the research proposal, which has enabled greater focus and direction for this dissertation.

Table of Contents

List of Tables

List of Figures

Chapter 1: Introduction

Due to the rapidly increasing elderly population, ocular disorders leading to vision impairment is becoming a major public health problem [1]. The number of Americans diagnosed with age-related macular degeneration (AMD), a disease responsible for the majority of cases of blindness, will increase by 50% to 2.95 million in the year 2020 [2]. AMD and other leading causes of vision loss such as diabetic retinopathy, endophthalmitis, and retinitis pigmentosa are currently difficult to treat [3,4] because they affect tissues in the posterior segment of the eye, such as the choroid and retina (Fig. 1-1). Drug delivery to the posterior segment has remained a challenge as most drugs fail to reach therapeutic levels in this region after topical and systemic administration.

As ocular disorders become more prevalent, the need for more effective therapies and treatments will increase. Many researchers in ophthalmology have been interested in developing new methods for more effective drug delivery to the eye. While numerous novel drug delivery systems have been proposed, many are unable to deliver therapeutic drug levels to target ocular tissues in a safe and minimally invasive manner.

The amount of drug that is delivered to a desired area can be affected by factors such as drug transport barriers and clearance mechanisms. Despite the numerous efforts in the development of new ophthalmic drug delivery systems, the ocular elimination mechanisms and the rate of drug clearance are largely unknown. By understanding how drugs are eliminated in the eye, the design of drug delivery

systems can be improved with greater efficiency. The aim of this research is to investigate how drugs are eliminated in the eye after ocular drug delivery by using magnetic resonance imaging and drug transport modeling.

1.1. Eye Anatomy

The eye is composed of two tunics that envelop the anterior and posterior segments. The anterior segment is capped by the cornea, and the posterior segment is bound by the sclera, choroid, and retina (Fig. 1-1). These thin tunics envelop the vitreous body which is a gelatinous mass that occupies most of the ocular volume. The sclera is known as the white coat of the eye which is avascular and is primarily composed of collagen fibrils. The choroid is a highly vascular layer which possesses the fastest rate of blood flow in the entire human body. Blood flow through the choroid provides necessary nutrients to the underlying retinal cells and also acts as a sink for heat dissipation. The retina is a multi-cellular layer responsible for many of the visual processes of the eye. The macula is an oval region of the posterior retina which is specialized for central vision, and is a common target tissue in ocular drug delivery.

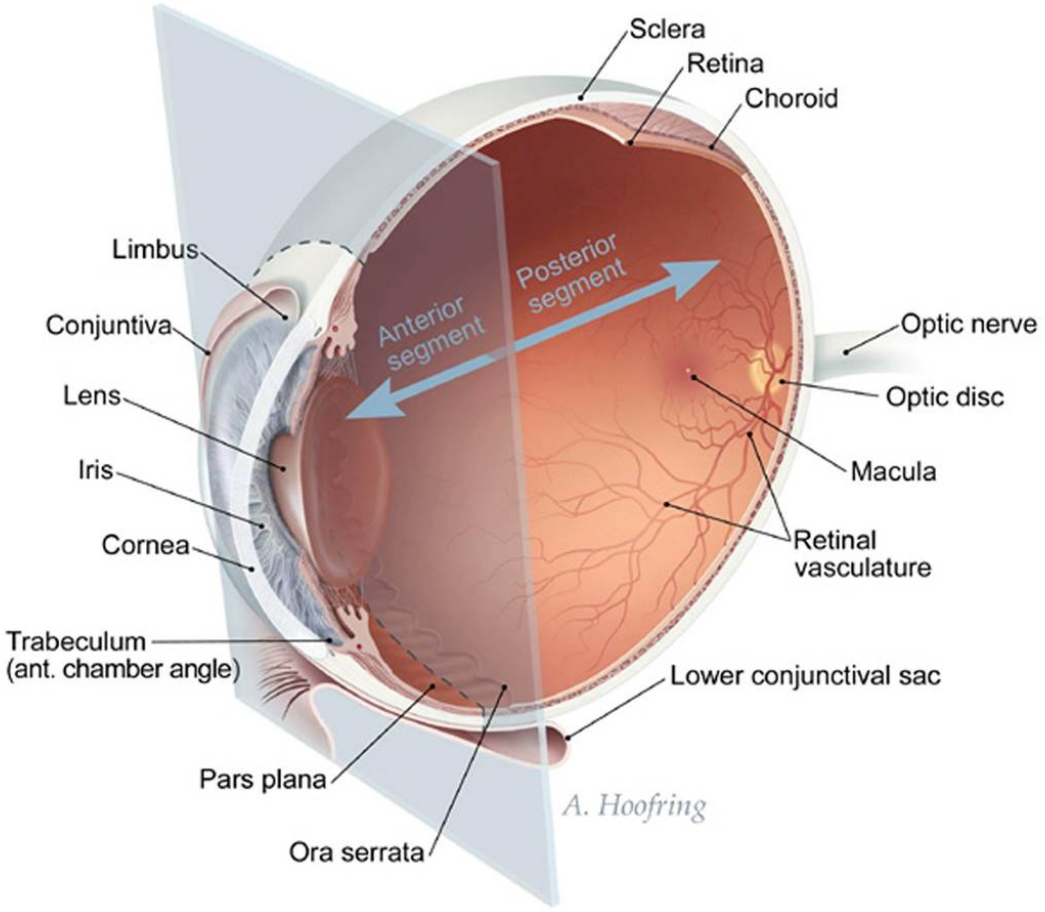

Figure 1-1. The anatomy of the human eye.

From reference [5].

The conjunctiva is a thin, opaque, filmy tissue that extends up to the equator of the posterior segment and folds up to line the inside of the upper and lower eyelids, forming the upper and lower conjunctival sac. It is a vascular tissue that has an extensive network of blood and lymphatic vessels.

1.2. Drug Delivery Methods for Posterior Segment Disorders

Four methods of drug delivery have been investigated for treatment of posterior segment disorders: topical, systemic, intravitreal, and periocular [3]. Figure 1-2 illustrates some of these drug delivery methods. While topical eye drops (Figure 1-2A) are easy to use and are non-invasive, less than 3% of the instilled drug has been found to penetrate the anterior segment due to low retention times in the conjunctival sac and rapid drainage from the ocular surface [6]. Topical eye drops are the most common method of ophthalmic treatment, but they are typically used in treating anterior disorders since drug concentrations in the posterior segment are typically below therapeutic levels [7]. Systemic injections of drugs also yield low drug concentrations in the eye because of the blood-ocular barriers that restrict the movement of drugs from the bloodstream into the surrounding tissues [8,9]. Unfavorable side effects usually result from toxicity because high systemic doses are required to achieve therapeutic levels in the eye. Intravitreal injections (Figure 1-2G) and implants (Figure 1-2F) can be administered directly into the vitreous to allow higher amounts of drug to reach the posterior tissues of the eye but the invasive surgical procedure may produce severe side effects such as retinal detachment, hemorrhage, and cataracts [3]. As a safer alternative, periocular delivery methods can be used, which require administering drugs to the outer tissues of the eye. This is typically accomplished by injecting (Figure 1-3) or implanting (Figure 1-2C) drugs underneath the conjunctiva, forming a subconjunctival drug depot. The elastic nature of the conjunctiva allows a localized depot to form after a drug solution injection, offering the potential for long-term sustained release.

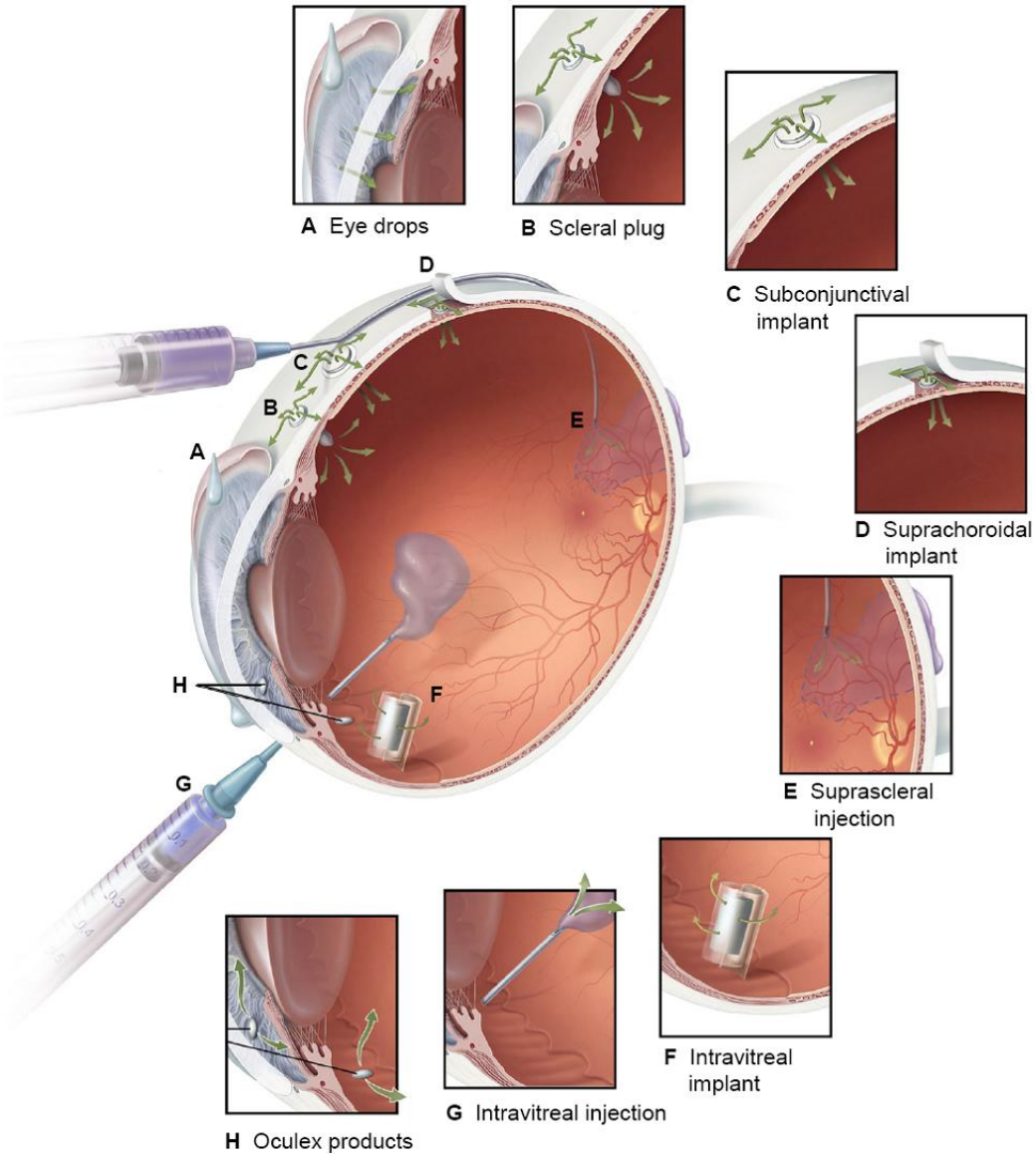

Figure 1-2. Methods of ocular drug delivery.

From reference [10].

Subconjunctival injections are a form of transscleral delivery, a method which requires drugs to penetrate across the sclera in order to reach the underlying target tissues such as the choroid, retina and vitreous [4]. Transscleral delivery is emerging

as an attractive method for ocular drug delivery because it is a less invasive and a safer alternative to other delivery methods, and also permits localized, sustained-release delivery of drugs to the posterior segment of the eye [3]. Subconjunctival injections of celecoxib, for example, yields greater delivery to the retina than systemic administration [11].

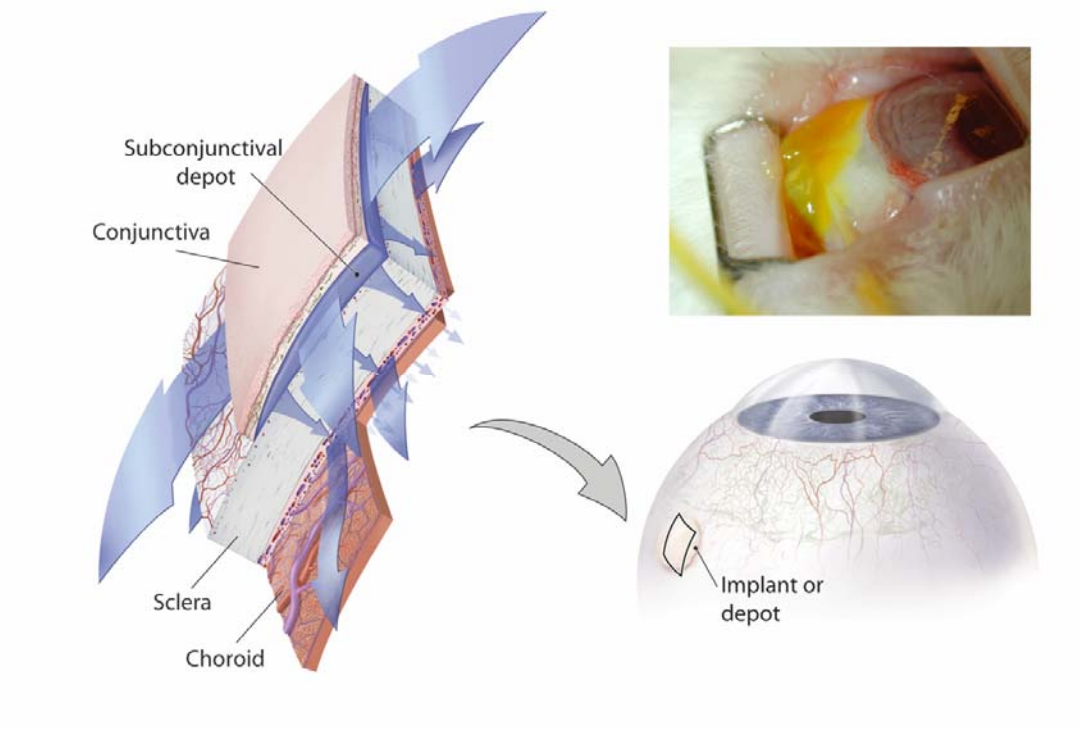

Figure 1-3. Subconjunctival Delivery.

Left: Anatomy of tissues involved during transscleral delivery. Top right: Photograph taken after subconjunctival injection in an albino rabbit eye. The conjunctiva is an elastic tissue that permits the formation of a local depot.

Methods of transscleral drug delivery range from drug solution injections to polymeric implants. Microparticles administered subconjunctivally have been formulated for the sustained release of drugs such as celecoxib [12] and budesonide [13] to maintain therapeutic retinal levels. Injectable gels with sustained release of drugs have been administered subconjunctivally [14,15]. Polymeric implants have been constructed as subconjunctival [16], episcleral [17], and intrascleral [18,19] discs. Osmotic pumps have also been utilized to intrasclerally infuse continuous amounts of drug into the eye [20,21].

Although there has been great interest in the development of transscleral drug delivery systems, transscleral delivery is still not as clinically effective as intravitreal delivery in treating retinal disorders [22,23]. The only treatments available for AMD (Lucentis, Avastin, and Macugen) are currently administered as intravitreal injections. During transscleral delivery, drug molecules must cross several layers of tissue before reaching the vitreous (Figure 1-4), and a very steep concentration gradient from the sclera to the vitreous is usually established. This steep gradient is due to barriers in transport that hinder drug molecules from successfully reaching the inner ocular tissues.

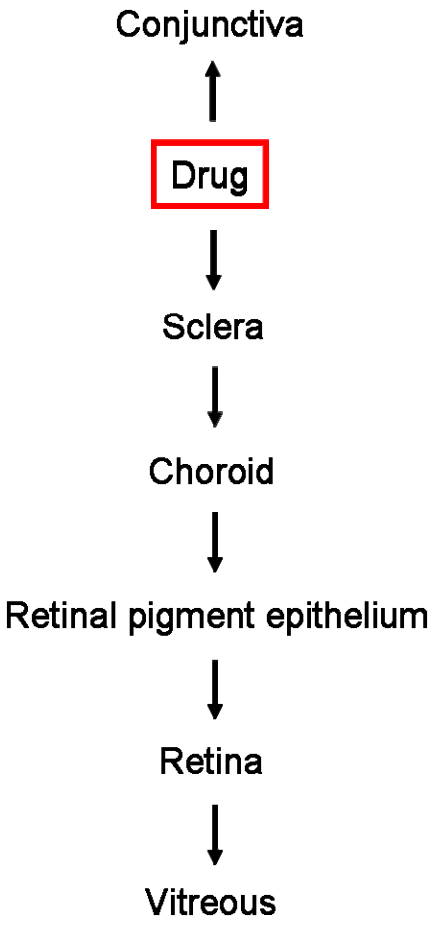

Figure 1-4. Penetration pathway of drugs after transscleral delivery.

1.3. Transport Barriers during Transscleral Drug Delivery

Three types of barriers hindering transscleral drug delivery have been described in the current literature: static, dynamic, and metabolic [24]. Static barriers are created by the structural features of the ocular tissues which pose a physical barrier to drug diffusion (Figure 1-5). Dynamic barriers are active clearance mechanisms of drug elimination through blood and lymphatic vessels, bulk fluid flow due to intraocular drainage, and also include the transporter proteins of the retinal

pigment epithelium (RPE). Metabolic barriers also exist in the eye, and may reduce drug penetration to the retina by degradation.

1.3.1. Static Barriers

The sclera is a matrix composed of proteoglycans and collagen fibers that can hinder the penetration of drug molecules through the tissue. The choroid and the underlying Bruch's membrane, a complex composition of lipids and lipoproteins, can also impede the movement of drug molecules. The RPE provides a cellular barrier with tight junctions, effectively reducing paracellular transport.

The diffusional barrier of these tissues to drug molecules has been most widely studied *ex vivo* by using the two-chamber Ussing type apparatus (Figure 1-6). The Ussing system measures the permeability of solutes across a membrane mounted between the two chambers. Permeability is reported in units of cm/s, and can be understood as the velocity of the molecule diffusing across a tissue in response to a concentration gradient [25].

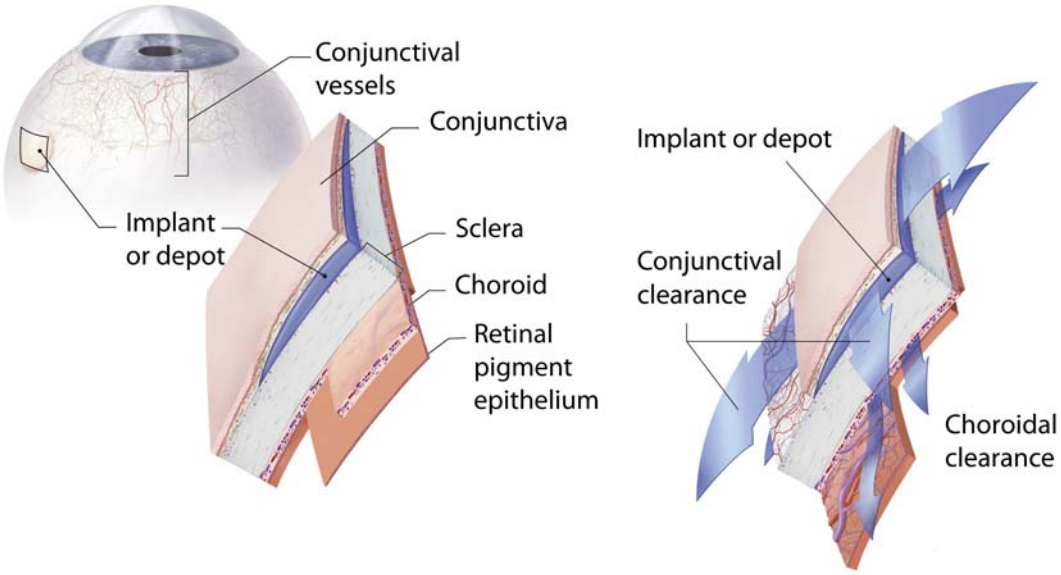

Figure 1-5. Static and dynamic barriers of the eye.

The static barriers (sclera, choroid, and retinal pigment epithelium) present during transscleral drug delivery. Clearance pathways present in the conjunctiva/episclera and choroid during transscleral delivery.

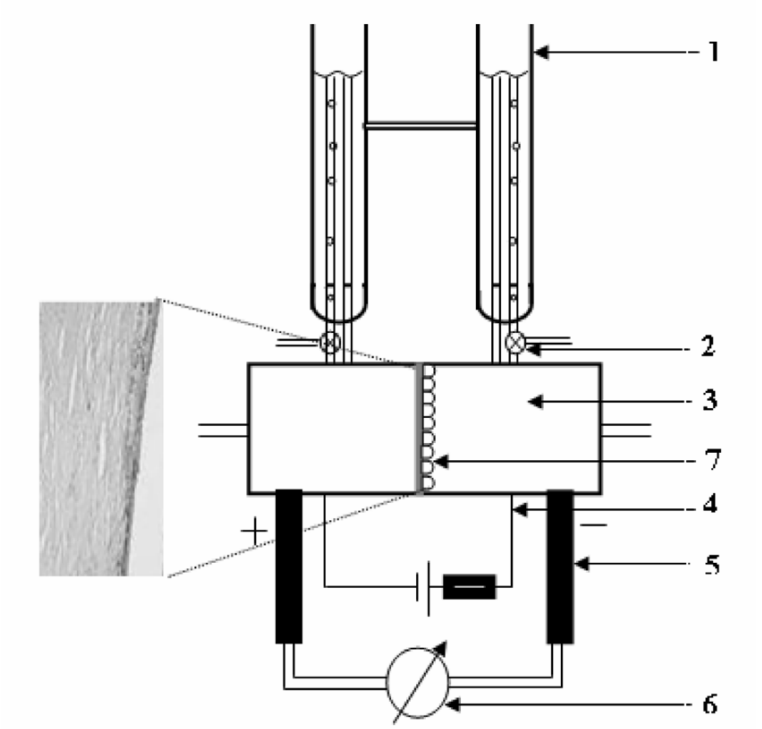

Figure 1-6. The two-chamber Ussing apparatus.

From reference [26].

Several factors influence the tissue permeability of molecules. Tissue permeability has been shown to have a strong dependence on molecular weight, with larger molecules having lower permeabilities than smaller molecules in the sclera [27-31]. Permeability has been shown to decrease roughly exponentially with molecular radius in the sclera [28,32], choroid and RPE [33]. Table 1-1 summarizes the effect of various physicochemical properties of solutes on the permeability of ocular tissues. The permeability of the Bruch's membrane and choroid (BC) has always been studied in tandem due to the difficulty of separating the two tissue layers [34]. The RPE, however, can be easily removed and its permeability characteristics

are understood by comparing tissue permeability values with and without RPE removal.

Increase in solute lipid solubility was also shown to lower scleral permeability [26,35,36], as hydrophilic compounds may diffuse through the aqueous media of proteoglycans in the fiber matrix pores more easily than lipophilic compounds [35]. Increasing solute lipophilicity also decreases the permeability of the choroid [36] but increased the permeability of the RPE [33]. This suggests that the permeability of the RPE increases with increasing lipophilicity. Solutes with negative charges have been found to have higher permeabilities than those with positive charges in sclera [36,37]. Proteoglycans in the sclera are negatively charged [38], which may contribute to the binding of positively charged molecules.

The *ex vivo* permeability of the sclera has been extensively reported in the literature. The permeability for a number of molecules has been measured including dextrans [30] and PEG molecules [29] of various molecular weights, antibiotics [39], oligonucleotides [40], retinal anti-angiogenic molecules [41], and lipophilic compounds [35,36]. Permeability studies of the Bruch's membrane-choroid and the RPE, however, are not as extensive as that of the sclera. Additional permeability studies are necessary to establish the relative resistance of the BC and RPE for a variety of solutes.

Physicochemical property	Sclera	BC	BC-RPE
Molecular radius	Exponential decrease with increasing radius [28,32]	Decrease with increasing molecular weight [42]	Exponential decrease with increasing molecular radius [33]
Lipophilicity	Decrease with increase in lipophilicity [26,35,36]	Decrease with increase in lipophilicity [36]	Increase with increase in lipophilicity [33]
Charge	Increase with negatively charged solutes [36,37]	Increase with negatively charged solutes [36]	Not studied

Table 1-1. Summary of effects on *ex vivo* permeability in ocular tissues with various solute physicochemical properties.

Most studies on transport barriers affecting transscleral drug delivery have focused on the determination of permeability values of ocular tissues. Permeability values are helpful for comparing diffusional resistances of one tissue to another and can also be used to calculate the diffusion coefficients of drugs. However, permeability values or diffusion coefficients alone cannot be used to determine the transport of drugs in the eye, since dynamic and metabolic barriers can also affect drug distribution.

1.3.2. Dynamic Barriers

Tissue permeabilities measured *ex vivo* do not take into account the effects of dynamic barriers that are present *in vivo*. *In vivo* studies are required to examine the dynamic barriers, which include clearance through lymphatic and blood vessels, bulk fluid flow, and the active transport mechanisms of RPE transporter proteins. Some dynamic barriers cease *post mortem,* and drug levels in some ocular tissues may be overestimated when measurements are obtained *ex vivo*. A summary of experiments investigating the effect of dynamic barriers on transscleral drug delivery *in vivo* is given. Rabbits have typically been used for *in vivo* clearance studies, and constitute the majority of the reports described below.

1.3.2.1. Conjunctival/episcleral clearance

The conjunctiva is well-vascularized in most mammals with considerable variability in vascularity present in the episclera between species (Fig. 1-7) [43-45]. Several studies have been performed to demonstrate that drug present in the conjunctival and episcleral tissues may be cleared through blood and lymphatic vessels.

Ocular lymphatic vessels have been investigated in humans [46-48] as well as in rabbits [49]. Radioactive tracers injected subconjunctivally have been detected in the cervical lymph nodes [50]. It has been estimated that the ^{131}I-albumin-Evans blue complex migrates to the lymph nodes of the neck within six minutes after subconjunctival injection [51]. Figure 1-8 shows the immediate filling of lymphatic vessels after subconjunctival injection of a dye solution.

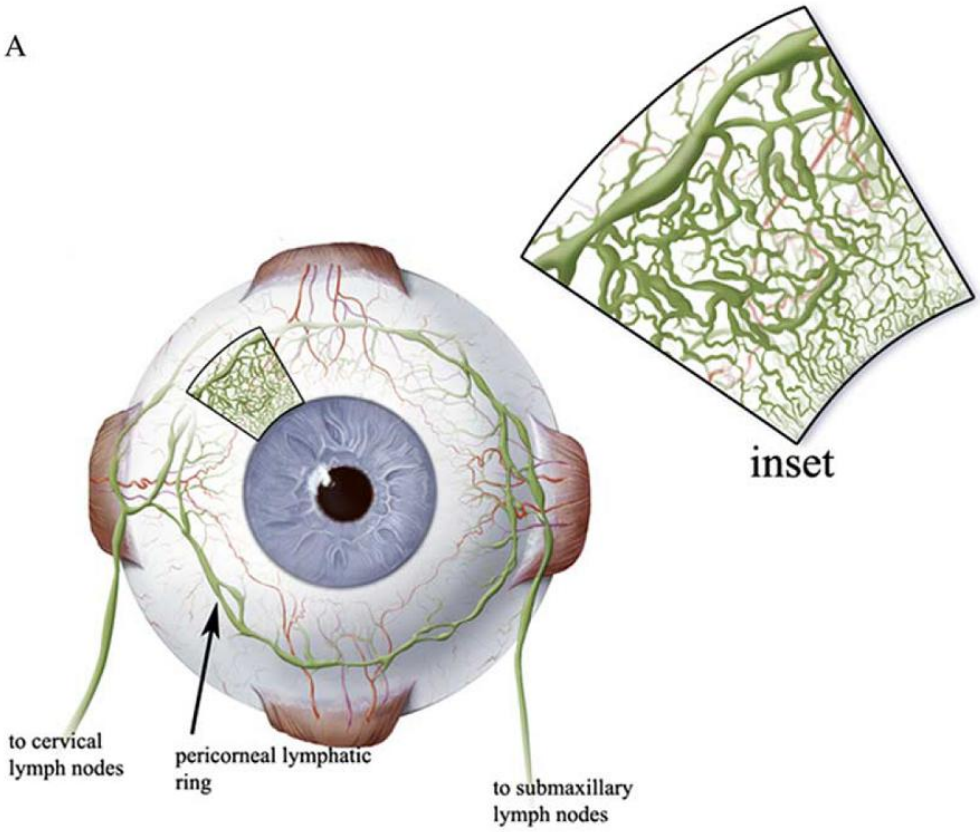

Figure 1-7. Illustration of the conjunctival lymphatic network.

From reference [52].

Figure 1-8. Clearance of dye through conjunctival lymphatics.

From reference [48].

The higher retention of subconjunctivally injected microparticles compared to nanoparticles [53] and the higher half-life of albumin compared to ^{22}Na [54] in subconjunctival tissue suggest that molecular size may affect the rate of conjunctival/episcleral clearance. Reports of the effect of various physicochemical factors on drug clearance through lymphatic and blood vessels are lacking, and further studies are needed to have a clearer understanding of the importance of these mechanisms.

Studies have also demonstrated that selective elimination of the conjunctival/episcleral clearance mechanisms result in higher amounts of intraocular drug penetration. Rabbits that received a sub-Tenon's injection of triamcinolone acetonide with an incised 'conjunctival window' created to inhibit local blood and lymphatic clearance in the conjunctiva had higher levels of drug in the vitreous than rabbits that did not have the incision [55]. Experiments were also performed to

compare the delivery of sodium fluorescein to the retina by periocular injection and a unidirectional episcleral exoplant. The exoplant allowed release of dye on the episcleral side but not on the conjunctival side. Higher amounts of sodium fluorescein were detected in the retina after delivery using a unidirectional episcleral exoplant than after periocular injection [56]. The results from these studies suggest that conjunctival/episcleral clearance mechanisms play a significant role in reducing intraocular drug penetration.

1.3.2.2. Choroidal clearance

Uptake by the rapid blood flow of the choroid is another mechanism by which drugs can be eliminated during transscleral delivery, hindering transport to the retina. Due to its high blood perfusion, the choroid is usually regarded as a sink in which the drug concentration is assumed to be zero when modeling drug transport in ocular tissues [57,58].

Systemic drug levels can be measured by acquiring blood samples, and tilisolol has been shown to be rapidly absorbed into the bloodstream after periocular injection [59]. But the effect of choroidal clearance cannot be accurately determined by systemic drug measurements since drugs cleared from the conjunctival blood vessels as well as the choroidal vasculature are found in the bloodstream. Drugs removed by lymphatic vessels can also contribute to systemic levels since the interstitial fluid is returned to the circulatory system after filtration through lymph nodes.

Cryotherapy is one method that has been used to locally eliminate choroidal blood flow. A single freeze/thaw cycle with cryotherapy forms a chorioretinal scar but leaves the conjunctiva and sclera intact [55]. Sub-Tenon's injections of triamcinolone acetonide were performed in rabbits at least 1 month after receiving cryotherapy to allow time for the conjunctiva and sclera to recover and for maturation of the chorioretinal scar. Rabbits that received cryotherapy did not have higher amounts of triamcinolone acetonide in the vitreous after sub-Tenon's injection compared to those that received cryotherapy [55]. This study suggests that choroidal blood flow may not significantly contribute to drug elimination during transscleral delivery.

1.3.2.3. Clearance by bulk fluid flow

Convective fluid flow in the eye may also contribute to the reduced penetration of drug molecules after transscleral delivery. Drug molecules can be carried along with bulk fluid flows present in ocular tissues and are ultimately cleared mostly through the choroidal or conjunctival vasculature.

1. Uveoscleral outflow

The uveoscleral outflow pathway is also known as the unconventional route [60] for aqueous humor drainage. Aqueous humor flows from the ciliary body into the posterior chamber, through the pupil, and into the anterior chamber. It is then drained either through the trabecular meshwork into Schlemm's canal and aqueous veins (conventional pathway) or directly through the ciliary body and into the

suprachoroidal space (unconventional pathway). From the suprachoroidal space, the aqueous humor flows through scleral channels [61-63] and is cleared by conjunctival lymphatics (Fig. 1-9, uveoscleral flow inset). Studies involving the injection of ^{131}I-albumin-Evans blue into the suprachoroid demonstrated that most of the labeled albumin had passed out through the sclera and drained from the conjunctiva through lymphatic vessels and eventually into the systemic blood circulation [64,65].

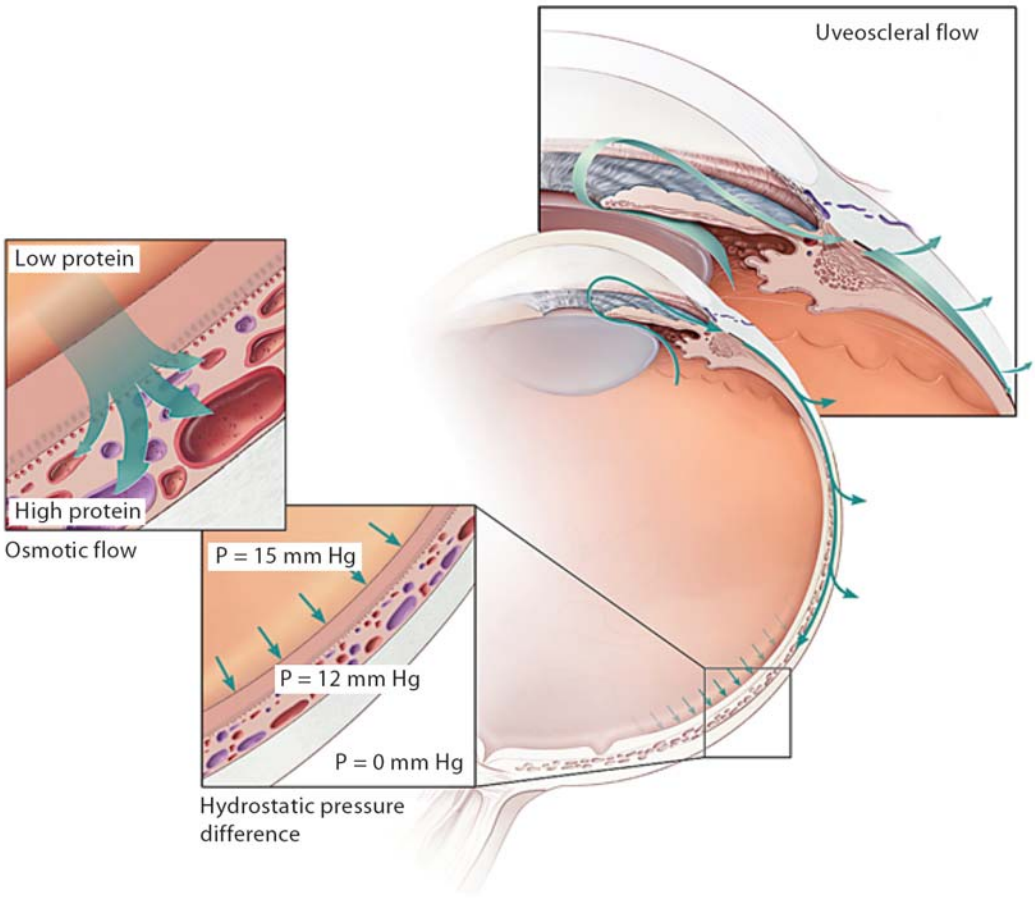

Figure 1-9. Clearance mechanisms by bulk fluid flow present during transscleral delivery.

P = pressure. From reference [24].

The uveoscleral pathway is currently not well understood because there are no methods for determining uveoscleral outflow directly and in a non-invasive manner [66]. It is known that the contribution of uveoscleral drainage on the total aqueous humor outflow differs widely among various species. Uveoscleral drainage has been reported to be in the range of 3 to 8% in rabbits [67] and up to 80% in mice [68]. Values ranging from 4 to 60% have been reported in humans, and the effect of aging on uveoscleral outflow [69] must also be taken into account. While uveoscleral outflow has previously been regarded as a minor route for aqueous humor drainage, the large values reported for uveoscleral outflow in humans indicate that it may play a more significant role.

The uveoscleral pathway may hinder the transport of drugs during transscleral delivery since it generates an outward bulk flow of fluid from the suprachoroidal space. Some drug molecules may be carried along with the convective current of aqueous humor, eventually being cleared by the conjunctival vasculature. Fluid and small particles can pass out directly through the scleral tissue [70], while larger particles exit the suprachoroid via scleral emissary channels found along the blood vessels and nerves that pierce the sclera [61].

2. Hydrostatic and osmotic pressure

While most of the fluid produced by the ciliary body leaves the eye by the aqueous humor drainage routes, some is cleared by passing through the vitreous, retina, pigment epithelium into the choroid. This flow of fluid maintains the

attachment of the retina to the pigment epithelium, and is mainly created by the difference between the osmotic pressures of the choroid and the vitreous [71,72]. The choroid is well vascularized, and is high in protein content. The osmotic pressure of the choroid in rabbits has been calculated to be about 12-14 mmHg [73]. While the choroid has an osmotic pressure similar to that of blood, the vitreous humor has an osmotic pressure lower than that of blood (near 0 mmHg). This difference in osmotic pressure between the choroid and the vitreous generates fluid flow towards the choroid (Fig. 1-9, osmotic flow inset).

The hydrostatic pressure difference between the suprachoroid and the episcleral tissue also contributes to outward bulk fluid flow [74]. At an IOP of 15 mmHg, the hydrostatic pressure of the posterior suprachoroidal space in cynomolgus monkeys was measured as 3.7 ± 0.4 mmHg below the IOP [75]. There is a hydrostatic pressure difference of about 12 mmHg between the suprachoroid and the episcleral tissue, which serves as a driving force for outward bulk fluid flow.

1.3.2.4. RPE transporter proteins

The RPE is responsible for regulating the transport of ions and solutes into the subretinal space. A variety of transporter proteins are expressed in the RPE, including ion transporters, amino acid transporters and drug efflux pumps. Transporter proteins that expel solutes toward the choroid may decrease drug penetration to the retina. Studies on the role of transporter proteins in ocular delivery have been very limited, and their level of involvement as transport barriers is largely unknown. Michaelis-Menten kinetics predicts that at high drug concentrations,

transporter proteins will become saturated, reducing their effect. However, since drug concentration levels at the RPE are typically low during transscleral delivery, transporter proteins may actually be a significant contributor as a barrier to the permeation of various drugs. Many transporter proteins are receptors for specific compounds, and do not affect most other solutes. While a short overview of transporter proteins in the RPE is presented below, a more exhaustive review on the transporters of the blood-retinal-barrier (BRB) including the RPE is given by Mannermaa *et al* [76].

1. Drug efflux pumps

Drug efflux pumps expel toxic and foreign molecules from the cell. They consist of two major efflux transporters: P-glycoproteins (P-gp) and multidrug resistance-associated proteins (MRPs) [77]. Both pumps have a broad substrate specificity, with P-gp pumps generally expelling large neutral or cationic compounds and MRPs removing large neutral or anionic compounds [78]. P-gp and MRP expression have been reported in human RPE with efflux directed towards the choroid, [79-81] preventing drugs from entering the retina.

2. Organic ion transporters

Many ophthalmic drugs are potential substrates of organic anion and cation transporters [76]. The active transport of organic anions by the RPE was first noted by Cunha-Vaz and Maurice [82]. Amines and various drugs exist as anions and cations at physiological pH. Organic cation transporters (OCT) carry endogeneous

amines such as choline, epinephrine, dopamine, guanidine, and histamine as well as organic cation drugs including anticholinergics, adrenergics, antihistamines, xenobiotics and vitamins [76]. Amino acid transporters for glutamate [83,84], taurine [85], and leucine [86] among others have been found in human RPE. Many amino acids show a net flux from the retina to the choroid [87]. Solute transport may also be determined by the relative apical and basolateral concentrations of ions and solute, as in the case for taurine [88,89]. The anti-glaucoma drug brimodine has been shown to be a substrate of organic cation transporters, and its transport is dependent on extracellular pH, temperature, and concentration [90]. The organic anion-transporting polypeptide-E (OATP-E) has been found in the retina of rat eyes [91], but its localization is unknown. Many transporter proteins require further investigation *in vivo* to accurately determine the direction of solute transport.

1.3.3. Metabolic Barriers

Since the eye is exposed to the atmosphere, it serves as a port of entry for xenobiotics into the body. As a defense mechanism, the eye possesses metabolizing enzyme systems which degrade foreign substances that may cause harm to ocular tissues. Drug metabolizing enzymes are present in many ocular tissues, but the ciliary body and the RPE are the most active sites of xenobiotic metabolism in the eye [92]. Higher levels of metabolic enzymes are required in these tissues since they are responsible for detoxifying drugs that are carried by the systemic blood circulation [93,94]. During transscleral delivery, the metabolizing enzymes of the RPE may degrade and detoxify drug molecules, limiting their transport to the retina. Most

studies on metabolic enzymes have been focused on identifying and understanding the metabolic pathway, and there have been few reports that study their effect on ocular pharmacokinetics and distribution of drug molecules [95]. Therefore, the significance of metabolic barriers during transscleral delivery is currently not well understood.

While there are numerous metabolic enzyme systems in the eye, a brief description of major metabolic enzymes found in the RPE is given below. More extensive reviews are given by Kumar [92] and Attar *et al* [78].

1.3.3.1. Cytochrome P-450

The enzymes of the cytochrome P-450 (CYP) family are the most important Phase I drug metabolizing enzymes [92]. Phase I enzymes introduce or unmask polar bodies through oxidation, reduction or hydrolysis reactions. Sufficiently polar metabolites are then excreted while remaining products are further polarized by phase II enzymes such as acetyltransferase, sulfotransferase, and glutathione S-transferase [92]. High levels of CYP enzymes have been reported in mouse [96] and bovine RPE [93,97]. CYP enzymes have broad substrate specificity and metabolize endogeneous and xenobiotic compounds. The CYP3A isozyme, for example, metabolizes more than 50% of commercial drugs [98].

1.3.3.2. Lysosomal enzymes

RPE cells play important roles in the formation of the blood-retinal barrier and in the regulation of solute transport and metabolism. They are also responsible for

digesting shed photoreceptor outer segments which can cause degeneration of photoreceptor cells and subsequent loss of vision when allowed to accumulate. RPE cells degrade the photoreceptor outer segments at a very high rate (3000 million disks in 70 years) [99], using various lysosomal enzymes. Lysosomal enzymes, also known as acid hydrolases, are found in lysosomes and melanosomes [100] and can degrade proteins, polysaccharides, nucleic acids and lipids into low-molecular-weight constituents in an acidic environment [101]. Figure 1-10 shows the levels of lysosomal enzyme activity in ocular tissues compared to levels in the liver. Several ocular tissues express high levels of lysosomal enzyme activity. In bovine ocular tissues, the highest levels of cathepsin B, cathepsin D and acid phosphatase are found in the RPE [101]. Other lysosomal enzymes including α-fucosidase, α-mannosidase, and β-N-acetylglucosaminidase have also been reported in bovine RPE [102]. Natural macromolecular drugs as well as xenobiotics may be degraded by lysosomal enzymes during transport across the RPE, as they are able to cross lysosomal membranes by passive diffusion [103,104].

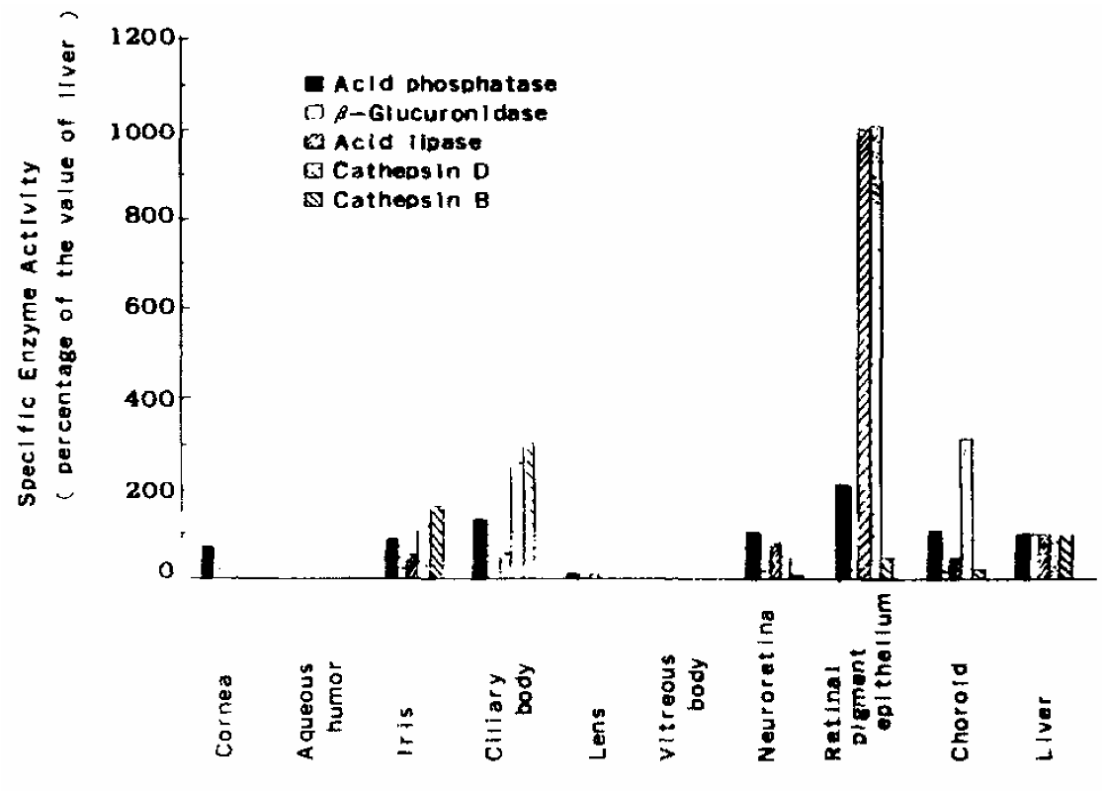

Figure 1-10. Levels of lysosomal enzymes in ocular tissues.

From reference [101].

1.3.4. Concluding Remarks

Most studies on transport barriers affecting transscleral drug delivery have focused on the determination of permeability values of ocular tissues. Permeability values are helpful for comparing diffusional resistances of one tissue to another and can also be used to calculate the diffusion coefficients of drugs. However, permeability values or diffusion coefficients alone cannot be used to determine the transport of drugs in the eye, since dynamic and metabolic barriers can also affect drug distribution.

The effect of dynamic barriers on drug penetration after transscleral delivery has been demonstrated in studies using magnetic resonance imaging (MRI), which allows the acquisition of three-dimensional images non-invasively *in vivo*. Dynamic barriers are active *in vivo* but cease *post mortem*, while static barriers are always present. A comparison of scans acquired *in vivo* and *post mortem* revealed increased penetration of a MRI tracer released from a polymeric episcleral implant into the anterior chamber and vitreous *post mortem* but not *in vivo* [105]. Similar results were obtained after subconjunctival injection of manganese ions [106]. The difference in results between the *in vivo* and *post mortem* scans suggest that dynamic barriers which cease *post mortem* significantly affect intraocular drug levels. Therefore, assessment of transscleral drug penetration cannot be accurately determined in systems involving only static barriers.

While the general effect of dynamic barriers on transscleral drug delivery has been demonstrated, the effect of individual dynamic barriers is unknown. The challenge of isolating the dynamic barriers during data acquisition currently prevents the direct comparison of one dynamic barrier to another. Understanding the importance of individual dynamic barriers will enable the improved design of drug delivery methods and devices. For example, the recent investigations examining the significance of conjunctival clearance has led to the design of the unidirectional episcleral exoplant [56], which minimizes drug loss to conjunctival blood and lymphatic flow. The posterior infusion of drug into the suprachoroidal space [107] is another method to bypass the conjunctival clearance mechanisms, allowing for greater delivery of drug to the macula.

A review of the literature shows that static barriers have been examined in detail, but studies investigating the significance of dynamic and metabolic barriers in transscleral drug delivery are sparse. While tissue permeability is important for drug transport, recent *in vivo* studies demonstrate that clearance and elimination mechanisms play a significant role in reducing drug delivery to the retina. Further studies exploring the effects of dynamic and metabolic barriers are warranted in order to improve our understanding of drug transport in transscleral delivery.

1.4. Methods of Ocular Pharmacokinetic Data Measurement

1.4.1. Traditional Methods

Ocular pharmacokinetic data has typically been measured by administering the drug of interest in an animal model and enucleating the eye after a specified period of time. The eye is then immediately frozen, the desired tissues dissected, and various extraction procedures are then performed to recover as much of the drug as possible. However, this requires the use of several animals in order to monitor the change in drug levels over time. Since there are physiological variations from one animal to the next, this adds error to the results and complicates pharmacokinetic analysis [108]. There are also errors in drug measurement as extraction efficiencies are often low and the thin, delicate tissues of the eye wall are difficult to completely isolate.

Fluorescence, autoradiography and drug extraction from tissues are traditional *ex vivo* techniques used to study drug penetration and elimination in the eye [109-112]. However, methods which require data measurement from tissues *ex vivo* may

not yield accurate results as the spatial distribution of drugs may change during the time interval that tissues are being harvested. Additionally, tissues are usually digested in its entirety and one drug measurement is obtained for the entire tissue. Therefore, information regarding the distribution of drugs is lost. Figure 1-11 shows a schematic which illustrates a sampling technique to acquire spatial drug distribution data; however, this technique is tedious and prolongs the dissection time.

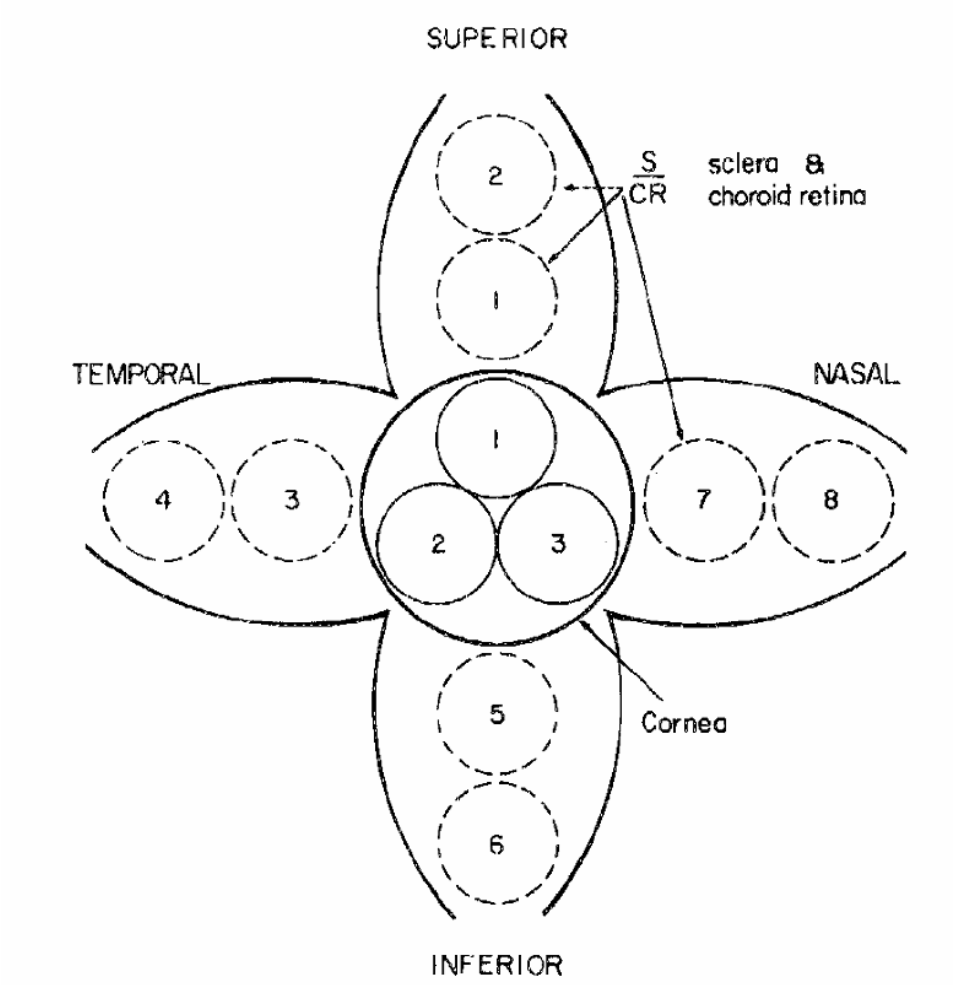

Figure 1-11. Schematic of tissue sampling sites for ocular drug distribution assessment.

From reference [113].

1.4.2. Non-invasive methods

Owing to their non-invasiveness, imaging techniques have become attractive methods for the assessment of drug distribution [114-117] and drug delivery [118]. Gamma scintigraphy, MRI, positron emission tomography (PET), and single photon emission computed tomography (SPECT) are some of the most widely used imaging modalities in studies of drug delivery and pharmacokinetics [114,116,119]. Nuclear imaging techniques (gamma scintigraphy, PET, and SPECT) have been widely used to assess the distribution of radiolabeled drugs in various applications such as in the determination of pharmacokinetics of anticancer therapies [120] and drugs for pulmonary delivery [121]. These methods also allow quantitation of drug distribution and drugs can be used as contrast agents after radiolabeling. Several studies have successfully utilized fluorine-18-labeled ciprofloxacin for PET studies in humans [122,123]. They are highly sensitive methods, permitting drug concentration measurements as low as 10^{-12} mol/L [117]. The temporal and spatial resolution is also excellent, with typical image acquisition in seconds to minutes with 1-5 mm resolution [114]. However, the use of radioactive materials requires additional precautions to be taken during imaging procedures including radioactive waste handling and the radiation exposure of patients/volunteers and clinical staff. Also, many radioactive tracers have short half-lives (^{15}O, $t_{1/2}$: 2.07 min; ^{13}N, $t_{1/2}$: 9.96 min; ^{11}C, $t_{1/2}$: 20.4 min), limiting their use to short experiments [114].

Optical coherence tomography (OCT) is another popular imaging method, with the most successful clinical application in ophthalmology [124,125]. OCT can achieve resolutions of 1-15 μm (10-100 times finer than MRI), and the imaging procedure can be carried out with noninvasive or minimally invasive delivery systems such as handheld probes, endoscopes, catheters, laparoscopes and needles [126]. Despite the integration of OCT into various medical and biological applications, no optical contrast agents have been developed for this technology. Since the image contrast mainly comes from the scattering and absorption of light by tissues, both the sensitivity and specificity of OCT have a strong dependence on the intrinsic optical properties of the biological sample, often limiting its diagnostic capability.

MRI is a non-radioactive method which forms images from the nuclear magnetic resonance signal generated by certain nuclei (^{1}H being the most commonly imaged) after being subject to a high magnetic field. Typical sensitivity values range from 10^{-5} to 10^{-3} mol/L, the temporal resolution is on the order of minutes, and the anatomical resolution is higher than that of PET [117]. While high-resolution imaging of the eye has been reported in previous anatomical studies [127], the use of MRI for ocular pharmacokinetics has not been widely investigated. In this research, ocular pharmacokinetic data was acquired by using dynamic contrast-enhanced magnetic resonance imaging (DCE-MRI). Many MRI contrast agents are conjugates of gadolinium, a paramagnetic metal that increases the signal intensity of nearby water molecules in the presence of a magnetic field. This allows the enhancement of contrast between tissues with and without contrast agent, and also increases the signal to noise ratio (SNR) of the image. DCE-MRI permits the measurement of a magnetic

tracer by producing high-resolution images that can be obtained in real-time and non-invasively *in vivo*. DCE-MRI provides spatial and temporal measurements of drug levels in the eye, and may become an important tool in the study of ocular pharmacokinetics [128].

In ocular research, DCE-MRI has become a valuable method in the study of the integrity and permeability of the blood-retinal barrier [129-131]. Ocular pharmacokinetic data have also been acquired with DCE-MRI by using a calibration curve to convert T_1 or signal intensity values to the concentration of the contrast agent [105,132]. The increased utilization of non-invasive pharmacokinetic imaging tools such as DCE-MRI may enable better understanding of drug clearance and distribution in future drug delivery studies for the eye.

1.5. Project Overview

As the development of ocular drug delivery devices has gained momentum in recent years, the gaps in the understanding of drug transport barriers in the eye have become more evident. To address this need, pharmacokinetic imaging tools, more specifically MRI, have been proposed and recently utilized to assess drug delivery in the eye [105,106,133,134]. MRI is a versatile technique and can provide information that cannot be obtained from traditional invasive pharmacokinetic measurement methods. No other quantitative technique has been explored for imaging the ocular distribution of drugs *in vivo*. Therefore, the use of MRI is potentially very attractive and may play an important role in future studies of ocular drug delivery assessment.

However, as with any measurement technique, MRI has limitations which need to be investigated in order to ensure that the data is interpreted correctly.

To address the current needs of the ocular drug delivery community, several goals have been achieved in this work: (1) to evaluate transscleral drug delivery *in vivo* using MRI, (2) to assess MRI as a technique for evaluating drug delivery in the eye, and (3) to better understand the significance of individual barriers in the eye by quantitatively analyzing experimental (MRI) data and by pharmacokinetic modeling. Two major animal imaging projects are presented in this work: the assessment of sustained transscleral drug delivery by continuous infusion (Chapter 3) and the determination of drug elimination kinetics after subconjunctival injection (Chapter 4) using DCE-MRI. These studies demonstrate the powerful potential of MRI and its advantages. Chapter 2 discusses the method by which MR images are converted to quantitative results and the limitations in this conversion. Chapter 5 presents a transscleral drug delivery model and the comparison of MRI data to the model results. Through this comparison, restrictions in the use of MRI for quantitative data measurement are discussed.

Since the initial stages of this research, there has been much interest in the ocular drug delivery community in the use of MRI for evaluating drug delivery. The use of pharmacokinetic imaging tools such as MRI will likely continue to grow in ocular drug delivery. Therefore, this work seeks to evaluate MRI as a pharmacokinetic imaging tool in ocular drug delivery, as well as present some of its powerful capabilities.

Chapter 2: Calibration of Contrast Agents

2.1. Introduction

2.1.1. MRI Physics

In nuclear magnetic resonance imaging, the signal is produced from the very center of the atom. Atoms containing unpaired protons or neutrons have net spin and angular momentum. All atomic nuclei with an unequal number of nucleons also possess a magnetic moment [135]. Figure 2-1 shows magnetic moments of atoms in random orientations.

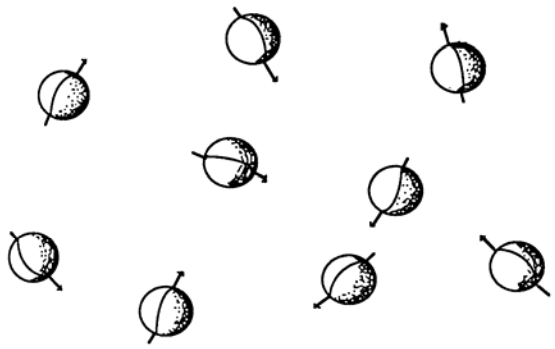

Figure 2-1. Random alignment of atoms in the absence of an applied magnetic field.

From reference [136].

When protons are exposed to the presence of a large external magnetic field (B_o), alignment of the magnetic moments occur either in the parallel (ground state, low energy) or antiparallel (excited state, high energy) direction (Fig. 2-2). Slightly more protons are in the ground state, resulting in a net magnetization vector (M_o).

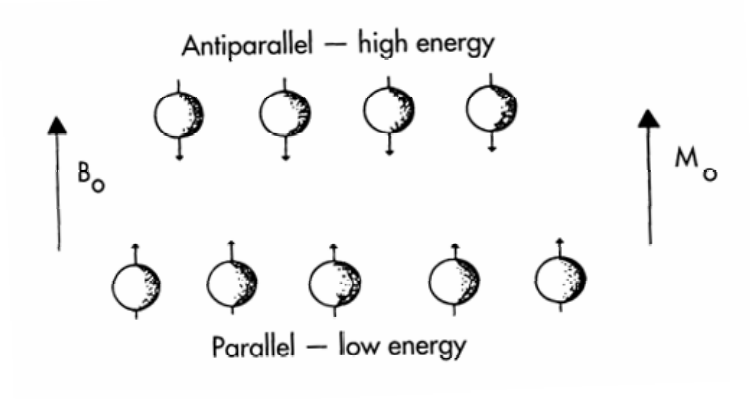

Figure 2-2. Alignment of atoms in the presence of an applied magnetic field B_o. From reference [136].

In order to create an MR signal which can be detected, M_o must be reoriented into the transverse plane from the longitudinal axis to cause a signal in the radiofrequency (RF) receiver coils (Fig. 2-3). A second magnetic field is applied in the form of a RF pulse to flip M_o into the transverse plane. The frequency of the RF pulse is determined from the Larmor equation:

$$\omega = \gamma \times B_0 \qquad (1)$$

where ω is the precessional frequency and γ is the gyromagnetic ratio (constant for a given nucleus; 42.58 MHz/T for hydrogen).

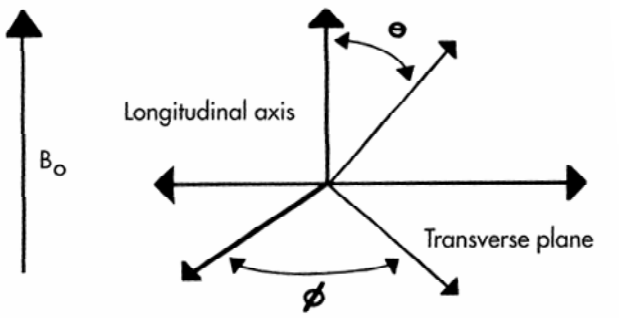

Figure 2-3. The longitudinal axis and the transverse plane.

From reference [136].

This energy applied in the form of a RF pulse is equivalent to the energy difference between the two proton states. For a 1-T magnet system, the protons will resonate at 42.58 MHz.

MRI exploits frequencies in the radiowave range, as shown in Figure 2-4. In this low frequency range, the human body is transparent to radiation which is low and nonionizing.

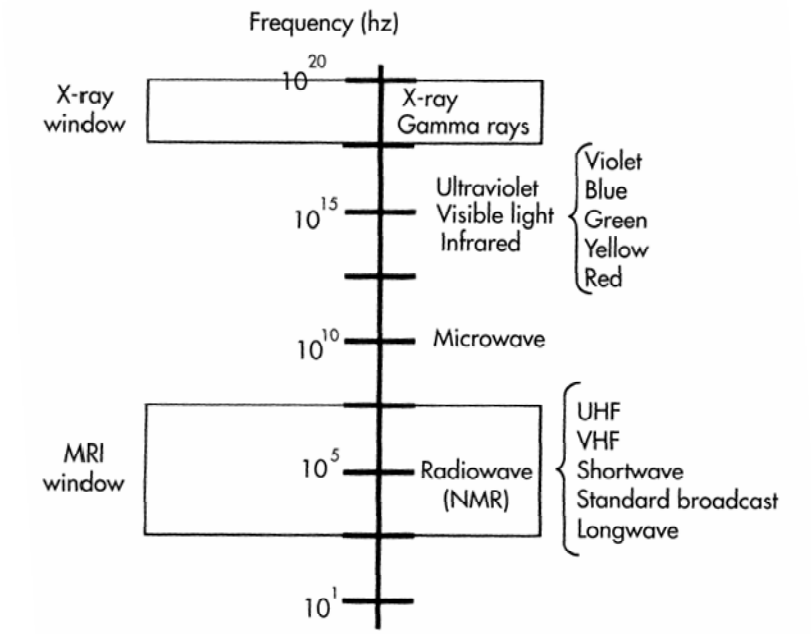

Figure 2-4. The electromagnetic spectrum.

From reference [136].

Of all the atoms with unpaired nucleons, hydrogen is the most important atom for medical MRI since it makes up two-thirds of all atoms in humans. Every cubic centimeter of water has approximately 10^{23} protons. In addition to its chemical abundance in the body, hydrogen is also highly magnetic, increasing its MR sensitivity.

After the RF pulse is applied, signal will begin to immediately decay as protons lose coherence in precession. There are two sources of irreversible signal loss: T_1 and T_2 relaxation. The process of energy dissipation to the surrounding magnetic environment as protons move from the high excited energy state to the ground state is called T_1 relaxation. T_1 is the time for 63% of the longitudinal

magnetization to recover following the RF pulse (Fig. 2-5). The relationship of signal intensity (SI) and T_1 depends on the time between RF pulses (repetition time or TR) and the T_1 of the tissue [136]:

$$SI = f\left(1 - e^{\frac{-TR}{T_1}}\right) \tag{2}$$

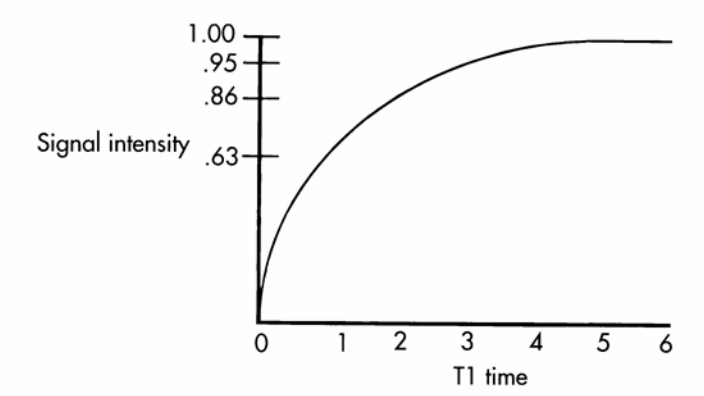

Figure 2-5. The intensity curve for T_1 relaxation.

From reference [136].

T_2 is the loss of transverse magnetization and is the time necessary to reduce the transverse magnetization to 37% of its original value following the RF pulse (Fig. 2-6). The relationship between SI and T_2 depends on the time from the RF pulse until the echo is received (echo time or TE) and the T_2 of the tissue [136]:

$$SI = f\left(e^{\frac{-TE}{T_2}} \right) \tag{3}$$

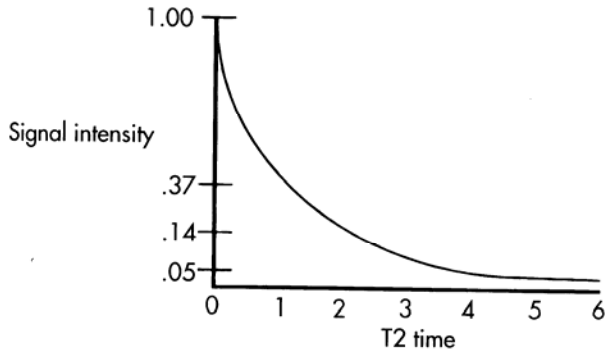

Figure 2-6. The intensity curve for T_2 relaxation.

From reference [136].

2.1.2. Pulse Sequence

As previously discussed, SI is produced by transverse magnetization, which is affected by T_1 and T_2 relaxation times. Other factors also affect SI, such as proton density (N), flow (f[velocity]) as well as RF pulse characteristics. While the specific equation for SI is dependent on the type of sequence used, a general form can be summarized as [136]:

$$SI = N \times f(v) \times e^{\frac{-TE}{T_2}} \times \left(1 - e^{\frac{-TR}{T_1}}\right) \quad (4)$$

When a short TR and TE is used, the resulting image will emphasize the T_1 characteristics of the tissue, and is said to be "T_1 weighted." A long TR and TE will result in a "T_2 weighted" image.

2.1.3. Contrast Agents

Paramagnetic materials are used to produce T_1 shortening. As seen from Figure 2-7, a decrease in T_1 relaxation time results in increased signal intensity. Paramagnetic materials include metal ions that have unpaired electrons (such as gadolinium, iron, and manganese) which have unpaired spins. The magnetic moment produced by these unpaired electrons is about 1000 times greater than that of a hydrogen nucleus [137].

Gadolinium-diethylenetriaminopentaacetic acid (Gd-DTPA, also known as Magnevist) is a paramagnetic agent, and develops a magnetic moment when placed in a magnetic field. Gd-DTPA enhances the relaxation rate of water protons in its vicinity by decreasing the T_1 relaxation time in tissues where it accumulates. Gd-DTPA is an extracellular contrast agent, and is cleared through the kidneys. It is used widely clinically, and does not produce toxic effects in the body. The DTPA chelate does not dissociate from the Gd ion, and overall the agent carries a -2 charge. The agent is highly soluble in water.

Other contrast agents such as Mn^{2+} and $MnEDTA^{2-}$ [106], $MnCl_2$ [138], Gd-albumin [139] have been explored in ocular *in vivo* studies as well as Gd-DTPA [105,131,134].

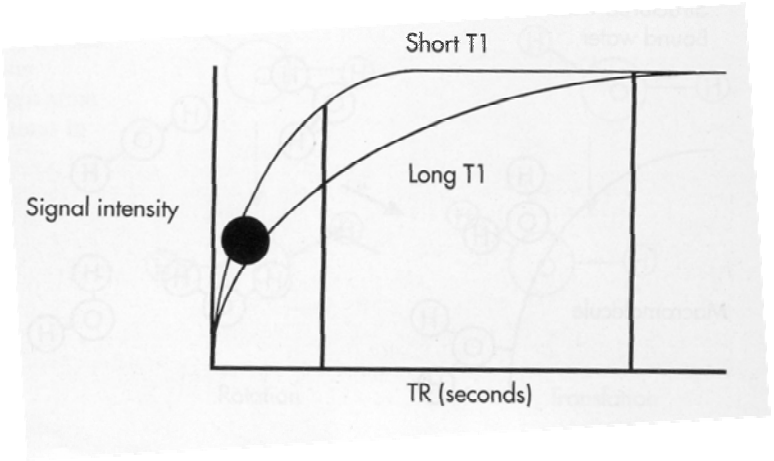

Figure 2-7. The effect of T_1 on signal intensity at a specified TR.
From reference [136].

2.1.4. Factors Affecting MR Images

The signal-to-noise ratio (SNR) is an important factor in MR imaging. Due to the low detection sensitivity of MRI, noise superimposed on the images can significantly degrade the image quality. SNR can be most easily increased by increasing the voxel size or the number of excitations (NEX).

The voxel size is determined by the field of view (FOV), matrix size, and the slice thickness. Increasing the voxel size increases the number of spins contributing

to the signal intensity, thereby increasing the SNR. Therefore, increasing the FOV, decreasing the number of pixels in the FOV by decreasing the matrix size, and increasing the slice thickness will all contribute to increased SNR. However, in doing this the spatial resolution will increase; therefore, a balance between spatial resolution and SNR must be achieved. Increasing the FOV is particularly significant in ophthalmic MRI since the eye occupies a small area and spatial resolution can be quickly lost.

The SNR can also be improved at the expense of scan time by increasing the NEX. However, increased scan times may not be permissible in studies where changes are occurring over short time periods. Repeated sampling through increased NEX allows greater signal averaging. The SNR increases proportionally with the square root of NEX, as shown in the following relation [140]:

$$\text{SNR} \sim (\text{FOV}/\text{matrix})*\text{slice thickness}*(\text{NEX})^{1/2} \quad (5)$$

MRI is a multiparametric modality, and the trade-offs that accompany the choice of the operating parameters in terms of the achievable image contrast, spatial resolution, and scan time must be recognized [140].

2.1.5. Conversion of Signal Intensity to Concentration

MRI can be utilized as a quantitative technique by converting data from the acquired images into concentration values of drug in each pixel. In order to convert image data into concentration levels of contrast agent, a calibration curve is needed.

The calibration curve is generated using various concentrations of contrast agent in a tissue phantom and scanning the samples using the same MR parameters that are used in the animal experiment.

Different types of image data can be used to derive the concentration information of the contrast agent. For example, if T_1 scans are performed, various values of T_1 can be measured at different known concentrations of contrast agent in tissue phantoms. An example of a T_1 calibration using the contrast agent $MnEDTA^{2-}$ is shown in Figure 2-2.

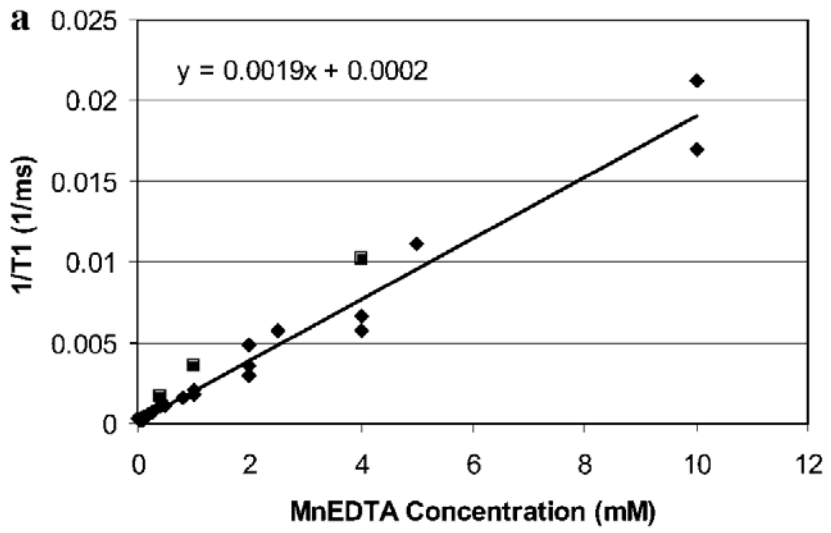

Figure 2-8. Calibration showing the linear relationship between inverse T_1 relaxation time and $MnEDTA^{2-}$ concentration.

From reference [106].

In this research, T_1-weighted images were acquired, and signal intensity values (instead of T_1 measurements) were used to calculate the concentration levels of contrast agent. 2% hydroxypropyl methylcellulose (HPMC) and phosphate buffered saline (PBS) were used as imaging phantoms. As will be explained in Chapters 3 and 4, 2% HPMC and PBS were chosen to mimic the suprachoroidal space and the subconjunctival bolus, respectively.

2.2. Methods

Tissue phantoms were prepared by using various concentrations of contrast agent (Gd-DTPA or gadolinium-albumin) in solutions of PBS (pH: 7.4) and 2% HPMC. Gd-DTPA was purchased from Berlex, Inc. (Monteville, NJ) and gadolinium-albumin (Gd-albumin) was purchased from Biopal, Inc. (Galbuim; Worcester, MA). HPMC was dissolved in PBS by stirring the solution at 90 ºC for 3 hours. Concentrations ranging from 10^{-6} to 0.5 M (stock concentration) for Gd-DTPA and 10^{-6} to 0.37 mM (stock concentration) for Gd-albumin in either PBS or HPMC were poured into 2 mL HPLC glass vials to be scanned with MRI. At least 4 sets of each type of tissue phantom were prepared and imaged.

The calibration samples were placed within a volume coil, and MRI scans were acquired using the same sequence parameters used for the animal experiments. All MRI experiments were conducted using a 4.7 Tesla MRI system (Bruker Instruments, Billerica, MA).

Signal intensity values from images were determined using image analysis software, ImageJ (ver 1.33u, NIH, Bethesda, MD). A circular region-of-interest

(ROI) was manually drawn inside each vial and the average signal intensity was measured. Signal intensity values were normalized either to the signal intensity of the phantom without contrast agent (for Gd-DTPA samples in HPMC) or to the signal intensity of the administered concentration (1 mM for Gd-DTPA and 0.1 mM for Gd-albumin in PBS) in animal experiments. This data along with the corresponding concentration of contrast agent were used to generate the plot for the signal intensity vs. concentration calibration curve.

2.3. Results

Figure 2-9 shows an image from a calibration MRI scan using phantoms of Gd-DTPA in PBS in glass vials. The varying signal intensity with concentration of contrast agent can be observed.

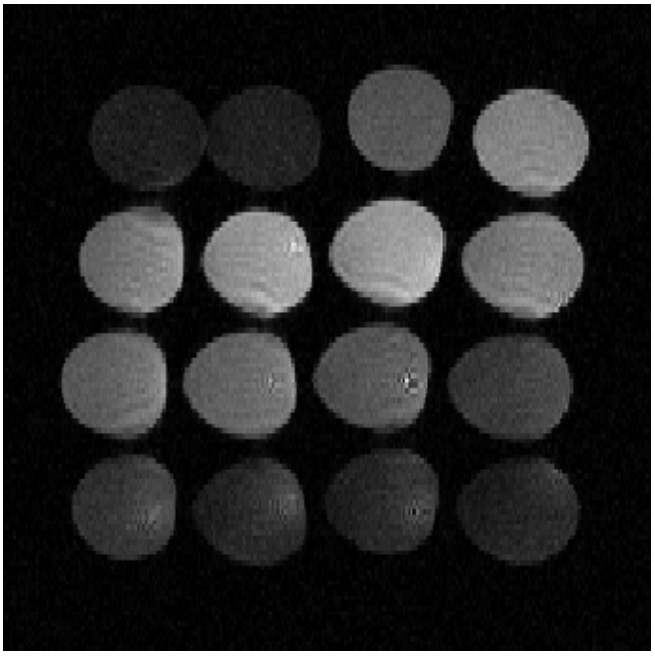

Figure 2-9. MR image of Gd-DTPA phantoms in PBS.

Figure 2-10 shows a calibration curve constructed for Gd-DTPA in PBS. At low concentrations ($<10^{-5}$ M), the signal intensity reaches a plateau and the limit of concentration detection is reached. The signal intensity increases with Gd-DTPA concentration and a peak signal intensity is observed. At high concentrations ($>10^{-2}$ M) the signal intensity decreases due to T_2 shortening effects [141].

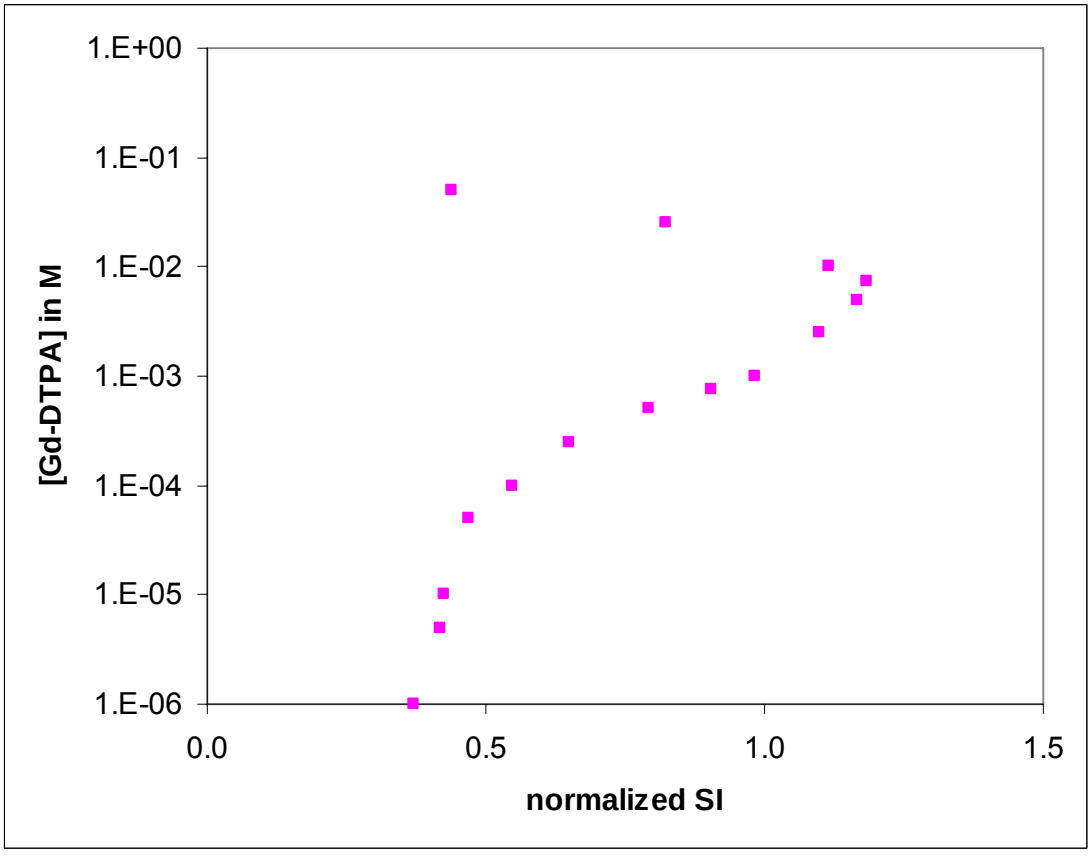

Figure 2-10. Gd-DTPA calibration showing the relationship between concentration and signal intensity.

Figure 2-11 shows the calibration curve for Gd-DTPA in PBS utilized in MR image analysis for studies described in Chapter 4. A sixth-order polynomial was fit to the selected data range to yield the best fit. The calibration curve shows that the concentration detection range spans a couple orders of magnitude. The limits of concentration detection are $3e^{-5}$ M and 0.05 M for Gd-DTPA in PBS.

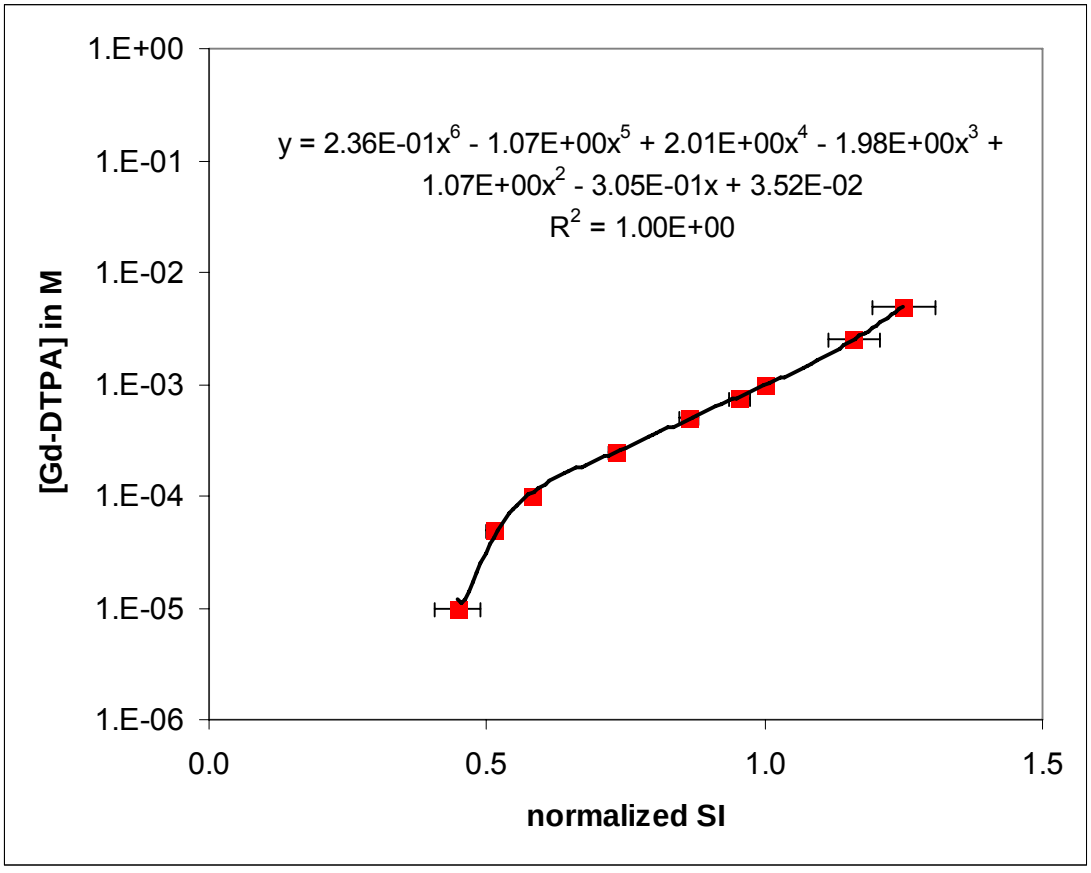

Figure 2-11. Gd-DTPA calibration in PBS.

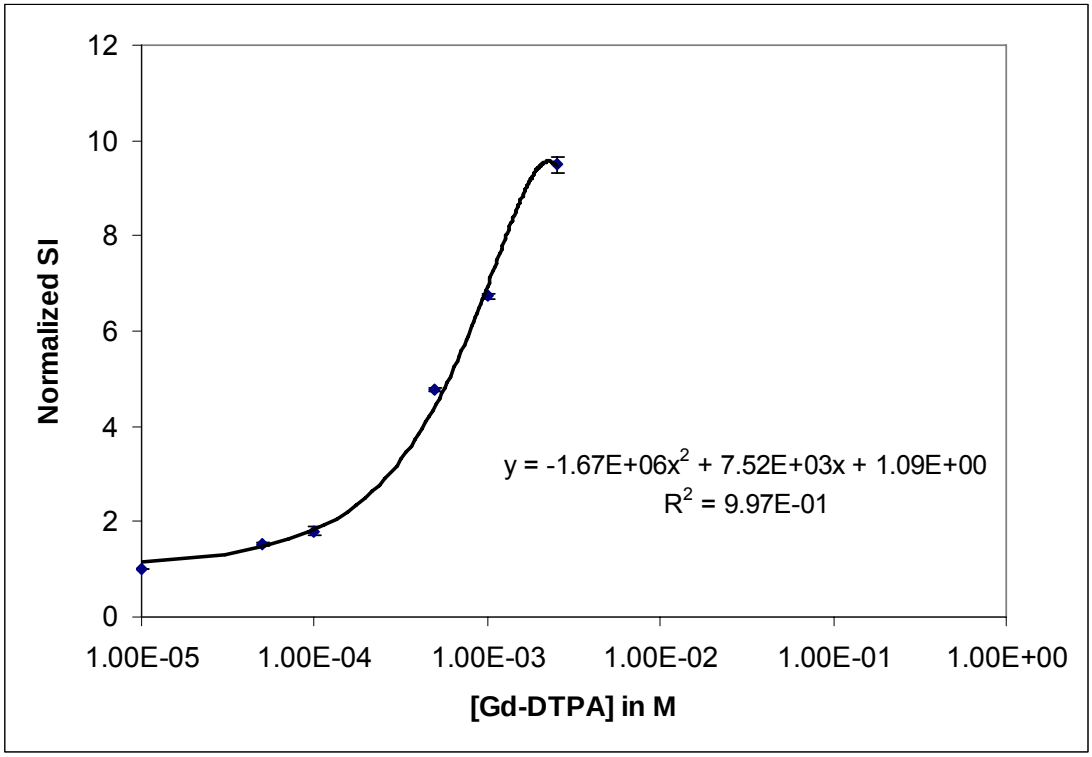

Figure 2-12. Gd-DTPA calibration in 2% HPMC.

Figure 2-12 shows the calibration of Gd-DTPA in 2% HPMC, with images acquired using the same MR parameters described in Chapter 3. Signal intensity values are different at a given Gd-DTPA concentration when comparing Figures 2-12 and 2-13 since the phantoms and MRI parameters (TR, TE) are different.

Figure 2-13 is the calibration used for Gd-albumin studies in Chapter 4. The limits of detection are 0.005 to 0.37 mM.

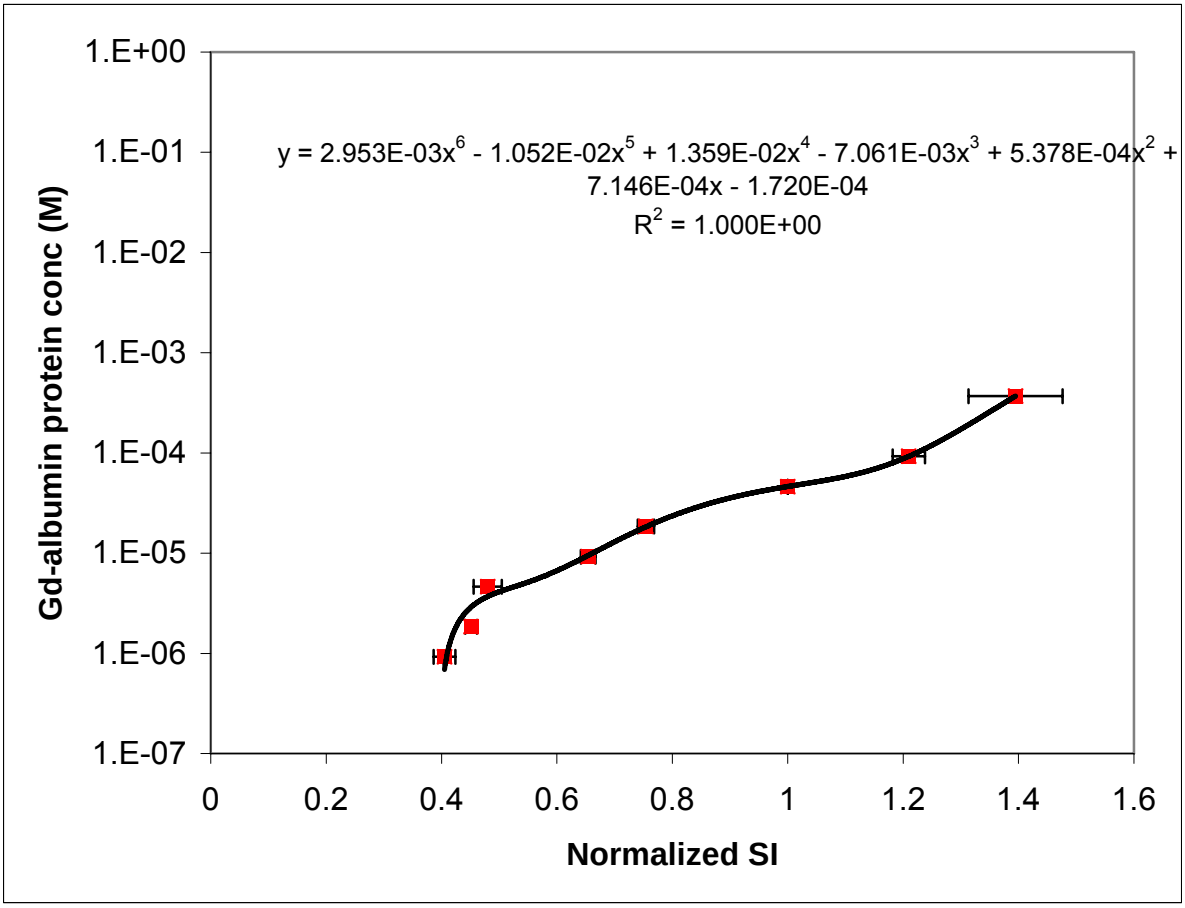

Figure 2-13. Gd-albumin calibration in PBS.

2.4. Discussion

Calibrations of various contrast agents in different phantom media can be constructed to quantitate MRI data. While 2% HPMC has been used in prior studies to simulate tissues that contain loose connective tissue [105,134], it is more difficult to construct synthetic phantoms that will successfully mimic the relaxation rates in other ocular tissues that consist of more complex structures.

Table 2-1 gives a list of T_1 relaxation rates from various ocular tissues determined in a rabbit eye. These experimental T_1 values are comparable to values reported for the human eye [142]. While the T_1 of the vitreous is similar to the value for PBS and HPMC, the tissues such as the conjunctiva, choroid, and retina have extracellular volume fractions less than 50%, and have very different T_1 relaxation rates than the tissue phantoms used in this study. Therefore, phantom materials that have lower T_1 relaxation rates should be used to construct calibrations for these ocular tissues, since the lower T_1 value of the tissue will affect the T_1 relaxation rate of contrast agent.

Phantom/Tissue	**T_1 (ms)**
PBS	3390
2% HPMC	3201
Conjunctiva	1701
Sclera	1872
Choroid-Retina	2288
Vitreous	3307

Table 2-1. T_1 measurements in phantoms and ocular tissues.

There are currently no standards for use as tissue phantom standards in biomedical MR imaging (Workshop on Pharmacokinetic/Pharmacodynamic Imaging, USC, January 22-23, 2007). All sectors in government, industry and academia realize

the important need for standardization in the use of tissue phantoms for accurate and consistent quantitative analysis in biomedical imaging. Agarose is typically used as a brain tissue phantom, but this may not be a good phantom for ocular tissues since tissue compositions vary.

The concentration range detected by using signal intensity data spans about 2-3 log units. This range may be further increased by using T_1 measurements instead of signal intensity data. While sensitivity may be increased by using T_1, longer scan times are required to acquire T_1 scans (~1 hour for one scan). For the studies in this research, short scans (~3-11 minutes) were required to capture the kinetic changes that were occurring in ocular tissues. Therefore, performing T_1 scans was not feasible in this study, but may be used in other experiments that can accommodate longer scan times.

2.5. Conclusion

The results from scanning MRI phantoms show that there is a concentration range that may limit the measurement capability for certain experiments. The phantoms used in this study cannot be used for cellular tissues, since there is a large discrepancy in T_1 relaxation rate. While limitations in conversion may exist, MRI is highly advantageous in acquiring tissue concentration levels *in vivo* which is not feasible with many traditional ocular pharmacokinetic measurement techniques.

Chapter 3: Assessment of Sustained Drug Delivery by Infusion

3.1. Introduction

Due to the lack of clinical efficacy in transscleral drug delivery, the incorporation of sustained release methods have been proposed to enhance delivery to the choroid and retina [3,25]. As previously discussed in Chapter 1, sustained delivery methods include the use of micro and nanoparticles and polymeric implants loaded with drug. Recently, transscleral delivery methods involving continuous infusions have been reported using an osmotic pump for sustained delivery into the eye [20,21]. Figure 3-1 is an illustration from a study in which an osmotic pump attached to a flexible catheter was inserted into the sclera for continuous drug delivery. The study concluded that bioactive proteins infused in this manner delivered therapeutic levels to the choroid and retina with negligible systemic absorption.

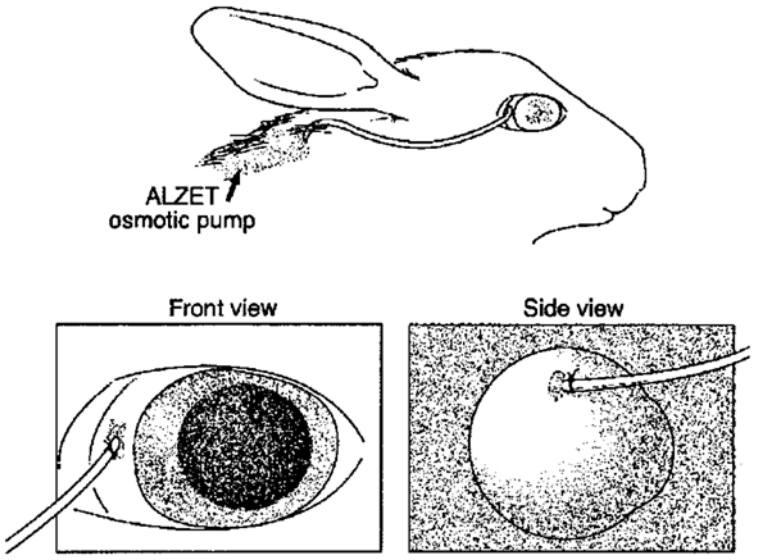

Figure 3-1. Intrascleral osmotic pump implantation in a rabbit eye.

From reference [20].

In this study, sustained transscleral drug delivery was explored by continuous infusionin the live rabbit. Two different transscleral infusion methods were investigated by positioning the catheter either subconjunctivally or intrasclerally. Magnetic resonance imaging was utilized to evaluate delivery and its capability in imaging drug delivery in the eye was also assessed.

3.2. Methods

3.2.1. Animal Setup

Female New Zealand White rabbits weighing 3-3.5 kg were purchased from Covance Laboratories, Inc. (Vienna, VA, USA) and were used according to the

guidelines set forth in the ARVO statement for the Use of Animals in Ophthalmic and Vision Research. Rabbits were monitored under general anesthesia during the MRI scan period. Placement of subconjunctival catheters behind the globe has been previously reported to deliver drugs to the macular region [20,143]. However, access to the back of the globe is difficult and intrascleral catheter placement may result in an inadvertent perforation. As a result, we placed catheters anteriorly, with the axis parallel to the limbus, for easier access. A 9-0 vicryl suture was placed at the limbus and the eye was rotated downward to expose the superonasal quadrant. A 24 gauge × ¾ inch long intravenous catheter (Terumo Medical Corporation, Somerset, NJ) was prepared by removing the plastic tubing and hub from the needle and cutting off the tubing from the hub (Fig. 3-2). The tube and hub were threaded back onto the needle and then inserted either subconjunctival or intrascleral 3-4 mm from the limbus. For intrascleral insertions incisions were made in the conjunctiva and Tenon's fascia with Wescott scissors to reveal bare sclera to ensure that the tubing was placed intrascleral. The catheter was inserted superonasally and was advanced into the eye at least 5 mm for subconjunctival infusions and 3 mm for intrascleral infusions. The needle was then carefully withdrawn, leaving the catheter remaining in the tissue. The eyelids were sutured closed to prevent corneal and sclera desiccation during the scan, and the distal portion of the catheter was left protruding out between the eyelids. The catheter was connected to 7 m of PE-10 tubing (Becton Dickinson, Franklin Lakes, NJ) by a 10 cm length of silicone tubing (0.025" ID × 0.047" OD RenaSil; Braintree Scientific, Inc., Braintree, MA). The silicone tubing was glued on one end to the PE-10 tubing and prefilled with Gd-DTPA solution before connecting to the catheter by a

friction fit. The Gd-DTPA solution was prepared by diluting the stock concentration 100-fold in PBS (pH 7.4) to 5 mM. The solution was administered through the entire tubing by using a programmable infusion syringe pump (Stoelting Co., Wood Dale, IL) located outside the scan room. A 3-way stopcock was used to connect the syringe and the PE-10 tubing to prevent leakage of solution from the catheter before and after the infusion. The Gd-DTPA solution was faintly colored with 100 mg/ml sodium fluorescein (Akorn, Inc., Decatur, IL) to a final concentration of 0.5 mg/ml to enhance visibility of the fluid in the tubing.

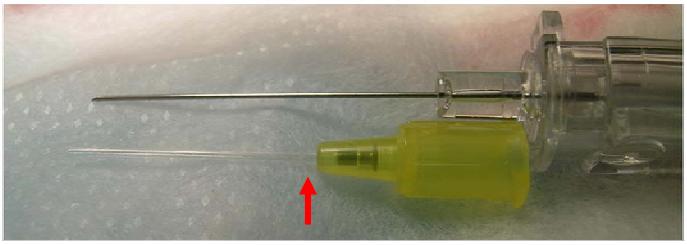

Figure 3-2. Photograph of IV catheter.

24 gauge IV catheter shown with plastic hub and tube removed from needle. Arrow indicates point of separation of plastic hub and tube.

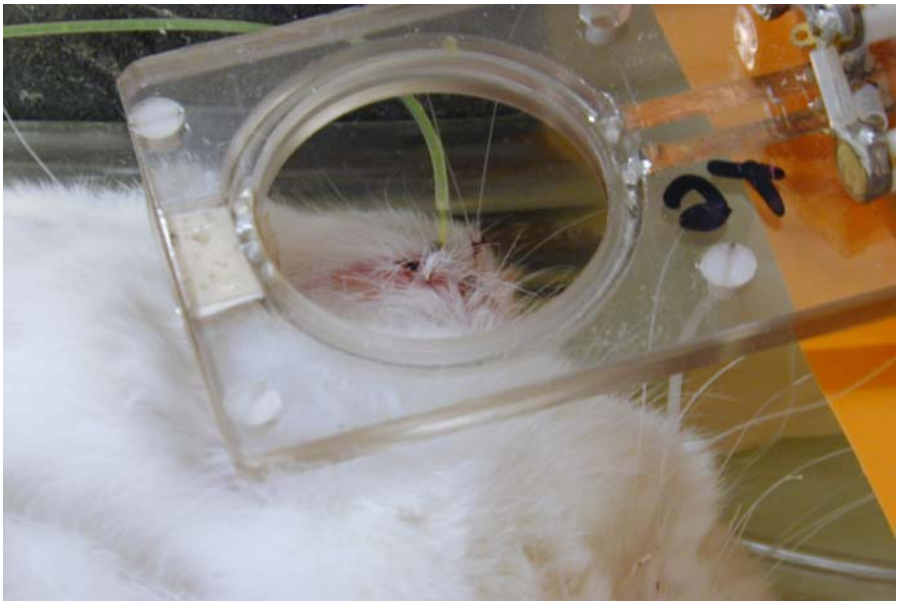

Figure 3-3. Custom-built surface coil placed over the rabbit eye.

3.2.2. MRI Setup

Experiments were performed using a 4.7 Tesla MRI system (Bruker Instruments, Billerica, MA). Following placement of the catheter, a 4 cm passively decoupled receive-only surface coil was placed over the rabbit's eye (Fig. 3-3). The rabbit was placed on a cradle and inserted in a transmit-only volume coil. T_1-weighted images were acquired using a 2D spin echo sequence. The sequence parameters were: TR/TE = 400/16 ms, FOV = 4.7 × 4.7 cm^2, matrix = 256 × 256, and averages = 2. Each scan lasted 3.5 minutes. Three contiguous 1.5 mm slices were acquired using two different orientations (Fig. 3-4). Slices in orientation 1 (O1) were aligned parallel to the cornea and placed near the posterior edge of the lens. Slices in orientation 2 (O2) were orthogonal to O1 and cut through the major axis and the

infusion site. One set of scans (O1 and O2) was acquired before the start of infusion. The infusion was then started at either 1 or 10 µl/min, and the eye was scanned continuously for 20-30 minutes. For rabbits infused intrascleral, the infusion was then halted and scanning continued until Gd-DTPA signal had cleared completely from the suprachoroidal space. All rabbits were euthanized by pentobarbital overdose (200-250 mg/kg) at the end of each MRI experiment. All experiments were repeated at least in duplicate.

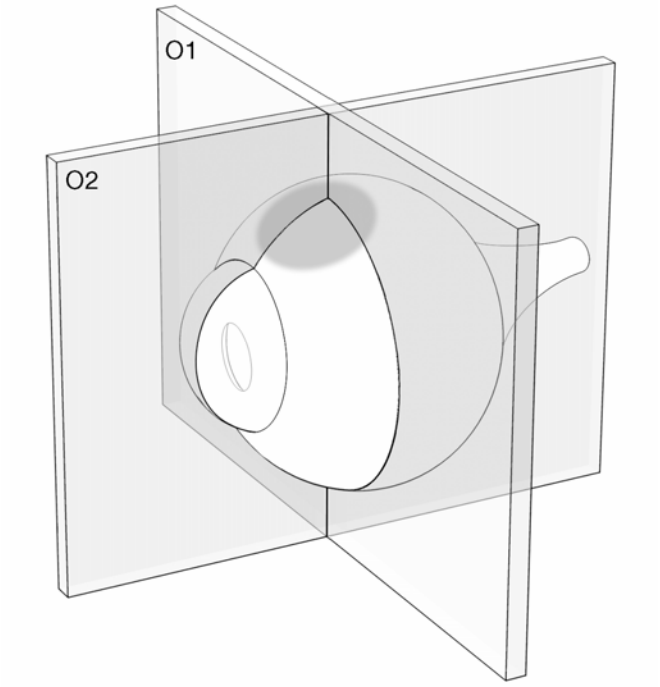

Figure 3-4. Positioning of slices in O1 and O2 shown on a schematic eye. Slices in both O1 and O2 intersect the site of infusion (shaded circle in gray).

3.2.3. Image Analysis

MR images were analyzed using ImageJ. Signal intensities from MR images were normalized to an average signal intensity from a region-of-interest (ROI) determined within the vitreous for each scan. We assumed that the concentration of Gd-DTPA within the vitreous was negligible during the time course of all experiments. Temporal analysis of the signal intensities from the vitreous region starting from the pre-injection scan to the end of the experiment indicated that its signal intensity value was relatively constant with values that were 5 to 10 times lower than the average signal intensity values from the suprachoroidal region. The signal intensities in the vitreous had a mean fluctuation of ±15% during the entire course of each experiment. Further support for the assumption of negligible vitreous concentration is derived on the basis of the low Gd-DTPA permeability of the ocular tissues (See Discussion).

To perform quantitative calculations of clearance rates for Gd-DTPA clearance from the suprachoriodal space, the normalized signal intensities for each pixel in an ROI were recorded and converted into Gd-DTPA concentration by using a calibration curve determined from various concentrations of Gd-DTPA in 2% HPMC samples in PBS (Fig. 2-12). The calibration curve was constructed by scanning the HPMC samples with the same MR imaging parameters used for the rabbit infusion experiments. The peak signal intensity of the calibration curve occurred at 5 mM, which was chosen as the infusion concentration. A similar calibration curve has been previously reported [58]. The lower detection limit of this technique was 0.1 mM.

The circumferential distribution and clearance rate of Gd-DTPA in the suprachoroidal space was determined from the 3 image slices acquired in O2 during intrascleral infusion experiments. The mass clearance rate of Gd-DTPA from the suprachoroidal space was calculated from the normalized signal intensity converted to concentration in each image by the following procedure: an ROI was established in each of the 3 slices from the last scan obtained before halting infusion to monitor the clearance of Gd-DTPA from the suprachoroidal space. The ROI consisted of a curved line that was drawn through the hyperintense suprachoroidal band. The ROIs were saved and superimposed onto the images of successive scans acquired during Gd-DTPA clearance. Normalized signal intensities for each pixel in an ROI were recorded and pixels with values near background intensity were discarded. The remaining pixels of the ROI were used to calculate a mean signal intensity which was converted into the average Gd-DTPA concentration of the suprachoroidal space.

The mass of Gd-DTPA for each image was determined by multiplying the average concentration of Gd-DTPA by the volume of the corresponding suprachoroidal space (number of pixels remaining in the ROI × pixel volume). The average mass of Gd-DTPA in the suprachoroidal space was computed using the mass values of the 3 slices. The average mass clearance of Gd-DTPA was fit to an exponential function, $M=Ae^{-kt}$, where M is the mass of Gd-DTPA in the ROI at time t, A is a constant, and k is the rate constant for clearance. The half-life was derived from the rate constant ($t_{1/2} = 0.693/k$). Regressions were also performed on semi-log plots of M vs. time and P-values of the goodness-of-fit of the exponential curve were computed.

3.2.4. Histology Study

Six rabbits were infused at 10 μl/min intrascleral under anesthesia with 5 mM Gd-DTPA for 1 hour to examine the eye histologically for toxicity. Two rabbits were euthanized and the infused eyes enucleated immediately upon death. The four remaining rabbits were recovered from anesthesia, and two rabbits were enucleated after 24 hours and the remaining two after 3 weeks. To limit the potential for fixation artifacts and to maintain the spatial relationship of the choroid and retina, enucleated eyes were immediately placed in plastic molds filled with embedding medium (Tissue-Tek O.C.T. Compound, Sakura Finetek, Torrance, CA, USA) and flash frozen at -80˚C. Frozen eyes were sectioned coronally at 10 μm slices on a cryostat at -20˚C and fixed in 4% paraformaldehyde after sectioning. Dried sections were stained with hematoxylin-eosin for light microscopy. Histological sections were also acquired from rabbits without prior infusion to serve as control images.

3.3. Results

Figure 3-5 shows an MR image acquired before infusion of Gd-DTPA. Many ocular structures can be delineated, including the layers of the cornea and defined structures of the ciliary body, lens and optic nerve. The conjunctiva, sclera and choroid/retina can also be identified, particularly in Figure 3-6D, as the conjunctiva and choroid/retina appear hyperintense and the sclera appears hypointense in a T_1 weighted image [142].

3.3.1. Subconjunctival Infusion

Most of the Gd-DTPA infused subconjunctival appeared to remain in the bleb formed by the conjunctival tissue (Fig. 3-6B and C). Increasing the infusion rate from 1 to 10 µl/min only increased the bleb size and did not contribute to any noticeable penetration of Gd-DTPA into the underlying tissues. Additional experiments were performed with 10 µl/min subconjunctival infusions lasting up to 2 hours (data not shown). However, a comparison of the scans to those acquired before infusion revealed that levels of Gd-DTPA were below the detection limit in the choroid/retina during the entire scan period.

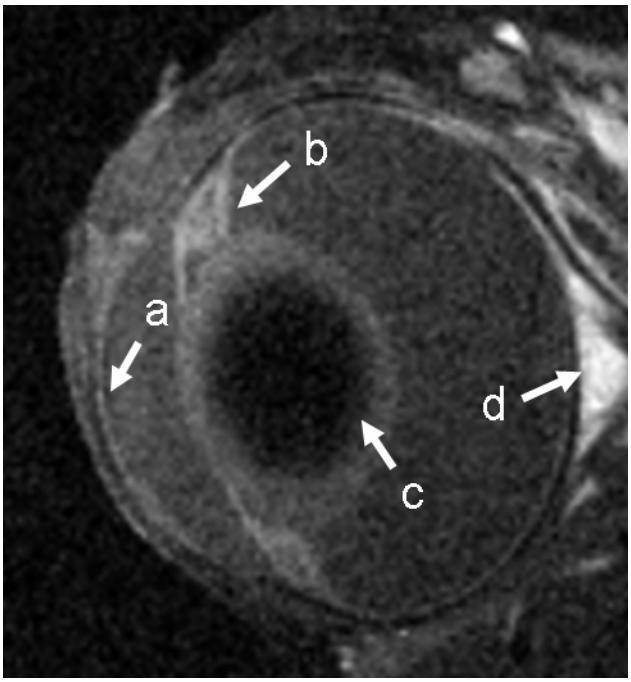

Figure 3-5. T_1 weighted MR image of the eye in O2 before infusion.

a: cornea, b: ciliary body, c: lens, d: optic nerve

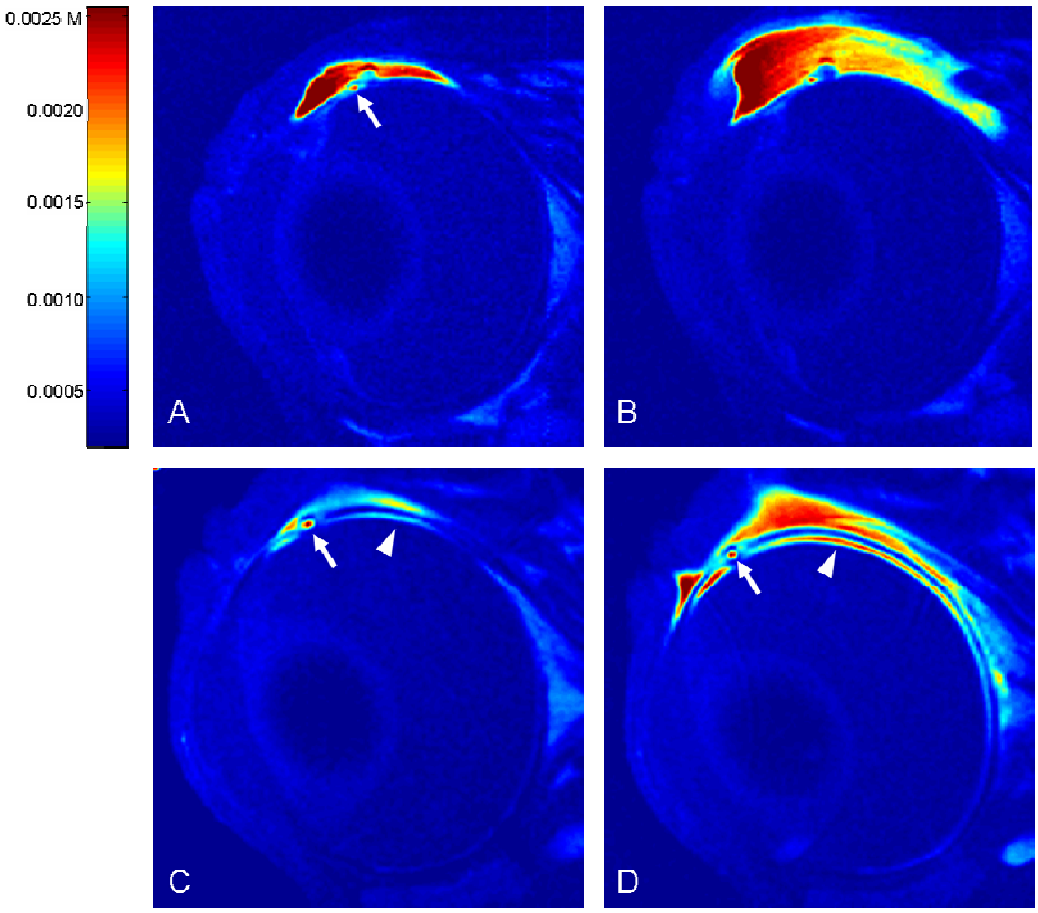

Figure 3-6. MR images of subconjunctival vs. intrascleral infusion.

After 42 minutes of subconjunctival infusion (A) at 1 µl/min and (B) at 10 µl/min. After 31.5 minutes of intrascleral infusion (C) at 1 µl/min and (D) at 10 µl/min. Arrows: catheter tubing; arrowheads: Gd-DTPA in suprachoroidal space. The color scale bar on the left indicates the signal intensity converted to concentration in Molar units.

3.3.2. Intrascleral Infusion

During intrascleral infusions, Gd-DTPA was seen to appear in the suprachoroidal space, indicated by the inner hyperintense band (Fig. 3-6C, D). Due to limited resolution, the distribution of Gd-DTPA in the inner choroid and retina was not discriminated. There was no Gd-DTPA detected in the anterior chamber with a small increase in signal intensity present in the ciliary body region near the catheter tip.

Gd-DTPA was detected in the suprachoroid immediately after the start of infusion at 1 and 10 µl/min. Gd-DTPA began to spread posteriorly in the suprachoroid from the infusion site. Figure 3-7 represents the distance traveled from the infusion site by the leading edge of the Gd-DTPA signal. After 7 minutes of 1 µl/min infusion, the posterior spread of Gd-DTPA in the suprachoroid reached a steady state and covered an average circumferential distance of 7 mm (Fig. 3-7). Prolonged infusion produced only a minimal increase in Gd-DTPA distribution. Figure 3-8 shows the spread of the Gd-DTPA signal in the O1 and O2 planes during a 10 ul/min intrascleral infusion. Increasing the infusion rate to10 µl/min caused Gd-DTPA to travel farther in the suprachoroidal space. This distance is shown in Figure 3-7 (squares). After 14 minutes of infusion Gd-DTPA had reached the optic nerve (Fig. 3-8F). Continued infusion increased the amount of Gd-DTPA in the suprachoroidal space. Gd-DTPA was also detected in the conjunctiva near the infusion site. This suggests that intrascleral catheters may also allow Gd-DTPA to partially infuse into the overlying conjunctiva.

A comparison of images taken in O1 (Fig. 3-8 A through D) and O2 (Fig. 3-8 E through H) show that Gd-DTPA is able to travel slightly farther by moving parallel to the limbus rather than in the posterior direction towards the optic nerve. This may be due to the transport and mechanical properties of the involved tissues but could also be influenced by the orientation of the catheter, which was placed parallel to the limbus rather than pointing towards the posterior pole of the eye.

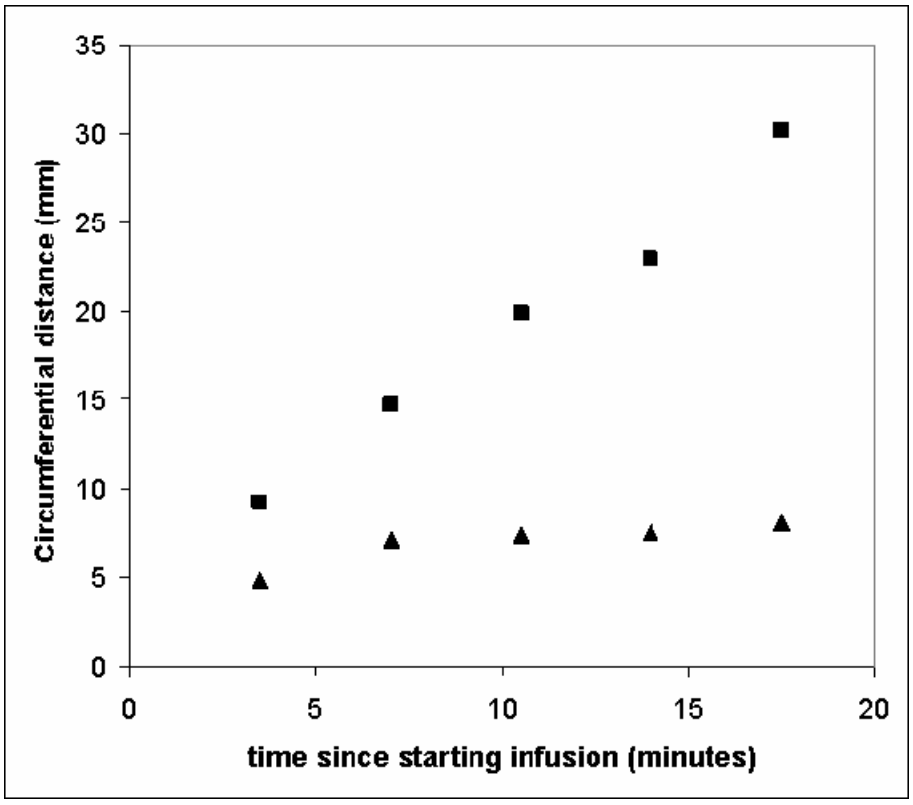

Figure 3-7. Spread of Gd-DTPA measured in the suprachoroidal space. Measurements taken from images in O2 during intrascleral infusion at 1 µl/min (triangles) and 10 µl/min (squares).

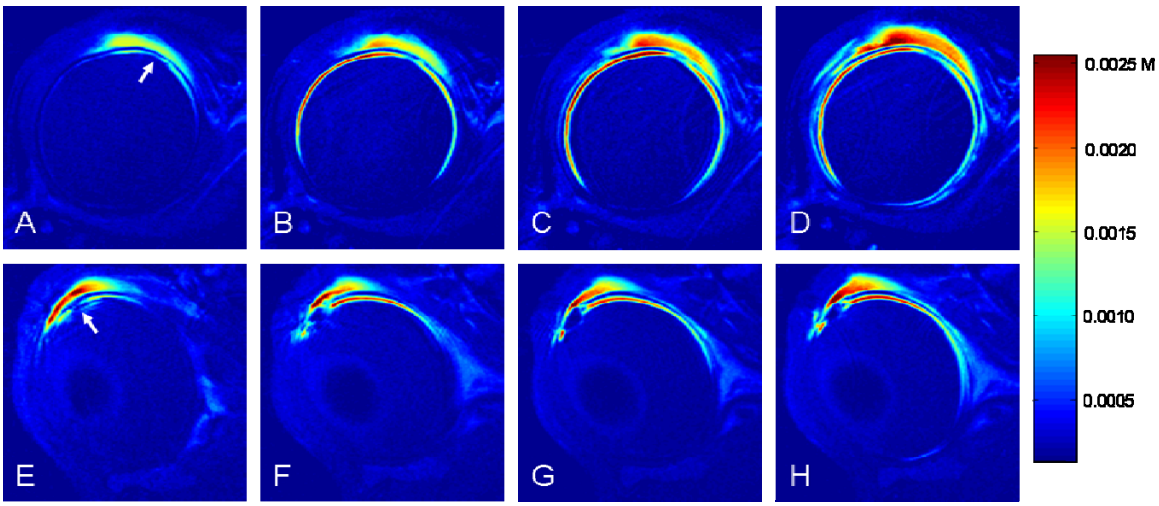

Figure 3-8. Time series MR images during intrascleral infusion.

Images acquired with O1 (A-D) and O2 (E-H) during 10 ul/min intrascleral infusion. Images in O1 after infusing for (A) 3.5 minutes, (B) 10.5 minutes, (C) 17.5 minutes, (D) 24.5 minutes. Images in O2 after infusing for (E) 7 minutes, (F) 14 minutes, (G) 21 minutes, (H) 28 minutes. Arrows indicate approximate location of catheter.

3.3.3. Suprachoroidal Clearance

Qualitatively, the MR images in Figure 3-9 show that the concentration of Gd-DTPA in the suprachoroidal space decreases uniformly after halting intrascleral infusion. Images shown in Figure 3-9 were positioned more obliquely than images shown in Fig. 3-8 E through H.

The clearance rate of Gd-DTPA from the suprachoroidal space was determined from a quantitative analysis of Gd-DTPA mass at sequential time points as described in the Methods. The rates of suprachoroidal clearance for 1 µl/min and

10 µl/min infusions are plotted in Figure 3-10 using the average mass from the 3 slices acquired in O2 for each scan. The clearance data shows a good fit to exponential equations (P-values in Figure 3-10 caption). This suggests that the mass clearance from the suprachoroidal space can be modeled as first-order for both 1 and 10 µl/min infusions, with half-lives of 5.4 and 11.8 minutes, respectively. Complete Gd-DTPA clearance from the suprachoroidal space after intrascleral infusion at 1 and 10 µl/min required approximately 20 and 60 minutes, respectively.

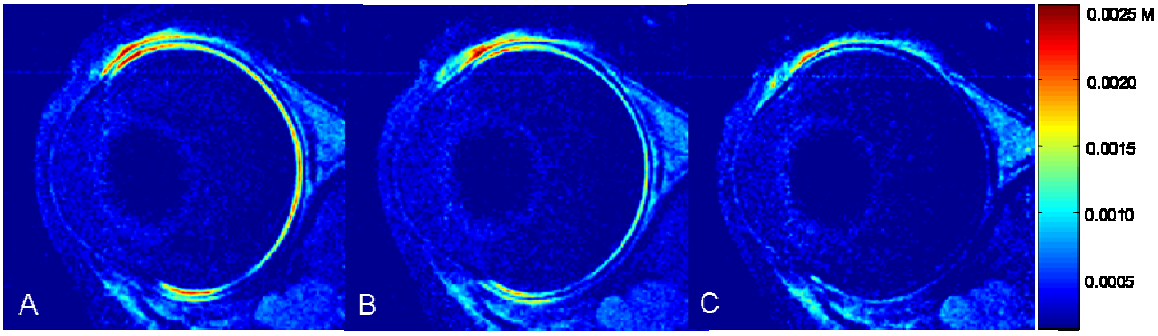

Figure 3-9. Time series MR images of suprachoroidal clearance.

(A) After intrascleral infusion for 23 minutes at 10 µl/min. After halting infusion for (B) 21 minutes and (C) 63 minutes.

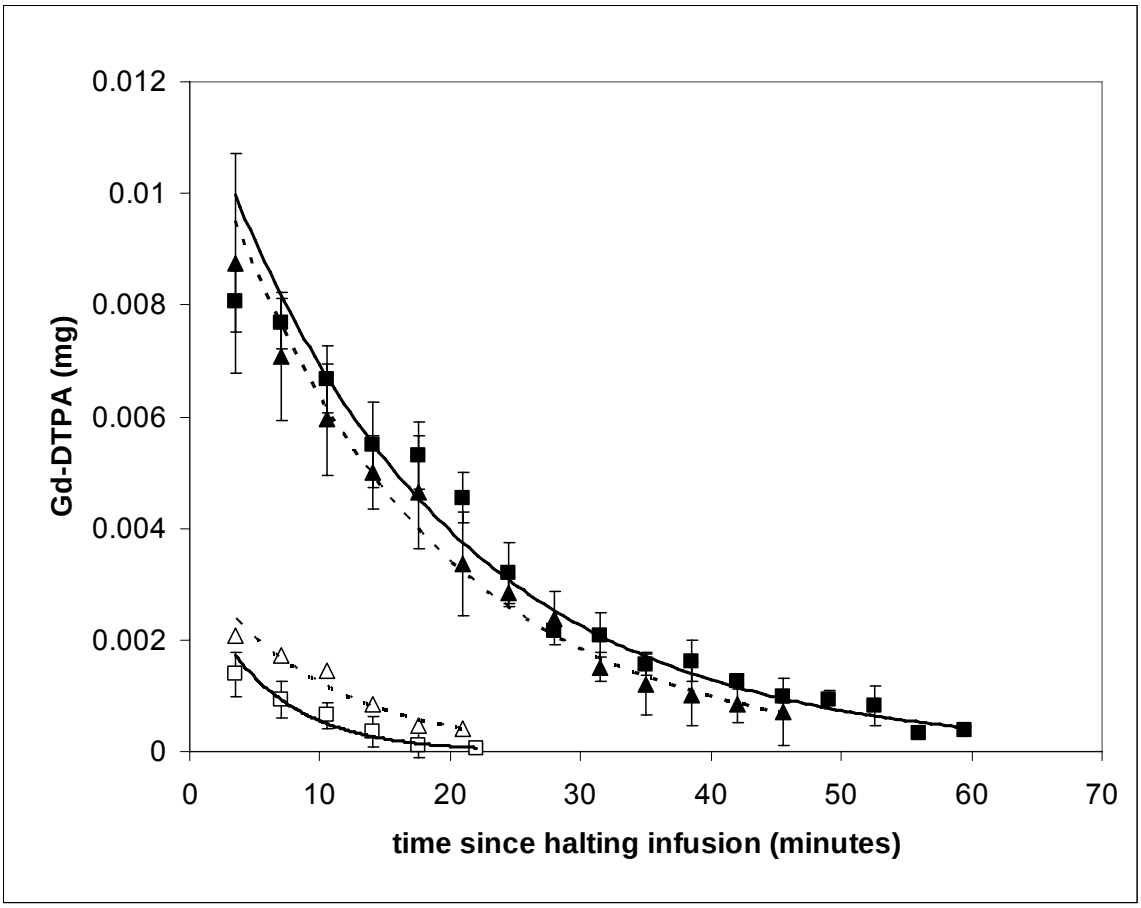

Figure 3-10. Suprachoroidal clearance after 1 and 10 µl/min intrascleral infusion.

Data points are mean ± SD of 3 slices. Triangles: rabbit 1; squares: rabbit 2. Open: 1 µl/min; filled: 10 µl/min. Dashed lines: exponential curve fit for rabbit 1; solid: rabbit 2. Average half-life: 5.4 min (1 µl/min), 11.8 min (10 µl/min). The goodness-of-fit P-values for all experiments were <0.0001 except for rabbit 1, 1 µl/min which was 0.001.

3.3.4. Histological Examination

Eyes enucleated immediately after 1 hour of 10 µl/min intrascleral infusion showed an expansion of the suprachoroidal space (Fig. 3-11). This indicated that much of the infused Gd-DTPA solution accumulated in the suprachoroidal space. In eyes enucleated 24 hours after infusion, the suprachoroidal space had normalized and tissue structures were no different from control images taken before infusion (Fig. 3-11A). Eyes enucleated 3 weeks after infusion also showed normal ocular tissues by light microscopy.

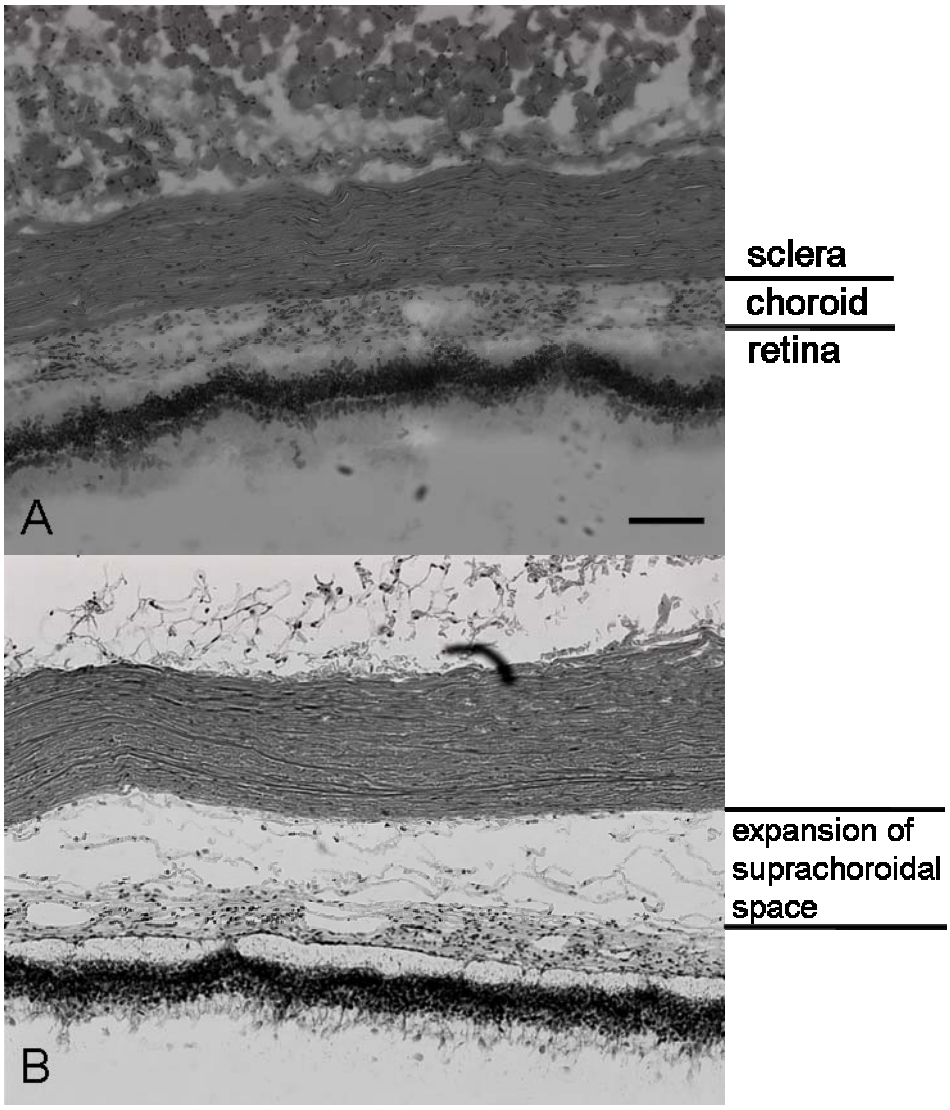

Figure 3-11. Histological images of the suprachoroidal space.

Hematoxylin-eosin stained light microscopy images. (A) Without infusion, (B) after 10 µl/min infusion for 1 hour. Scale bar represents 50 µm.

3.4. Discussion

3.4.1. Assessment of Sustained Drug Delivery by Continuous Infusion

Subconjunctival sustained infusions demonstrated no detectable levels of Gd-DTPA in the choroid/retina using dynamic MRI, possibly because of clearance by conjunctival blood vessels and lymphatics [52,105] and by rapid removal of any agent that does diffuse to the choroid. The results from this study show that the concentration of Gd-DTPA in the choroid/retina was under the MRI detection limit after sustained subconjunctival delivery by continuous infusion.

In contrast, intrascleral infusions expanded the suprachoroidal layer and rapidly delivered Gd-DTPA circumferentially and posteriorly with very limited anterior segment exposure. Our results indicate that higher infusion rates allow greater distribution of Gd-DTPA in the suprachoroidal space. While intrascleral infusions of 10 μl/min achieved Gd-DTPA delivery to the optic nerve after 15 minutes, infusions of 1 μl/min localized the spread of Gd-DTPA near the infusion site. The rate of infusion and clearance may have reached equilibrium during 1 μl/min infusions, and this may account for the steady state in spatial distribution of Gd-DTPA in the suprachoroidal space.

The suprachoroidal space is a virtual space and is avascular, consisting of loose connective tissue [63,144]. It was assumed that after intrascleral infusion the suprachoroidal space consisted mostly of Gd-DTPA solution (as shown by histology), and that this could be adequately modeled using a polymer solution. Gd-DTPA calibrations were not made for other ocular tissues (sclera, choroid, retina), since

quantitative calculations were only performed for the Gd-DTPA signal present in the suprachoroidal space.

3.4.2. Assessment of Suprachoroidal Delivery

Although the suprachoroidal clearance data from this study was obtained from a portion of the globe, an estimate of the amount of Gd-DTPA present in the entire suprachoroidal space after 30 minutes of infusion at 10 µl/min can be calculated by multiplying the average suprachoroidal Gd-DTPA concentration by the volume of the suprachoroidal space. Adapting a methodology for the calculation of the scleral surface area [145], the surface area of the suprachoroid was approximated as 8 cm^2. The suprachoroidal space is included within a volume of 8 cm^2 multiplied by the pixel width (0.184 mm). This yields an approximate apparent volume of 150 mm^3. Since the average concentration of Gd-DTPA after 30 minutes of infusion is about 0.001 M, the estimated mass of Gd-DTPA in the suprachoroidal space is approximately 0.14 mg. This value represents about 10 % of the total infused amount of Gd-DTPA.

Suprachoroidal clearance of Gd-DTPA was rapid, and the agent was undetectable in the eye after about 1 hour following a 10 µl/min infusion. Clearance of Gd-DTPA followed first-order kinetics and the average half-life after a 30-minute 10 µl/min infusion was approximately double that of a 1 µl/min infusion. Although the higher infusion rate increased the half-life, the fast elimination of Gd-DTPA from the suprachoroidal space suggests that infusions may need to be maintained for a defined time period to successfully deliver desired amounts. The actual mechanisms

responsible for the decrease of Gd-DTPA are not known but could include diffusion and convection through the sclera [64,65], uptake by the choriocapillaris [146], and movement of tracer laterally out of the plane of the image slices. The pressure created by the solution infused into the eye may also contribute to the elimination of Gd-DTPA.

In calculating the suprachoroidal mass clearance of Gd-DTPA, the number of pixels in the ROI that were above background signal intensity decreased with time, and this may reflect the volume decrease of the suprachoroidal space after halting infusion. While the data from this study is insufficient to determine if the decrease in Gd-DTPA mass is due to the decrease in volume, the normalization of the suprachoroidal space over time indicates that fluid may also be cleared from the suprachoroidal layer.

The expansible capabilities of the suprachoroidal layer have been demonstrated clinically where large choroidal effusions following glaucoma filtering procedures can resolve without sequelae [147]. Previous animal studies with deliberate expansion of the suprachoroidal space with volumes of hyaluronate > 300 µl show complete resolution without toxicities [148,149]. Our histological studies with rabbits that were infused intrascleral at 10 µl/min for 1 hour showed that the suprachoroidal layer could expand and contract without affecting tissue morphology and structure. This suggests that intrascleral infusions at rates of up to 10 µl/min for 1 hour can be safely performed in rabbits.

Technological advances with programmable implantable pumps across many specialties can potentially be applied to deliver drugs in the sclera for an extended

period of time [150-152]. Since there are no implantable infusion pumps approved for ocular drug delivery, a 15-minute intrascleral infusion using an external pump may be feasible to deliver a sustained-release formulation into the suprachoroidal space over the macular region [153,154]. The suprachoroidal space would serve as a reservoir for a sustained-release formulation that establishes a steep concentration gradient for drug diffusion into the choroid and retina. Investigators have directly accessed the posterior segment through the suprachoroidal space using either a rigid [153] or flexible cannula [154]. Following placement of a cannula behind the porcine eye via the suprachoroidal space and injection of a triamcinolone acetonide depot posteriorly, pharmacokinetic studies showed high local drug concentrations in the choroid and retina in the macular region for at least 4 months [154]. The flow-assisted delivery system used in our study may be a safer alternative since mechanical damage from the catheter tip, such as choroidal tears and optic nerve injury, would be avoided [154]. Diffusion-based implants have also been used for drug delivery to the retina through the suprachoroidal space requiring surgical incisions for placement of the implant [19,155]. However, the implant insertions, requiring incisions through the sclera and dissection to the suprachoroidal space, are invasive and may have a greater potential for adverse events.

3.4.3. Advantages and Limitations in using MRI for Drug Delivery Assessment

In this study we used a custom-built surface coil to acquire high resolution scans of the eye. The surface coil localizes the magnetic field to a smaller region and permits higher spatial resolution. An in-plane resolution of 0.184 × 0.184 mm was

achieved, which was sufficient to delineate several tissues comprising the eye wall. Higher resolutions have been reported in ophthalmic MRI [156], but were unable to utilize these scanning methods in this study due to limitations in temporal resolution. As described in Chapter 2, there is always a compromise between spatial and temporal resolution, and higher resolutions may be achievable in measuring processes with slower dynamics.

To achieve high resolution, we were only able to scan a portion of the orbit (3 contiguous slices), and a 3-dimensional scan could not be achieved in our desired time frame. For this particular study, assessment of drug delivery was feasible by analyzing 2D slices, since a major goal was to visualize the posterior distribution of drug by infusional delivery. Depending on the desired outcome measurements, however, a 2D imaging technique may not always suffice, and spatial and temporal resolution may have to be sacrificed in order to achieve 3D imaging.

Despite the high resolution we were able to achieve with the surface coil, there were still limitations in sensitivity and resolution which prevented the detection of low levels of Gd-DTPA in the choroid/retina and vitreous and the delineation of the plane between the neurosensory retina and choroid. The spatial resolution used in this study also could not clearly separate the Gd-DTPA solution filled suprachoroidal space from the choroid/retina. Partial volume averaging may contribute to error in calculation of the Gd-DTPA mass clearance rate. The dynamics of suprachoroidal Gd-DTPA distribution during and after infusion are rapid, and fast scan times were necessary to acquire a sufficient number of images for clearance rate determination.

In addition to the MRI issues of spatial and temporal resolution, there were several other limitations in this study. One has to be cautious in extrapolating ocular imaging data from rabbit to human given the relative differences in the size of the eye, scleral thickness, choroidal flow velocities, and degree of retinal vascularization [157-159]. In addition, the results of the ocular distribution and clearance of Gd-DTPA cannot be generalized to all drugs because of differences in properties relevant to drug transport [3,20,41,143]. The effect of pigment binding in the uvea can influence drug transport, but this is not studied appropriately in albino rabbits.

In this study, the concentration of Gd-DTPA in the vitreous was assumed to be below the detection limit of 0.1 mM at all times for all experiments. We normalized all signal intensity values to the vitreous signal intensity which we assumed to have negligible concentrations Gd-DTPA. We feel that this assumption is justified on the basis of the low infusion concentration (5 mM), the limited time course of our image acquisitions, and low the permeability of the retina-choroid-sclera membrane (2.0×10^{-6} cm/sec) [58] to Gd-DTPA. Using higher concentrations of Gd-DTPA may produce lower signal intensities near the infusion site due to T_2 shortening effects, but the concentration of Gd-DTPA in the vitreous may rise above detection limits and allow measurement of Gd-DTPA concentration levels. As previously mentioned in the Methods, the average signal intensity of the vitreous did not significantly change during the duration of the experiments of our study. Longer scan times may allow greater amounts of Gd-DTPA to accumulate in the vitreous, producing higher signal intensities.

DCE-MRI has been shown to be useful in determining pharmacokinetic and physiologic properties [160,161]. Studies involving ocular pharmacokinetics with MRI have been previously reported [132,162,163]. MRI pharmacokinetics is an emerging field [160,164] and the improved resolution with newer generation scanners [165] will allow for non-invasive pharmacokinetic analysis in pre-clinical evaluation of ocular drug delivery systems.

3.5. Conclusion

An intrascleral continuous infusion was successful in transporting Gd-DTPA to the posterior segment from an anterior infusion site with limited anterior segment exposure. The suprachoroidal space appears to be an expansible conduit for drug transport to the posterior segment and may be able to deliver drugs to the macular region.

The results from this study also demonstrate the advantages and limitations in the DCE-MRI technique. While a surface coil was used to improve resolution, only a portion of the globe could be scanned since a 3D scan could not be completed within the desired time frame. However, the use of the surface coil produces high resolution images of the eye, and the conjunctiva, sclera and choroid/retina can be clearly delineated. A 2D scanning technique utilizing a surface coil designed for optimal imaging of the eye can be useful in assessing drug delivery techniques in which high spatial resolution is crucial for outcome measurement.

Chapter 4: Drug Elimination Kinetics after Subconjunctival Injection

4.1. Introduction

As discussed in Chapter 1, subconjunctival injections are one form of transscleral drug delivery. Subconjunctival injections are routinely performed in patients to administer drugs such as corticosteroids [166] and antibiotics [167] for ocular treatment. Drug solutions injected into the subconjunctival space form a localized depot, which may allow for long-term sustained delivery. After subconjunctival injection, drugs penetrate the eye directly through the underlying tissues [111] and therapeutic concentrations can be achieved in the vitreous [168]. While subconjunctival injections are commonly performed, the retention time of drug and the rate of drug elimination from the depot are unknown and have not been investigated in detail.

Previous methods of examining the change in drug levels in the subconjunctival space after injection include extracting drug from the excised depot [169] and using a scintillation counter to measure the rate of loss of gamma-emitting materials [170]. Drug extractions are inefficient since they require the use of multiple animals and it is also difficult to successfully remove the entire depot for analysis. The measurement of gamma-emitting compounds can give quantitative results *in vivo* but lacks information on spatial distribution. Magnetic resonance imaging has recently been introduced as a non-invasive approach to assess the subconjunctival delivery of ionic permeants [106]. The study by Li et al analyzed concentration

levels of Mn^{2+} and $MnEDTA^{2-}$ in the anterior chamber, posterior chamber, and the vitreous to assess the permeation and clearance of model ionic permeants. In our study, we measured the concentration levels of model drugs injected into the subconjunctival space using three-dimensional DCE-MRI. The rate of drug clearance was determined by following the concentration changes of the injected contrast agent from the local depot.

Recent studies have demonstrated that elimination mechanisms present *in vivo* such as conjunctival lymphatic clearance and blood flow can significantly reduce the penetration of drugs to the vitreous [105] and anterior chamber [106] after transscleral delivery. The effect of dynamic clearance mechanisms on drug concentration levels in the subconjunctival space was studied by performing experiments *in vivo* and *post mortem*. Two different contrast agents, Gd-DTPA (590 Da) and Gd-albumin (67.5 kDa), were used as model drugs to understand the effect of molecular weight on clearance rate. The effect of injection volume was also studied by administering different volumes (60, 200, and 600 μl) of Gd-DTPA.

4.2. Methods

4.2.1. Animal Setup

Female New Zealand White rabbits weighing 3-3.5 kg were monitored under general anesthesia during the entire MRI scan period. Proparacaine 1% ophthalmic drops (Allergan America, Hormigueros, PR) were used topically on the eye. The superotemporal quadrant was exposed by placing a 9-0 vicryl suture at the limbus and rotating the eye downward. A 24 gauge × ¾ inch long intravenous catheter was

prepared as described in Chapter 3. The catheter was then inserted through the eyelid and advanced at least 5 mm superonasally under the conjunctiva. The needle was carefully withdrawn, leaving the tip of the catheter under conjunctival tissue (Fig. 4-1). The catheter was held in place by the puncture through the eyelid. The eyelids were closed with tissue adhesive (Vetbond, 3M Animal Care Products, St. Paul, MN) and the tip of the catheter was connected to 7 m of PE-10 tubing by a 10 cm length of silicone tubing (0.025" ID × 0.047" OD). The silicone tubing was glued on one end to the PE-10 tubing and prefilled with contrast solution before connecting to the catheter by a friction fit. The tubing was prefilled with either Gd-DTPA diluted to 1 mM in PBS or Gd-albumin diluted to 0.1 mM protein in PBS before connecting to the catheter. The contrast solution was faintly colored with 100 mg/mL sodium fluorescein to a final concentration of 0.5 mg/mL to enhance visibility of the fluid in the tubing. The bolus was administered after the rabbit was placed into the magnet and preliminary scans were acquired. The contrast solution was injected outside the scan room through a 1 mL syringe joined to the tubing with a 30 gauge needle.

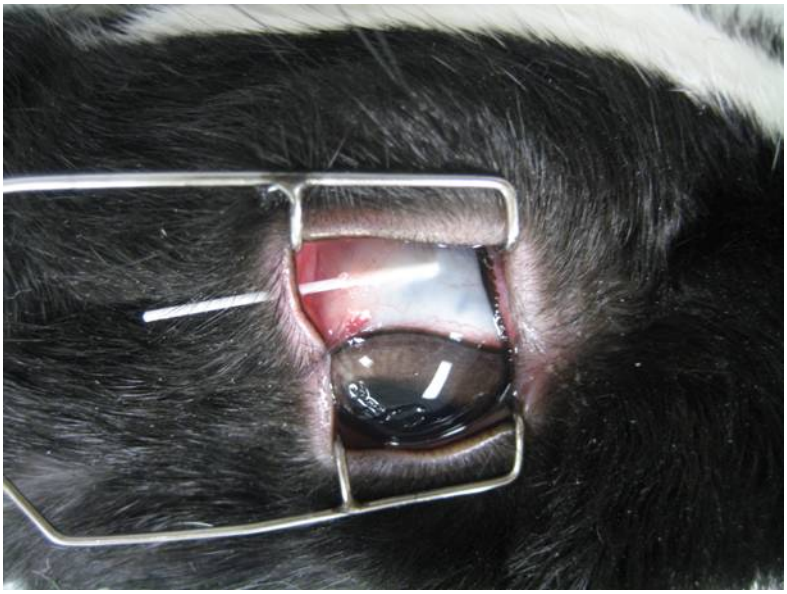

Figure 4-1. Photograph of subconjunctival catheter placement.

Catheter remaining in the eye after subconjunctival insertion. The open end is connected to a syringe located outside the scan room by 7 m of PE-10 tubing.

4.2.2. MRI Setup

Two 2 mL glass vials filled with PBS and the injection contrast solution were taped over the eye as reference standards. The rabbit was placed on a cradle and the entire head inserted in a volume coil (Fig. 4-2). T_1-weighted images were acquired using a 3D gradient echo sequence. The sequence parameters were: TR/TE = 40/5 ms, FOV = 9 cm × 4.59 cm × 9 cm, matrix = 256 × 128 × 128, pulse angle 30° and NEX = 1. The FOV was positioned to capture both eyes and the two standard solutions and the pixel resolution was 0.703 mm × 0.179 mm × 0.703 mm. One scan was acquired before bolus injection with each scan lasting 11 minutes. After

injection, scans were acquired in continuous succession for at least 3 hours for 60 and 200 µl injections and 5 hours for 600 µl injections. All rabbits were euthanized by pentobarbital overdose (200-250 mg/kg). Rabbits used for *in vivo* experiments were euthanized immediately after completion of the experiment, while rabbits used for *post mortem* experiments were euthanized within one hour prior to the start of the scan. A heating pad was used in *post mortem* experiments to maintain body temperature at 37 ˚C. All experiments were repeated at least in triplicate.

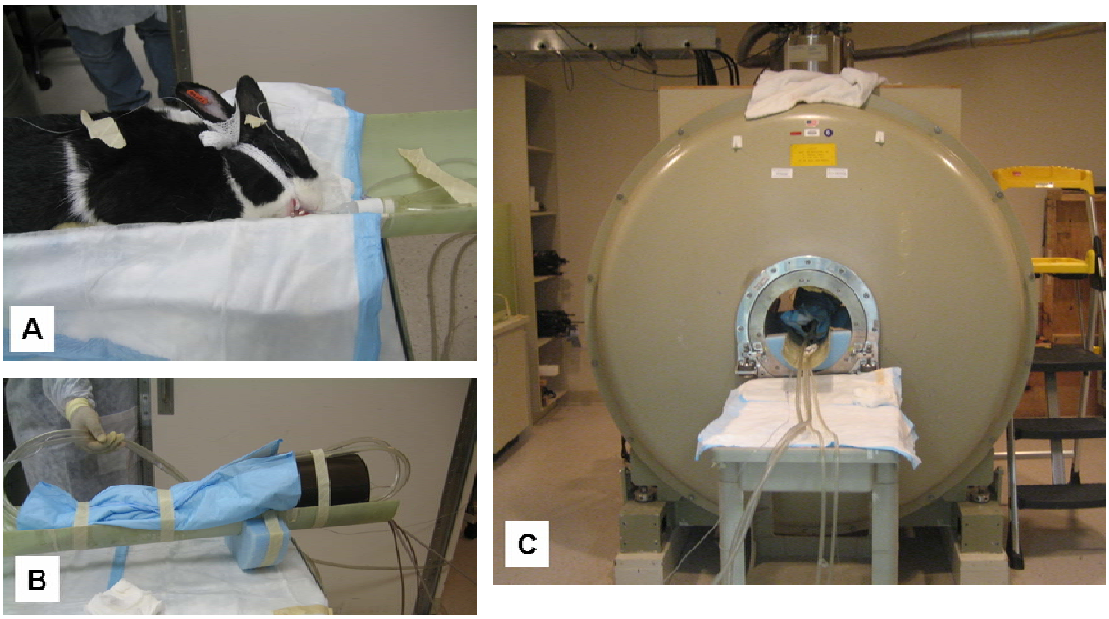

Figure 4-2. Rabbit setup in magnet.

(A) Rabbit after intubation, (B) rabbit head positioned inside volume coil, and (C) rabbit and cradle positioned inside the bore of the main magnet.

4.2.3. Image Analysis

MR images were analyzed using a program written in MATLAB (Mathworks, Natick, MA) designed to read and display Bruker file images. To convert signal intensities into concentration values of Gd-DTPA and Gd-albumin, a signal intensity vs. concentration calibration curve was constructed by scanning samples of varying concentrations of contrast agent in PBS using the same MR imaging parameters as the rabbit experiments. The calibration curves were shown previously, in Figures 2-11 and 2-13. Since injections were performed using large solution volumes and most of the subconjunctival bleb consisted of fluid, PBS was assumed to adequately model the fluid-filled tissue. The calibration curve was constructed by scanning the PBS samples using the same MR imaging parameters used for the rabbit experiments.

To obtain concentration values of the contrast agent in the subconjunctival tissue after injection, the entire 3D image set was normalized to the signal intensity of the contrast agent standard at each time point. The images were set to a threshold signal intensity level equivalent to a concentration of 0.03 mM for Gd-DTPA and 0.005 mM for Gd-albumin (detection limit). This allowed the subconjunctival bleb to be defined clearly as pixels containing only background noise and tissues with trace or no amounts of contrast agent were omitted.

Analysis was performed on individual slices which were all taken from one of the three dimensions. The in-plane resolution of the images used in analysis was 0.703×0.179 mm. For each slice that contained visible pixels in the subconjunctival tissue after thresholding, an ROI was manually drawn around the hyperintense bleb. The signal intensity of each pixel in the ROI was converted to a concentration of Gd-

DTPA or Gd-albumin using the signal intensity vs. concentration calibration curve. After converting the signal intensity value to concentration for each pixel in the ROI, the mass of contrast agent in each pixel was computed by multiplying the pixel volume (0.089 mm^3) by concentration. By taking the sum of the mass of contrast agent in each slice, the total mass of contrast agent in the subconjunctival tissue was computed for each time point. The number of pixels that were included in each ROI was also recorded and multiplied by the pixel volume to obtain the total volume of the subconjunctival tissue at each time point. The average concentration of contrast agent in the subconjunctival tissue was calculated by dividing the total mass by the total volume.

The mass clearance data was fit to an exponential function, $M=Ae^{-kt}$, where M is the total mass of contrast agent in the subconjunctival space at time t, A is a constant, and k is the rate constant for clearance. Regressions were performed using Microsoft Excel (Microsoft Corporation, Redmond, WA) on semi-log plots of M vs. time, and values of k were computed from each experiment. The half-life was derived from the rate constant ($t_{1/2} = 0.693/k$).

4.2.4. Cryotherapy Procedure

A previous study [52] utilized cryotherapy to selectively eliminate clearance of drug from choroidal circulation. To examine the effect of cryotherapy on drug elimination after subconjunctival injection, cryotherapy was performed on the right eye of healthy rabbits at the injection site of the superotemporal quadrant. A single freeze/thaw cycle was performed to preserve the conjunctival vasculature and sclera

and produce a chorioretinal scar. A 2.5 mm retinal probe attached to a Keeler CTU CO_2 cryo unit (Keeler Instruments, Broomall, PA) was used to perform cryotherapy at a temperature of -60 ˚C. A total of eight adjacent cryotherapy applications in two horizontal rows were placed 4 mm from the limbus. The rabbits were utilized for MRI scanning at least 4 weeks after mature chorioretinal scar formation. Previous studies have indicated that this time frame is sufficient to ensure the permanent local damage of choroidal vasculature [52,171,172].

The cryotherapy treated rabbits were scanned according to the same surgical and experimental procedures as outlined in previous sections, with the catheter placed directly over the cryo-treated site.

At least 3 cryotreated eyes were also enucleated and sectioned according to methods outlined in section 3.2.4. for histological analysis.

4.3. Results

Figures 4-3 and 4-4 show serial images acquired immediately after a 200 µl and 600 µl subconjunctival injection of Gd-DTPA, respectively. The images show a comparison of the *in vivo* and *post mortem* scans. The color bar indicates the concentration of Gd-DTPA determined after conversion from signal intensity. Immediately after injection, the Gd-DTPA solution appears as a localized depot in the subconjunctival space at a high concentration. Over time, the concentration of Gd-DTPA in the subconjunctival bleb decreases dramatically *in vivo* for both injection volumes. About 3 hours post-injection of 200 µl and 4 hours post-injection of 600 µl, most of the Gd-DTPA molecules have disappeared from the depot *in vivo*. However,

in the *post mortem* case for both injection volumes, the Gd-DTPA concentration decrease is not nearly as significant.

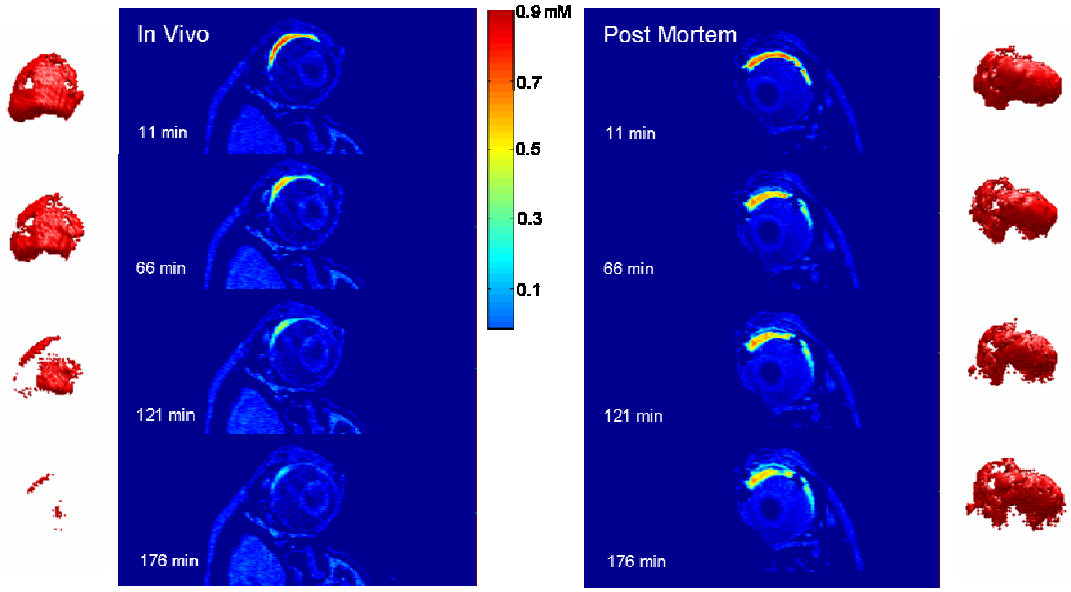

Figure 4-3. MRI scans of 200 µl Gd-DTPA.

Images acquired during *in vivo* and *post mortem* experiments after 200 µl Gd-DTPA injection. Times indicate minutes after injection. The volume occupied by Gd-DTPA is also shown in red by 3-dimensional reconstruction.

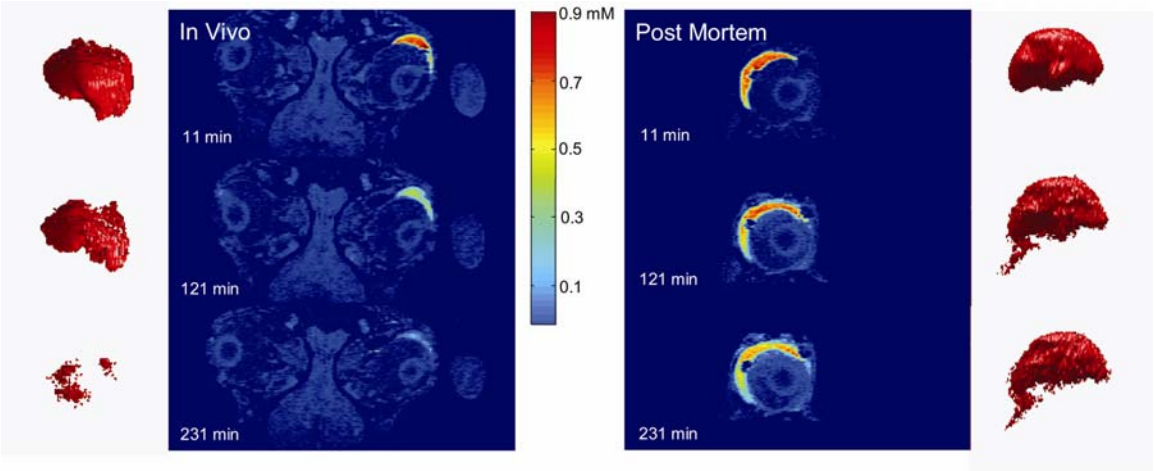

Figure 4-4. MRI scans of 600 µl Gd-DTPA.

Images acquired during *in vivo* and *post mortem* experiments after 600 µl Gd-DTPA injection.

The Gd-DTPA mass clearance data for 200 and 600 µl injection experiments is plotted in Figures 4-5A (*in vivo*) and 4-5B (*post mortem*). The plots also show the regression lines for the exponential fit of the mass data. Table 4-1 lists the average mass clearance rates (k) determined from individual regressions. While the k value for the 600 µl injection data appears to be less than the k value for the 200 µl data *in vivo*, the results from a one-tailed Mann-Whitney U test reveals that this difference is not significant for p=0.05 (Table 4-2). Similarly, the k value after a 60 µl injection (0.0372 min^{-1}) is not significantly different from the k value after a 200 µl injection *in vivo*. However, the difference in k values becomes significant when comparing the 60 µl injection to the 600 µl injection data, as shown in Tables 4-1 and 4-2.

Contrast agent, injected volume	k (*in vivo*) (min^{-1})	Half-life (hrs)	k (*post mortem*) (min^{-1})	Half-life (hrs)
Gd-DTPA, 60 µl	0.0372 ± 0.0032	0.31	--------	-----
Gd-DTPA, 200 µl	0.0273 ± 0.0145	0.42	0.0029 ± 0.0007	3.3
Gd-DTPA, 200 µl, CRYO	0.0336 ± 0.0043	0.35	--------	-----
Gd-DTPA, 600 µl	0.0247 ± 0.0071	0.47	0.0028 ± 0.0010	4.1
Gd-albumin, 200 µl	0.0022 ± 0.0010	5.3	0.0009 ± 0.0004	12.8

Table 4-1. Summary of average rate constants ± SD acquired *in vivo* and *post mortem*.

Figures 4-3 and 4-4 also present three-dimensional visual reconstructions of the apparent volume of Gd-DTPA, which were created by merging the slices that crossed through the subconjunctival bleb. These reconstructions are shown adjacent to the MR images at each respective time point. The apparent subconjunctival volume occupied by Gd-DTPA decreases dramatically *in vivo* while the *post mortem* scans show a slight increase in volume. This effect is also shown in Figures 4-5C and 4-5D which are plots of the apparent Gd-DTPA volume in the subconjunctival space. Figures 4-5E and 4-5F are plots of the average concentration of Gd-DTPA in the subconjunctival space. They show a decrease in average concentration for all experiments.

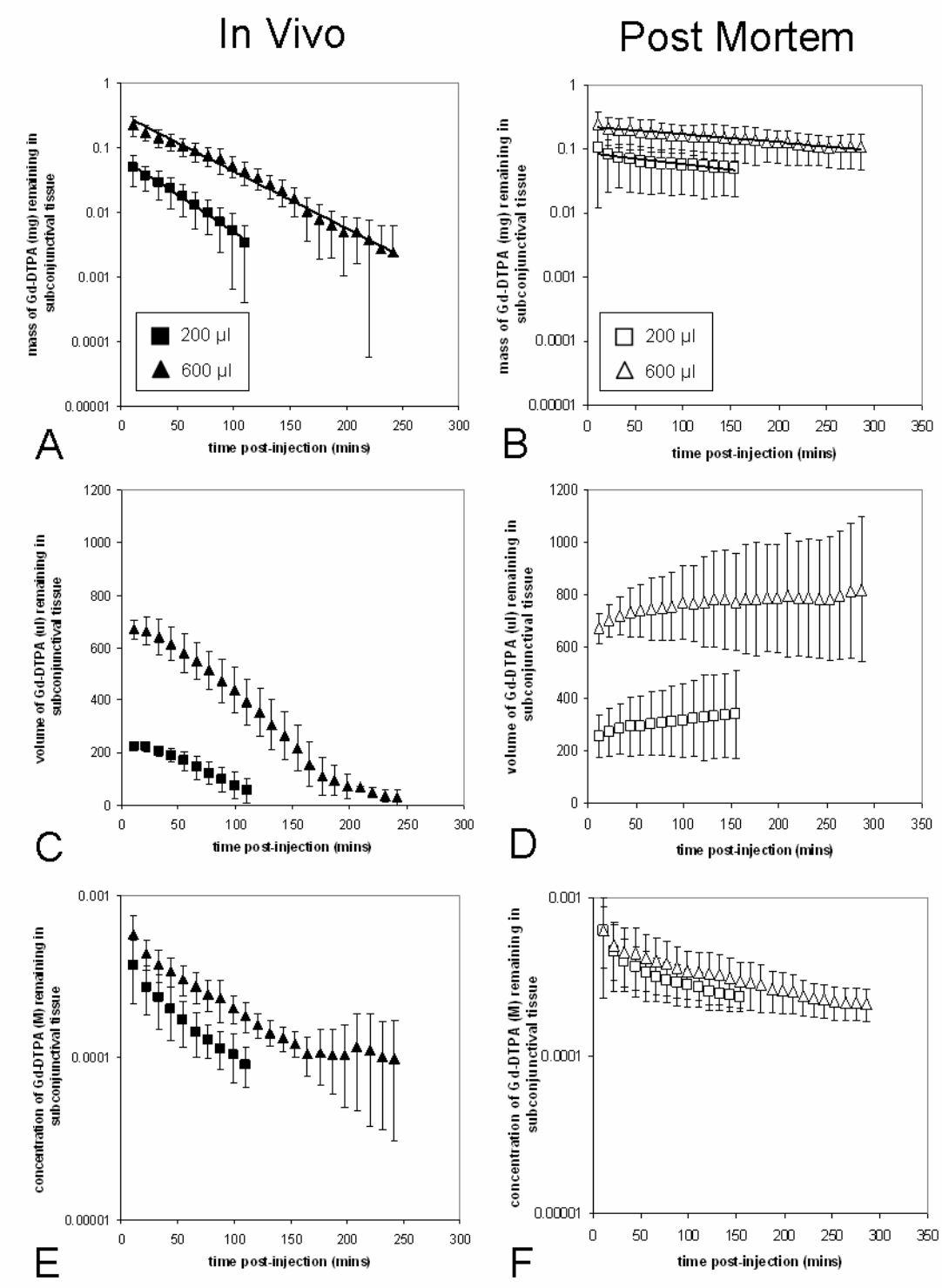

Figure 4-5. Plots comparing Gd-DTPA *in vivo* and *post mortem*.

Gd-DTPA change in mass, apparent volume and average concentration after 200 µl and 600 µl subconjunctival injection *in vivo* (A, C, E) and *post mortem* (B, D, F).

Values are given as mean ± SD. Lines indicate regression for mass clearance data. r^2 values: ■=0.99, ▲=0.99, □=0.84, △=0.97.

Test	Significantly different?
In vivo* vs. *post mortem	
Gd-DTPA, 200 µl	yes
Gd-DTPA, 600 µl	yes
Gd-albumin, 200 µl	no
Effect of volume, *in vivo*, Gd-DTPA	
60 µl vs. 200 µl	no
200 µl vs. 600 µl	no
60 µl vs. 600 µl	yes
Gd-DTPA vs. Gd-albumin	
in vivo, 200 µl	yes
post mortem, 200 µl	yes
Cryo vs. control	
Gd-DTPA, 200 µl, *in vivo*	yes

Table 4-2. Results from the Mann-Whitney U test for U(0.05).

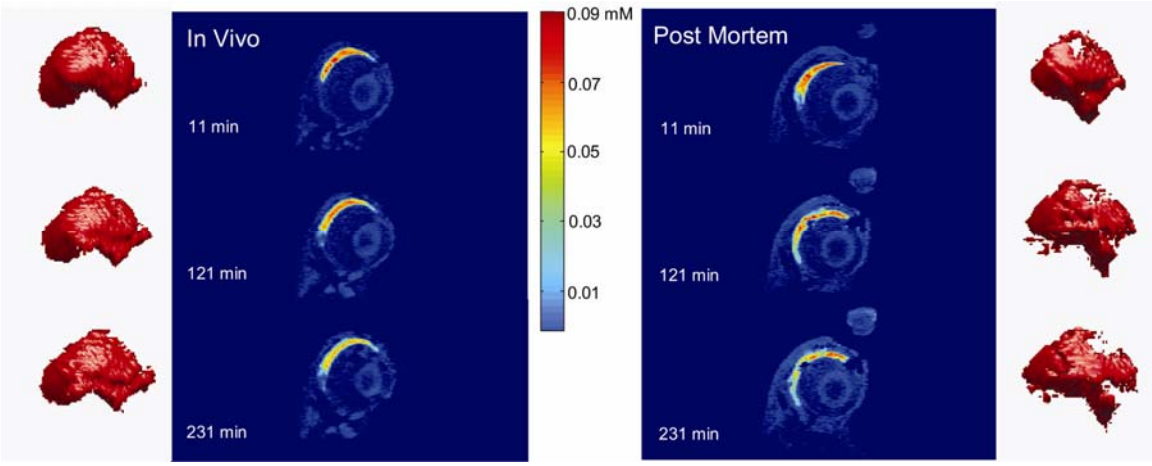

Figure 4-6. MRI scans of 200 µl Gd-albumin.

Images acquired during *in vivo* and *post mortem* experiments after 200 µl Gd-albumin injection. The volume occupied by Gd-albumin is also shown in red by 3-dimensional reconstruction.

MR images from 200 µl injections of Gd-albumin are shown in Figure 4-6. A comparison of the *in vivo* Gd-albumin images in Figure 4-6 to the *in vivo* Gd-DTPA images in Figure 4-3 for the 200 µl injection volume indicates that the concentration of Gd-albumin decreases more slowly with time compared to Gd-DTPA. This observation is further substantiated by the quantitative representation of mass clearance given in Figures 4-7A (DTPA) and 4-7B (albumin). The average *in vivo* half life of Gd-DTPA is 22 minutes and of Gd-albumin is 5.3 hours, as presented in Table 4-1. Figures 4-7A and 4-7B also show that the *post mortem* decline of Gd-albumin concentration is about 4 times slower than the *post mortem* decline of Gd-

DTPA for the 200 µl injection experiments, as evidenced by the calculated half lives which are given in Table 4-1.

The mass clearance data in Figure 4-7B shows a slightly faster decrease of Gd-albumin *in vivo* compared to Gd-albumin *post mortem*. Table 4-1 gives the respective half lives as 5.3 hours *in vivo* and 12.8 hours *post mortem*. However, a one-tailed Mann-Whitney U test ($p=0.05$) suggests that the difference between the *in vivo* and *post mortem* clearance rates is not significant for Gd-albumin (Table 4-2).

The apparent volume of Gd-albumin shows a slight increase *post mortem* (Fig. 4-8D). A similar effect is seen in Figure 4-7C for the volume of Gd-DTPA *post mortem*. The *in vivo* volume of Gd-DTPA shows a considerable decrease, whereas that of Gd-albumin is less prominent. The faster decrease in volume of Gd-DTPA may reflect the higher clearance rate of Gd-DTPA than Gd-albumin from the subconjunctival space, since the volume decrease is due to the reduction in the number of pixels with signal intensities above the threshold.

Figures 4-7E and 4-7F show a decrease in average concentration of Gd-albumin in the subconjunctival space for all experiments. This trend also correlates with the images shown in Figure 4-6, which show a slight decrease in the overall concentration of Gd-albumin.

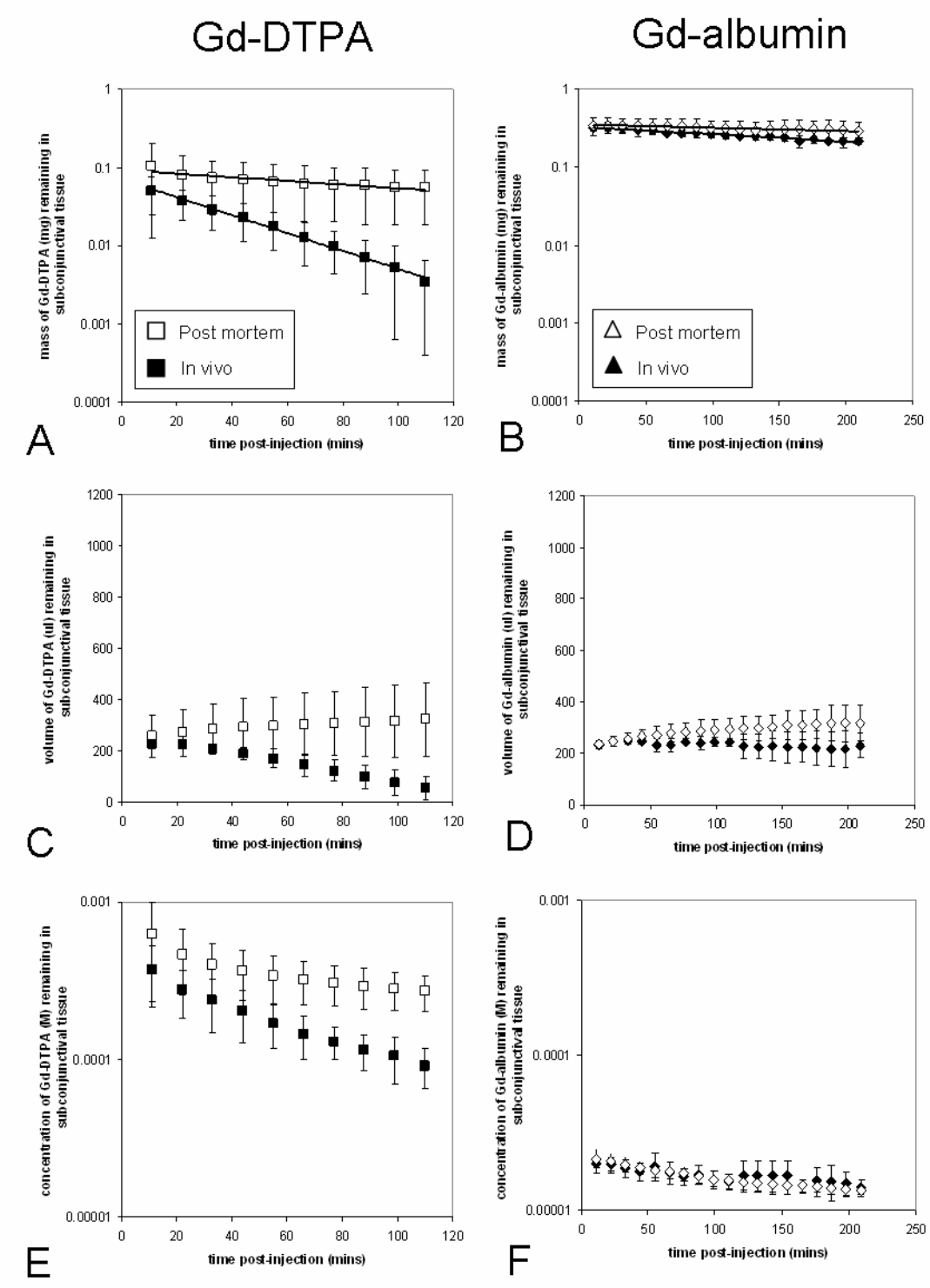

Figure 4-7. Plots comparing Gd-DTPA and Gd-albumin.

Gd-DTPA (A, C, E) and Gd-albumin (B, D, F) change in mass, apparent volume and concentration after 200 µl subconjunctival injection *in vivo* and *post mortem*. Values

are given as mean ± SD. Lines indicate regression for mass clearance data. r^2 values: ■=0.99, □=0.84, ◆=0.94, ◇=0.97.

Figure 4-8 shows a histological slide of the sectioned cryo-treated area after hemotoxylin and eosin staining. The eye was enucleated 4 weeks after cryotherapy and sectioned into 10 micron slices. The retina is shown to be effectively obliterated in the cryo area. Table 4-1 shows that the k value from cryo-treated animals is 0.0336 min^{-1}. From the Mann-Whitney U test, this is significantly different from the *in vivo* k value, 0.0273 min^{-1} (Table 4-2). Therefore, cryotherapy significantly increases the mass clearance rate of Gd-DTPA after subconjunctival injection.

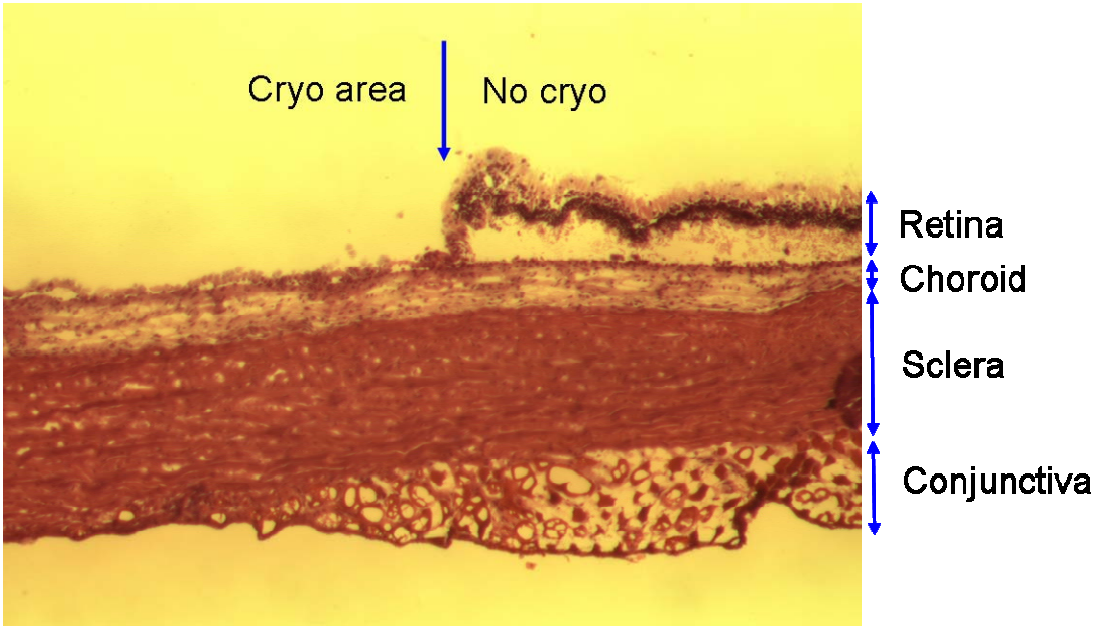

Figure 4-8. Sectioned cryo area after H&E staining.

4.4. Discussion

Our study gives a quantitative comparison of the clearance of Gd-DTPA and Gd-albumin following subconjunctival injection in rabbits. The clearance rates of Gd-DTPA and Gd-albumin were determined by measuring the changes in signal intensity by means of DCE-MRI and converting these values into mass.

4.4.1. Gd-DTPA vs. Gd-albumin

Results from *in vivo* experiments show that the mass decrease of Gd-DTPA is faster compared to that *post mortem*. This indicates that there are dynamic clearance mechanisms that are present *in vivo* but not *post mortem*. *In vivo*, drugs can be cleared from the subconjunctival depot by diffusion into surrounding tissues and also by entering lymphatic and blood vessels located in the conjunctiva [52,105]. *Post mortem*, drug elimination from the depot occurs mainly by diffusion since blood and lymphatic flow are presumed absent. While the clearance rate of Gd-DTPA *in vivo* was substantially higher than that *post mortem*, the *in vivo* and *post mortem* clearance rates of Gd-albumin did not differ significantly. This indicates that *in vivo* clearance mechanisms such as blood and lymph flow have a considerable effect on the elimination of Gd-DTPA but not on Gd-albumin.

Gd-DTPA molecules are smaller (<1 nm) and lower in molecular weight than Gd-albumin (4 nm). Drug absorption after subcutaneous injection has been shown to

decrease linearly with increasing molecular weight [173], and a similar dependence may exist after subconjunctival injection. The disposition of nanoparticles following subconjunctival injection has been shown to display a size-dependence, with smaller particles reaching undetectable levels in the periocular tissue while larger particles were almost entirely retained [53]. Small drug molecules (<1 kDa) are thought to be preferentially absorbed by the blood capillaries while proteins larger than about 16 kDa are taken up primarily by the lymphatic system [173,174]. The large molecular radius of Gd-albumin may hinder its entry into blood vessels so that clearance by blood flow is negligible. However, lymphatic vessels permit the entry of large particles and Gd-albumin may be cleared by the lymphatics present in the conjunctiva. Since albumin molecules are able to gain rapid access to lymphatic vessels but not to blood vessels, they are used in lymphatic flow studies which require administration by subcutaneous injection (Schornack, PA et al. *Proc Intl Soc Mag Reson Med*, ISMRM, 2001;58) [175,176]. Gd-DTPA, on the other hand, should be easily cleared by both blood and lymphatics because of its small size. Our results show that the *in vivo* Gd-albumin clearance rate from the subconjunctival space was significantly slower than Gd-DTPA clearance rate by a factor of about 14, as seen from the values in Table 3-1. These results may be indicative of the selective clearance of Gd-albumin through lymphatic vessels and the relatively low flow rate of lymph compared to that of blood [174]. Our results also show that the clearance rates of Gd-albumin *in vivo* and *post mortem* are not significantly different. If Gd-albumin is cleared mostly by lymph and not by blood flow, this may suggest that lymphatic clearance after subconjunctival injection is not significant.

Maurice and Ota previously reported on the kinetics of subconjunctival injections in 1978 [170]. They reported that the half-life of ^{22}Na was 9 minutes while that of albumin was 9 hours. Our data shows that the half-life of Gd-DTPA after a 200 µl injection *in vivo* is about 27 minutes, which based on its molecular size, fits reasonably with Maurice and Ota's findings. The half-life of Gd-albumin reported in our study (5.3 hours) also compares to the half life of 9 hours reported by Maurice and Ota. The discrepancy may be explained by the difference in data acquisition, as Maurice and Ota measured radioactive-labeled albumin from sections of excised tissue from enucleated eyes. For comparison to other tissues, Pain et al [177] reported a 3.6 hour half life for the clearance of albumin from subcutaneous injections in healthy human volunteers. Their clearance data showed a single exponential decay over times up to three hours.

4.4.2. Quantitation of MRI Results

With the cessation of blood or lymph flow in the *post mortem* animal, a nearly zero clearance rate for both Gd-DTPA and Gd-albumin is expected. In our study, the *post mortem* decrease in mass is most likely due to the diffusion of contrast agent molecules out of the subconjunctival space. As molecules diffuse away from the subconjunctival depot, they will begin to fill the pixels that lie on the periphery of the injection site. But many of these pixels will have very low concentrations of contrast agent and will remain below the threshold value (0.01 mM for Gd-DTPA and 0.005 mM for Gd-albumin). Although these pixels contain contrast agent molecules, they are removed during image analysis. Therefore, the total mass of contrast agent

decreases over time because molecules are continuously moving from high to low concentration areas, increasing the number of molecules residing in pixels that fall below the threshold. Since the diffusion of Gd-DTPA is faster than Gd-albumin, the *post mortem* "clearance" of Gd-DTPA is also faster than that of Gd-albumin.

On the other hand, the apparent volume was reported to increase in *post mortem* experiments. As molecules diffuse out of the depot, more molecules will enter the pixels surrounding the injection site. This will increase the concentration of contrast agent and in some cases the increase may be sufficient for pixels to have values above the threshold. These pixels are then counted as part of the subconjunctival depot during image analysis, and the volume will increase with time.

The volume measured in our studies represents the apparent volume of contrast agent in the eye, not the volume of the subconjunctival bleb. The changes in volume and mass of subconjunctival fluid may be different from that of the contrast agent. While fluid clearance may affect solute clearance, the technique used in our study cannot distinguish between fluid and solute clearance, and other measurement methods are necessary to explore these mechanisms in detail.

4.4.3. Effect of Injection Volume

Our results also showed that there was no significant difference in clearance rate when comparing the 60 and 200 μl injections and the 200 and 600 μl injection volumes. The clearance rate is significantly different, however, when comparing the 60 and 600 μl injection volumes. Previous studies using intramuscular injections reported a higher rate of absorption of hydrophilic drugs when the compounds were

administered in smaller injection volumes [178,179]. This is expected as a high interface area to injection volume ratio increases the drug absorption rate [180,181] and is in line with our results. In our study, the Mann-Whitney U test results demonstrated that the clearance rate did not differ significantly until the volumes differed by an order of magnitude. This indicates that the surface area to volume ratio will significantly alter the mass clearance rate when injection volumes differ by 10-fold.

The MRI results also show that larger injection volumes allow for longer retention times of contrast agent in the subconjunctival space. A comparison of mass values after 200 and 600 μl injections shows that there are higher amounts of Gd-DTPA in the subconjunctival space after the 600 μl injection at any given time point. This may be of clinical importance when longer retention times of drugs are required in the subconjunctival space to produce prolonged release of drug.

4.4.4. Effect of Cryotherapy

The results from the cryo-treated rabbits showed significantly faster clearance than normal rabbits. This is a surprising result, since with the elimination of choroidal blood flow, the rate of mass clearance is expected to be reduced. Gd-DTPA may have permeated to the vitreous at higher levels since cryotherapy may have significantly reduced the diffusional resistance provided by the retina (and probably also the RPE). However, the accumulation of Gd-DTPA in the vitreous did not significantly increase, since Gd-DTPA concentrations were found to be below detection levels (< 0.03 mM) during the entire scanning period. Therefore, this is a

puzzling result, since elimination has somehow increased after cryotherapy, despite the decrease in diffusional resistance. This result prompts further investigation on the physiological changes that occur after cryotherapy and whether there are any alterations in blood flow or permeability to ocular tissues before cryotherapy becomes an established model for selective elimination of choroidal clearance.

4.4.5. Limitations in DCE-MRI Technique

There are several limitations of the DCE-MRI technique used in our study. The concentration range of contrast agent detected by our DCE-MRI method is only about 2 log units. The effect of dose on clearance rate could not be studied due to the narrow concentration detection range. Concentration changes occurring beyond this range are undetectable with our technique and more sensitive methods such as measurement of T_1 may be required. The differences in relaxation times of PBS and subconjunctival tissue may contribute to error in the conversion of signal intensity to concentration, because our calibration was based on PBS and not on subconjunctival tissue. However, since the subconjunctival bleb is comprised mostly of fluid and not tissue, we assumed that PBS would adequately model the subconjunctival bleb. Also, our choice of Gd-DTPA as a low molecular weight model drug may not be fully adequate since Gd-DTPA is a hydrophilic molecule and may exhibit pharmacokinetic behavior that is different from lipophilic drugs. In following animal care and use guidelines, inhalational isoflurane was required to maintain general anesthesia. Clearance rates may be different in an anesthetized vs. a non-anesthetized animal, as

the effect of inhalational isoflurane on blood and lymphatic flow in the eye is unknown.

In this study, a volume coil was utilized and therefore high resolutions produced in prior studies (Chapter 3) using a surface coil could not be achieved. However, a volume coil allows a bigger FOV to capture standard phantoms and the contralateral eye. For this study, since high spatial resolution was not as critical as temporal resolution, a volume coil could be used to acquire the necessary data for this analysis.

4.5. Conclusion

DCE-MRI is a useful technique that allows non-invasive *in vivo* data measurement in real-time. Our study demonstrates that sufficient spatial and temporal resolution can be achieved with DCE-MRI to capture the kinetic changes of subconjunctival drug clearance. DCE-MRI also enables the quantitation of data through the conversion of signal intensity to concentration. Results from subconjunctival injections of Gd-DTPA and Gd-albumin indicate that active clearance mechanisms (such as lymphatic and blood flow) can affect drug elimination rates. Lymphatic clearance does not seem to be as significant as clearance by blood, as evidenced by data from Gd-albumin injections. Injection volume significantly decreases the clearance rate when increased 10-fold, and higher injection volumes allow for longer retention times of drug.

Chapter 5: A Model of Subconjunctival Drug Delivery

5.1. Introduction

Although many ocular pharmacodynamic studies have been reported in the literature, the pharmacokinetics in the eye after drug delivery needs more elucidation. The number of ocular pharmacodynamic studies is far greater than pharmacokinetic studies, and this is particularly true for periocular (i.e. transscleral) drug delivery studies [182]. As a result of the lack of periocular pharmacokinetic data, modeling efforts have been hindered as many pharmacokinetic parameters remain unknown.

In an effort to better explore the drug barriers and clearance mechanisms present in the eye, a finite element model of transscleral drug delivery by subconjunctival injection was created using COMSOL and the results were compared to MRI data. Finite element modeling enables distributed pharmacokinetic modeling, which incorporates both temporal and spatial information of drug distribution [183]. On the contrary, compartmental models assume that the drug is distributed homogeneously in each tissue or organ. In modeling local ocular drug delivery, compartmental models may not accurately represent the distribution of drugs in eye tissues since steep drug concentration gradients are often established due to the complexity of drug transport barriers present in the eye. Therefore, distributed models may be of greater interest and may provide more accurate information regarding local ocular drug delivery.

As previously discussed, drug measurements in eye tissues are traditionally reported as a total mass or average concentration value. Because tissues are

processed and analyzed in their entirety, information regarding the spatial distribution of drugs is lost. Therefore, many current pharmacokinetic models of drug delivery in the eye are compartmental models [133,184], reflecting the manner in which drug measurements have been acquired in ocular delivery studies.

In this research, *in vivo* temporal and spatial drug distribution information was acquired by utilizing MRI. The results from MRI experiments were used to compare the results from a finite element model defined using literature values. To date, the most investigative modeling on subconjunctival delivery has been performed by Lee and Robinson [185-187], in which the subconjunctival space and the vitreous chamber are modeled as compartments (Fig. 5-1). Figure 5-2 shows a proposed (unsolved) subconjunctival compartmental model accounting for the intermediary tissues [133]. A more recent study performed by Mac Gabhann et al [188] describes a one-dimensional distributed model of protein delivery to the retina after subconjunctival injection (Fig. 5-3). Currently, this is the only model in the literature that explicitly accounts for the distinct transport properties of each of the ocular wall tissues (sclera, choroid and retina). Finite element modeling has previously been used to model drug distribution within the vitreous compartment [57,58,189,190] after intravitreal delivery. However, a finite element model has not yet been reported for transscleral (including subconjunctival) drug delivery.

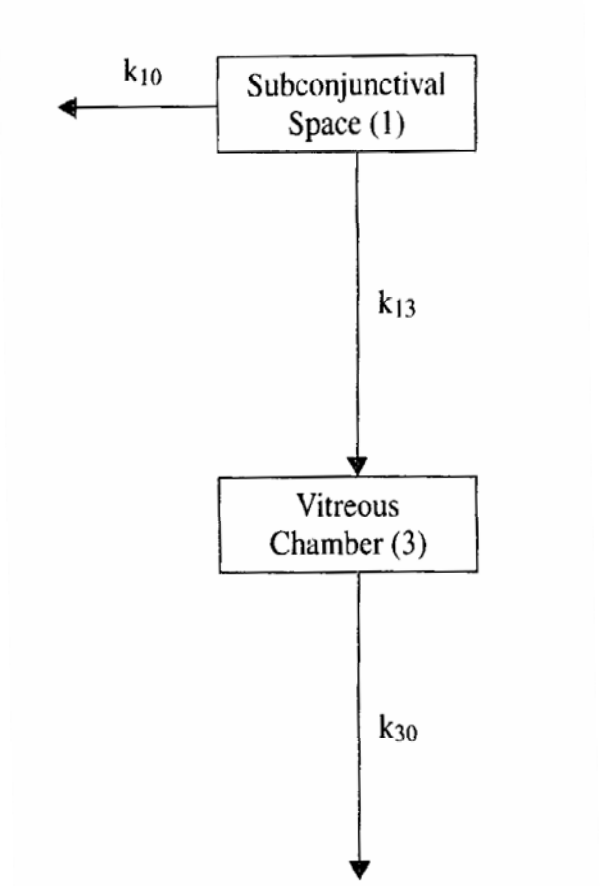

Figure 5-1. A simple compartmental pharmacokinetic model of subconjunctival injection.

From Lee, 2004 [186].

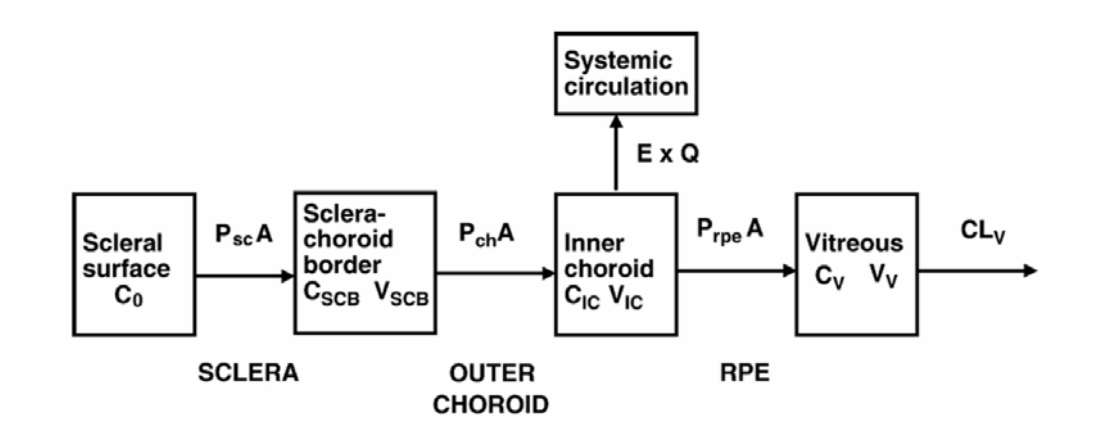

Figure 5-2. A proposed compartmental pharmacokinetic model of subconjunctival injection.

From Ranta, 2006 [133].

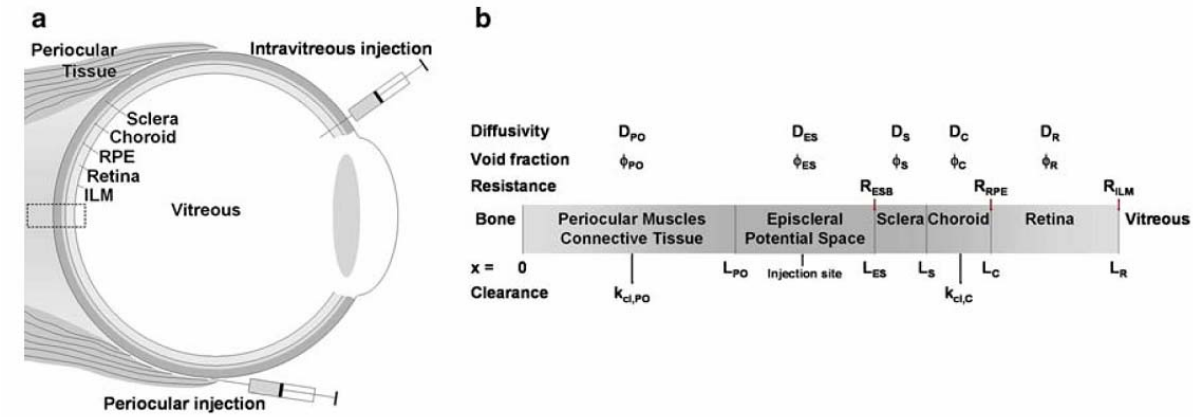

Figure 5-3. A distributed pharmacokinetic model of subconjunctival injection.

From Mac Gabhann, 2007 [188].

5.2. Methods

5.2.1. Model Geometry

A two-dimensional axisymmetric geometry was created in COMSOL Multiphysics™ 3.3a (Burlington, MA) using the Chemical Engineering Module to resemble the anatomy of the tissues involved during subconjunctival delivery. The model was designed to simulate a 200 µl bolus subconjunctival injection of Gd-DTPA. Figure 5-4 shows the model geometry which includes 7 subdomains: adipose tissue, conjunctiva, the injected drug bolus, sclera, choroid, retina, and vitreous. The RPE was not drawn as a separate subdomain but was modeled as a thin resistance layer with a thickness of 10 microns [191].

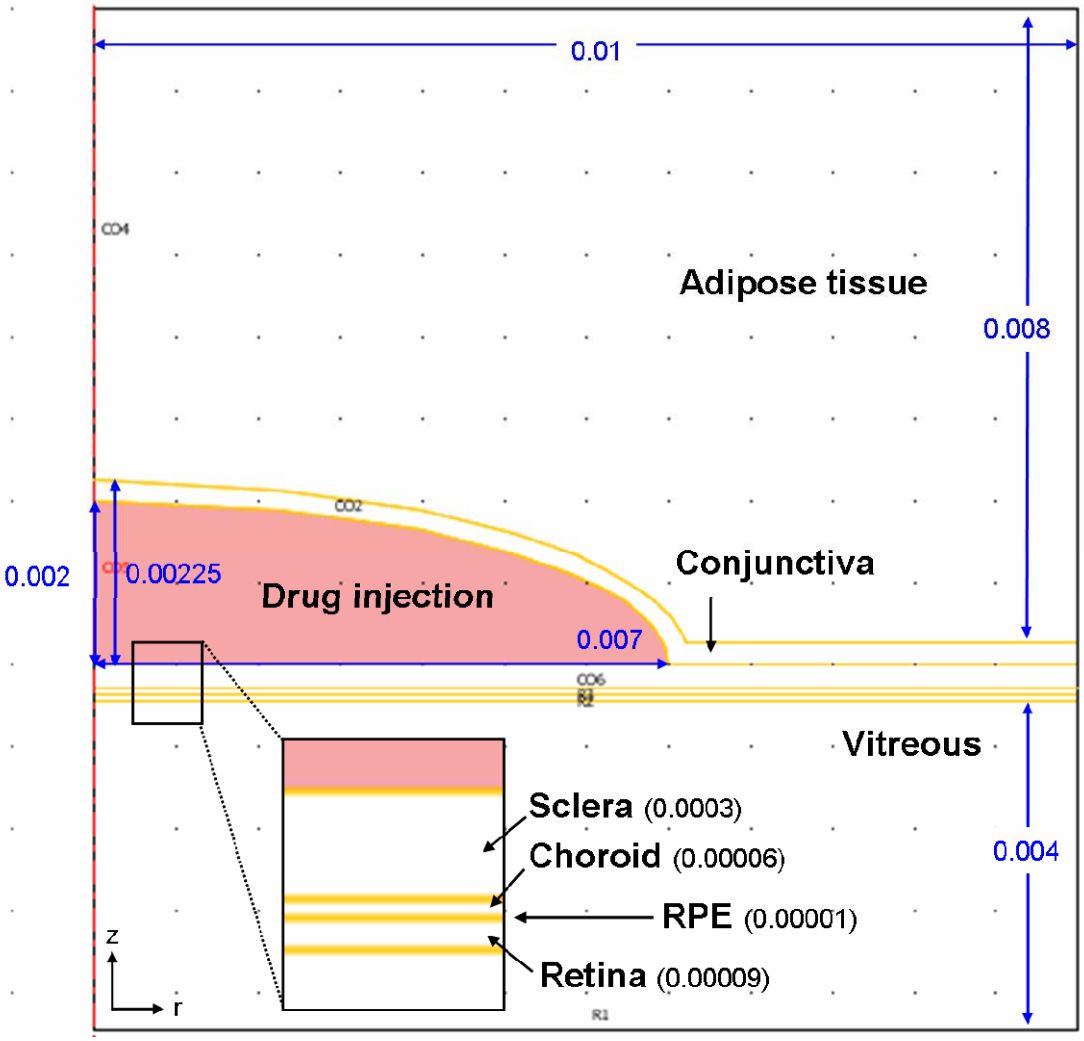

Figure 5-4. Model geometry in r-z plane.

Numbers indicate dimensions in meters.

The bolus was drawn as an ellipsoid with a radius of 0.007 m and height of 0.002 m to yield a volume of 205.25 µl, simulating a 200 µl injection. The radius and height of the injection solution domain were specified to match the radius and height of the bolus imaged from MRI experiments. The conjunctiva was drawn as an elliptical shell enveloping the outer side of the bolus and the remaining compartments

were drawn as cylindrical discs. The thicknesses of the choroid and retina were determined by measuring the tissue thicknesses of the albino rabbit choroid and retina from histology slides (Table 5-1). Adipose tissue was included as a subdomain outside the conjunctiva, since it surrounds the orbit, acting as a cushion for the eyeball [192]. The model was reduced to a quarter of the original geometry to minimize solver time and memory requirements.

Tissue	Thickness (m)	Reference
Sclera	0.0003	Fatt, 1970 [193]
Choroid	0.00006	Measured in histology slides
Retina	0.00009	Measured in histology slides

Table 5-1. Tissue thickness values used in model.

The geometry was meshed using triangular elements resulting in 33120 elements and 69223 degrees of freedom (Figure 5-5). The model was solved for times from 0 to 3 hours at 11 minute increments to correspond to the MR image acquisition time. Model solver times were approximately 90 seconds.

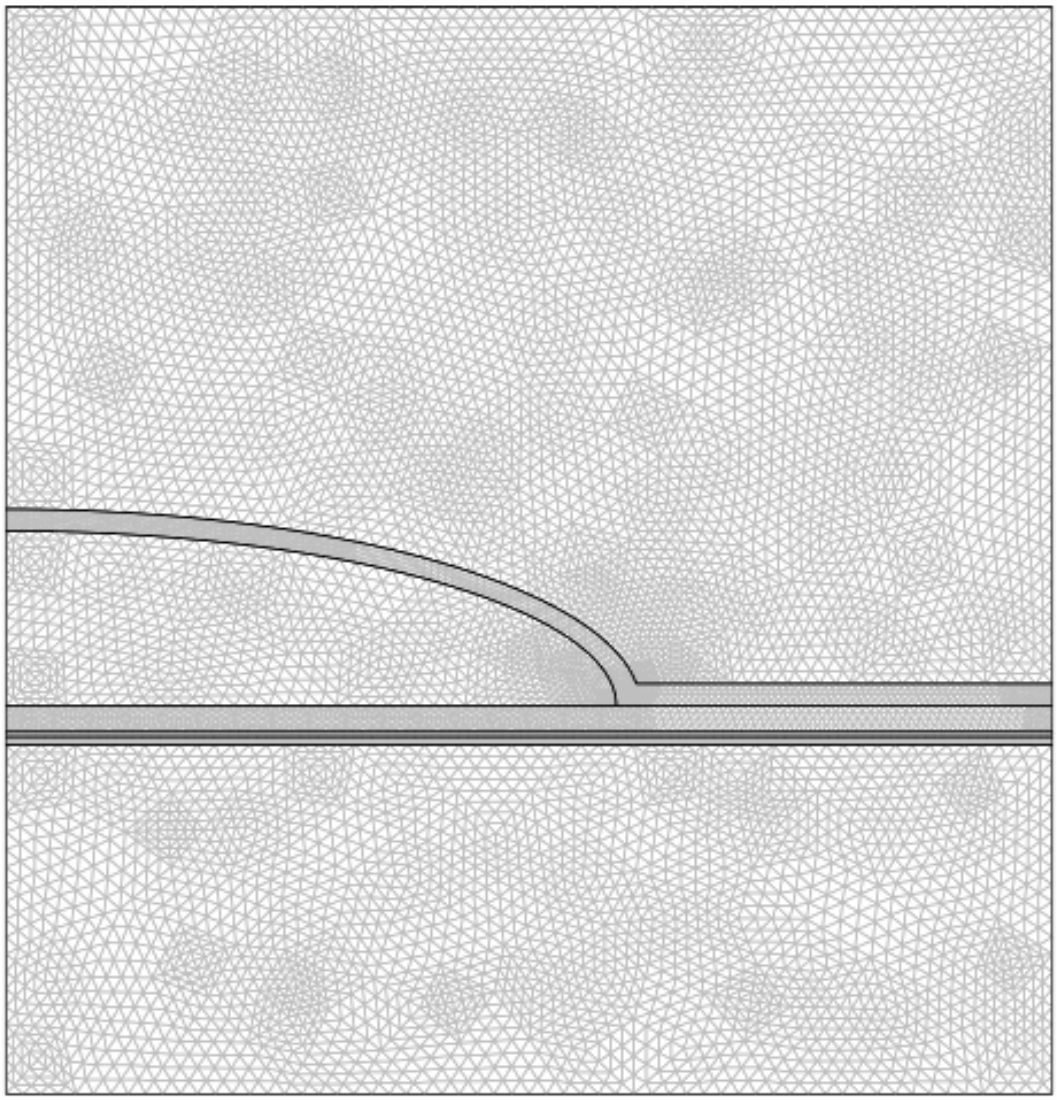

Figure 5-5. Meshed geometry in r-z plane.

5.2.2. Model Parameters

5.2.2.1. Governing equation

A transient diffusion analysis was specified for the model geometry, and transport by convection was ignored. Therefore, the governing mass transport equation is described by:

$$\frac{\partial C}{\partial t} + \nabla \cdot (-D \nabla C) = R \tag{1}$$

where C is the whole tissue concentration of Gd-DTPA, D is the whole tissue diffusion coefficient, and R is the reaction rate. For tissues with significant cellular mass, extracellular parameters were taken into account:

$$\begin{aligned} C &= C_e \phi_e \\ D &= D_e \phi_e \end{aligned} \tag{2}$$

where φ is the extracellular void volume fraction. Void fractions for various tissues are given in Table 5-2. The void volume fraction has not been reported for the conjunctiva, and it was estimated that the void fraction would be the same as that of the choroid since the conjunctiva is cellular and includes vascularity.

Tissue	**Void fraction (φ_e)**	**Reference**
Adipose	0.1	Linde and Chisolm, 1975 [194]
Conjunctiva	0.4	estimate
Sclera	0.8	Mac Gabhann, 2007 [188]
Choroid	0.4	Mac Gabhann, 2007 [188]
Retina	0.3	Mac Gabhann, 2007 [188]

Table 5-2. Model values of extracellular void volume fraction.

5.2.2.2. Diffusion coefficients

Diffusion coefficients were assigned to each subdomain. The injection bolus was assigned the diffusion coefficient of Gd-DTPA in water (Table 5-3), since the injection solution consisted of Gd-DTPA in PBS. The diffusion coefficient of Gd-DTPA in the vitreous was also assumed to be equal to that in water. The calculation of the diffusion coefficient of Gd-DTPA in various subdomains is described in the Appendix. The diffusion coefficient of the RPE was determined by using the permeability value of sodium fluorescein (NaF) across the Bruch's membrane-choroid and RPE [195]. NaF has similar physicochemical properties as Gd-DTPA in molecular weight (376 Da) and hydrophilicity.

Subdomain	**Diffusion coefficient (m^2/s)**
Injection solution	5.3e-10
Conjunctiva	2.2e-10
Adipose tissue	2.0e-10
Sclera	2.6e-10
Choroid	2.2e-10
RPE	4.9e-13
Retina	2.1e-10
Vitreous	5.3e-10

Table 5-3. Model parameters: diffusion coefficients.

5.2.2.3. Clearance rates

MRI data from Chapter 3 suggested that lymphatic flow may not be a significant contributor to drug clearance in the eye. In addition, while adipose tissue is vascularized [196], the presence of lymphatics is still debated [197]. Therefore, blood flow was regarded as the sole contributor to *in vivo* clearance in this modeling study. Clearance by blood flow was simulated by including a reaction (clearance) rate term (R) in the conjunctiva, choroid, and adipose tissue. The clearance rate was assumed to be first-order:

$$R = CL \times C \tag{3}$$

(where CL is a constant) since in most instances, the first-order approach is regarded as a reasonable approximation for many drug absorption processes in the body [198].

The clearance constant CL was defined using the equation for capillary clearance developed by Kety, Renkin and Crone [199-201]:

$$CL = \frac{Q}{V}\left[1 - e^{\frac{-PS}{Q}}\right] \tag{4}$$

where P is the capillary permeability, S is the capillary surface area, Q is the tissue blood flow rate, and V is the volume of distribution. Values for PS and Q were gleaned from the literature and are summarized in Tables 5-4 and 5-5.

The capillary surface area of the choriocapillaris was estimated by multiplying the surface area of the choroid (8 cm^2; [134]) by 3/2, similar to the method used by Bill et al [202]. The conjunctival capillaries are nonfenestrated, similar to those found in skeletal muscle [203]. Since values of PS and Q for the conjunctiva have not been reported, values for skeletal muscle were used instead. Values for ^{51}Cr-EDTA were used since ^{51}Cr-EDTA is commonly used in perfusion studies and its physicochemical properties are similar to that of Gd-DTPA (^{51}Cr-EDTA is also lipid-insoluble and has a molecular weight of 357 Da).

Tissue	**Species**	**P (cm/s)**	**S (cm^2)**	**PS (g/s)**
Choroid (choriocapillaris)	Rabbit	7e-4* [204]	12	0.0084
Skeletal muscle	Cat	---------	--------	0.0002* [205]

Table 5-4. Literature values and calculated values of PS.

*Reported value for ^{51}Cr-EDTA.

Tissue	**Species**	**Q (g/s)**
Choroid	Rabbit	0.0135 [158]
Skeletal muscle	Human	0.0001* [206]

Table 5-5. Literature values of Q.

*value scaled for rabbit conjunctiva.

The volume of choroidal tissue was calculated by multiplying the tissue thickness (0.006 cm) by the surface area (8 cm^2) and regarding tissue density as that of water (1 g/cm^3). Likewise, the volume of conjunctival tissue was calculated using an estimated tissue thickness (0.03 cm) multiplied by the surface area (8 cm^2; [207]). This yielded values of 0.048 g and 0.24 g for volumes of the choroid and conjunctiva, respectively.

Table 5-6 shows the CL values calculated from equation (4) for the conjunctiva and choroid.

Subdomain	**CL (s^{-1})**
Adipose tissue	-0.0003* [208]
Conjunctiva	-0.00041
Choroid	-0.13

Table 5-6. Calculated clearance rate constants for *in vivo* models.

*Reported value for ^{51}Cr-EDTA in rabbit.

From equation (4), if PS<<Q,

$$CL \approx \frac{PS}{V} \tag{5}$$

the clearance rate becomes diffusion limited. Similarly, if PS>> Q,

$$CL \approx \frac{Q}{V} \tag{6}$$

and the clearance rate becomes blood flow limited. The clearance constant for adipose tissue was assumed to be diffusion-limited since the vessels are nonfenestrated and a perfusion rate could not be found from the literature. In addition, the diffusion-limited CL value is not expected to differ significantly from the perfusion-limited value (as is the case for the conjunctiva, indicated from the values listed in Tables 5-4 and 5-5).

For models simulating *post mortem* delivery (no blood flow), CL was set equal to 0.

5.2.2.3. Boundary and Initial conditions

All outside boundaries were set to insulation (zero flux), and the interior boundaries were assigned as continuity except at the RPE boundary, which was specified as a thin boundary layer (Figure 5-6). The initial conditions were specified as1 mM for the injection bolus and 0 mM for all remaining subdomains.

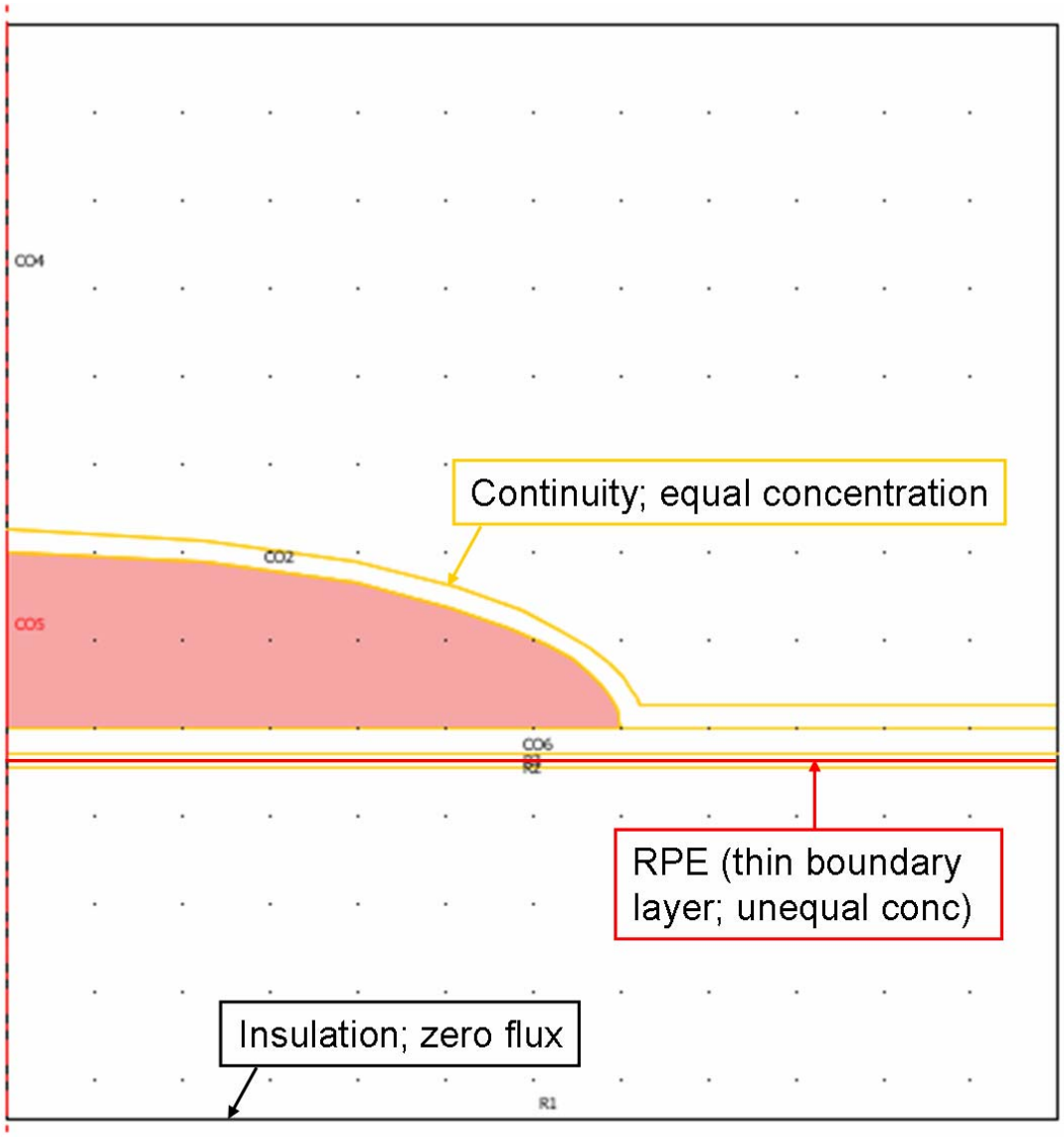

Figure 5-6. Boundary conditions.

5.3. Results

5.3.1. Post mortem

Figure 5-7 shows the results from the *post mortem* model simulation at time=0 minutes post-injection. A thresholding of 0.03 mM was applied to the images to

match the detection limit of the MR images. The injection depot subdomain is at the initial concentration of 1 mM and the remaining subdomains are at 0 mM. Figure 5-8 shows the change in concentration with time and space. At 11 minutes post-injection, a significant amount of Gd-DTPA has diffused into the surrounding subdomains. By 55 minutes, a low concentration of Gd-DTPA can be detected in the conjunctiva and portions of the adipose tissue as the contrast agent molecules are diffusing out of the bleb. By 3 hours, low levels of Gd-DTPA can be seen in most of the surrounding tissues including the vitreous.

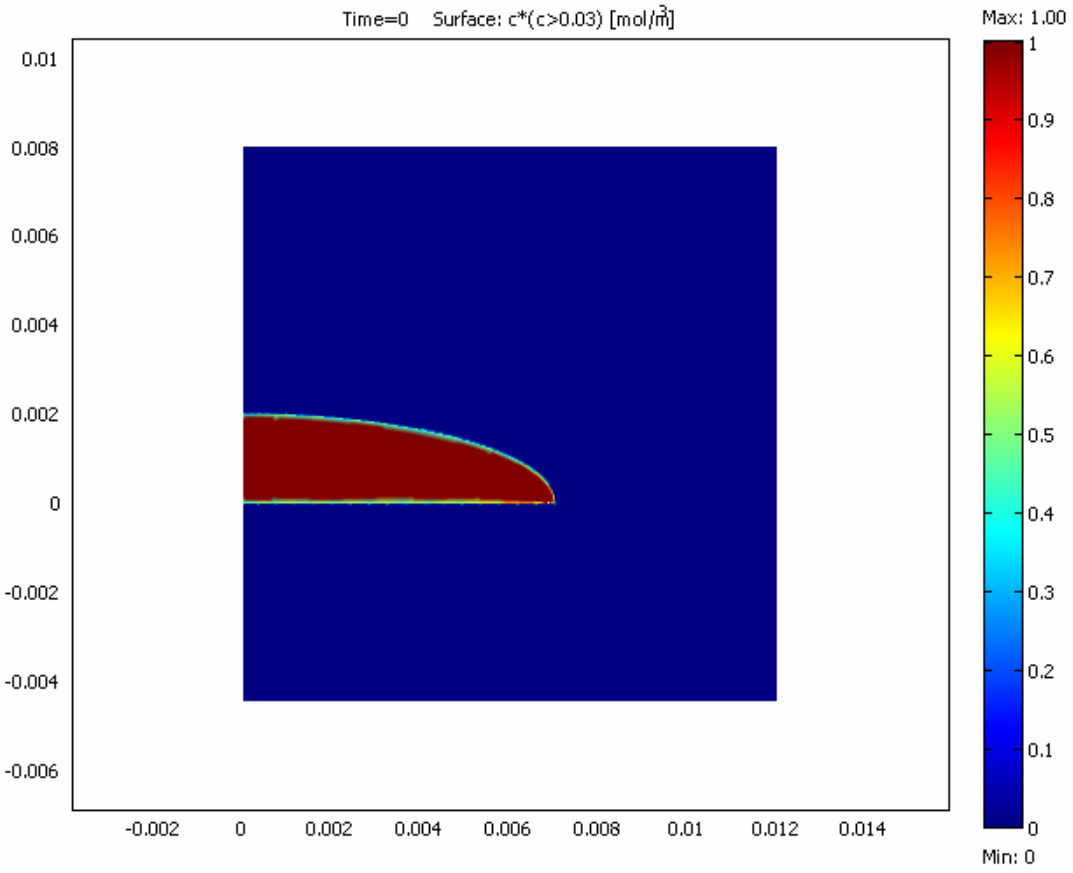

Figure 5-7. Model result at t=0 min post-injection (initial condition).

Color scale shows the concentration range in mM units.

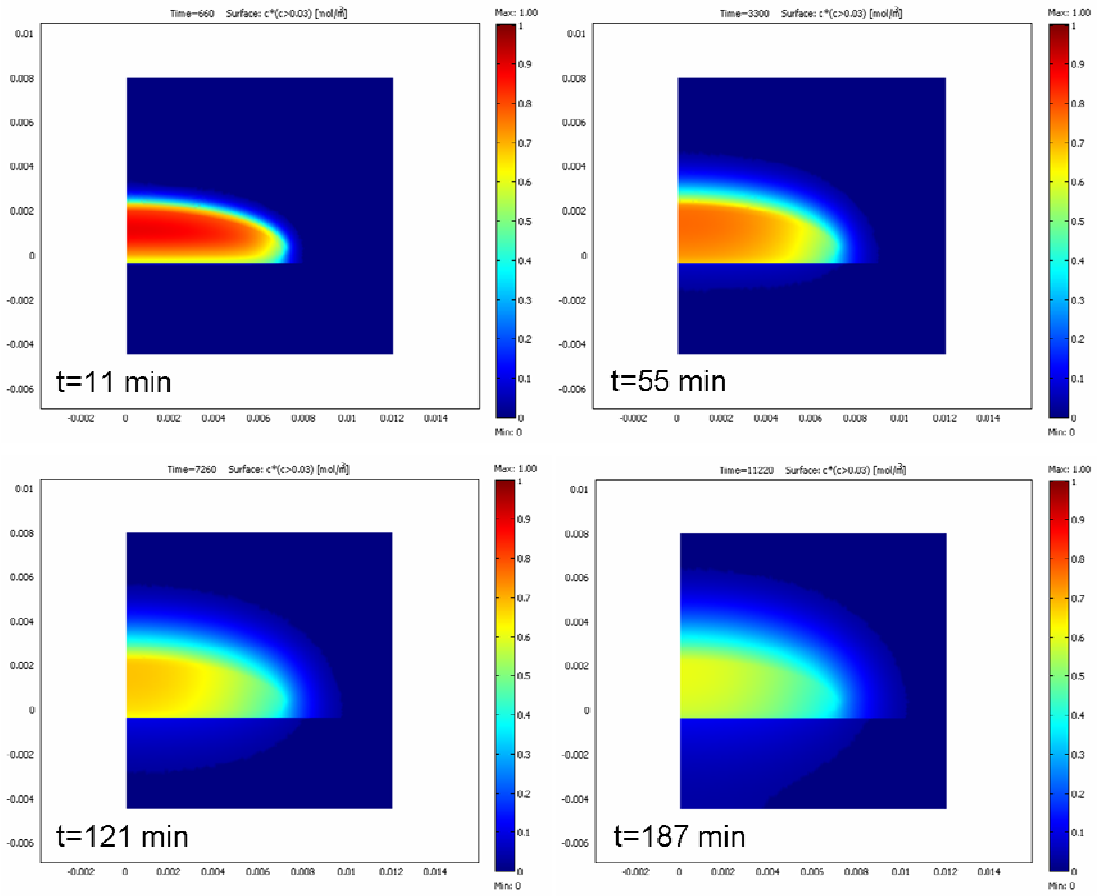

Figure 5-8. Concentration changes of Gd-DTPA with time and space in the *post mortem* model.

Color scale shows the concentration range in mM units. Times represent minutes after injection.

Figure 5-9 shows the concentration profiles from the center axis of symmetry, r=0. High concentrations remain within the injection depot but steep gradients are observed on either side of the subconjunctival subdomain. The RPE provides high diffusional resistance between the choroid and retina (Fig. 5-10), resulting in very low concentrations in the retina and vitreous.

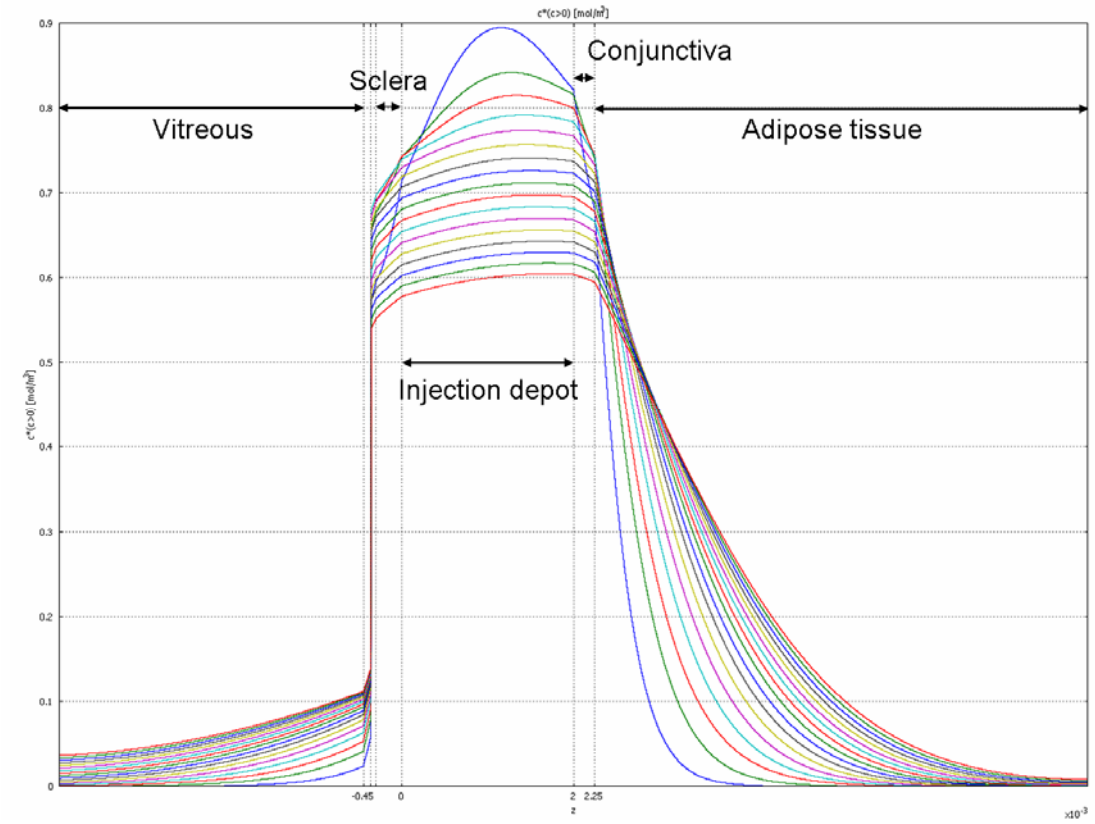

Figure 5-9. Concentration profiles from the *post mortem* model of Gd-DTPA through the center axis of symmetry, r=0.

Lines represent concentration profiles at 11 minute increments from 11-187 minutes post-injection.

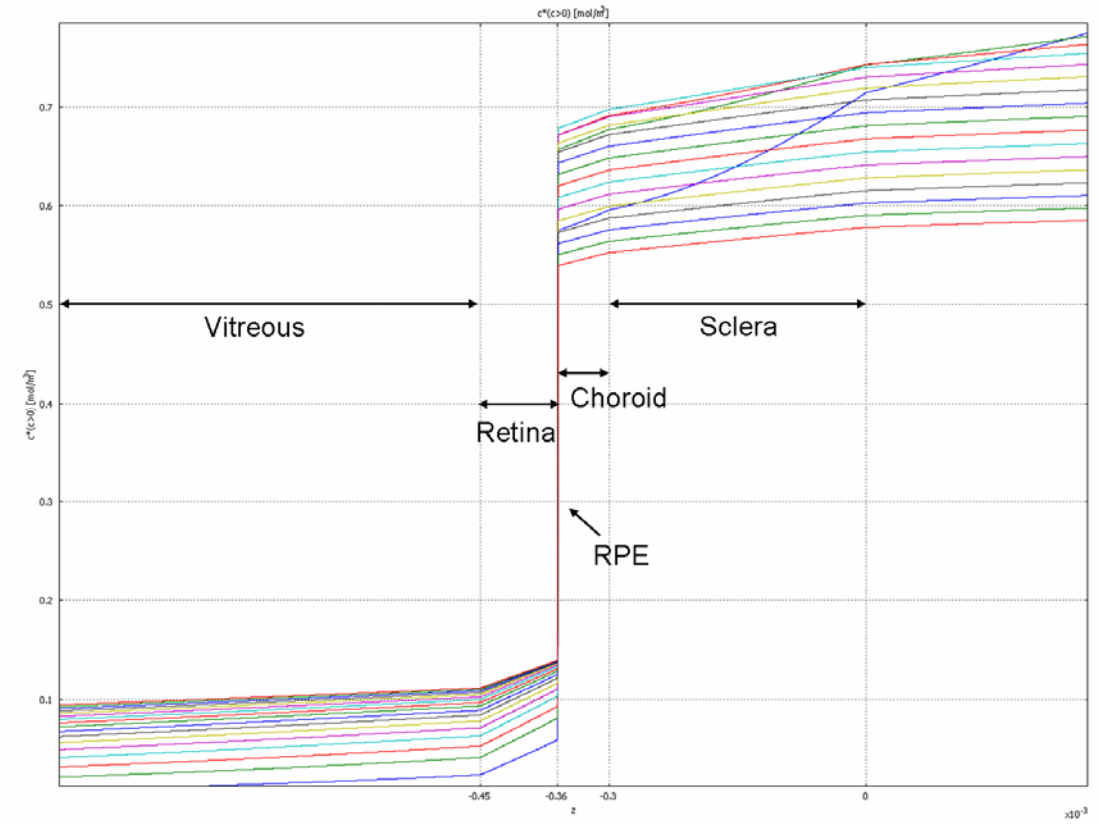

Figure 5-10. Increased magnification of concentration profiles shown in Figure 5-9.

Figure 5-11 shows a plot of the mass decrease of Gd-DTPA comparing the model results to the MRI data. To obtain mass values of Gd-DTPA from the model, mass integration was performed on all subdomains at each time point for those elements that had concentration values above the specified threshold of 0.03 mM. The resulting k value for the *post mortem* model is 0.0008 min^{-1}. This is significantly different from the MRI experimental result (k = 0.0041 min^{-1}).

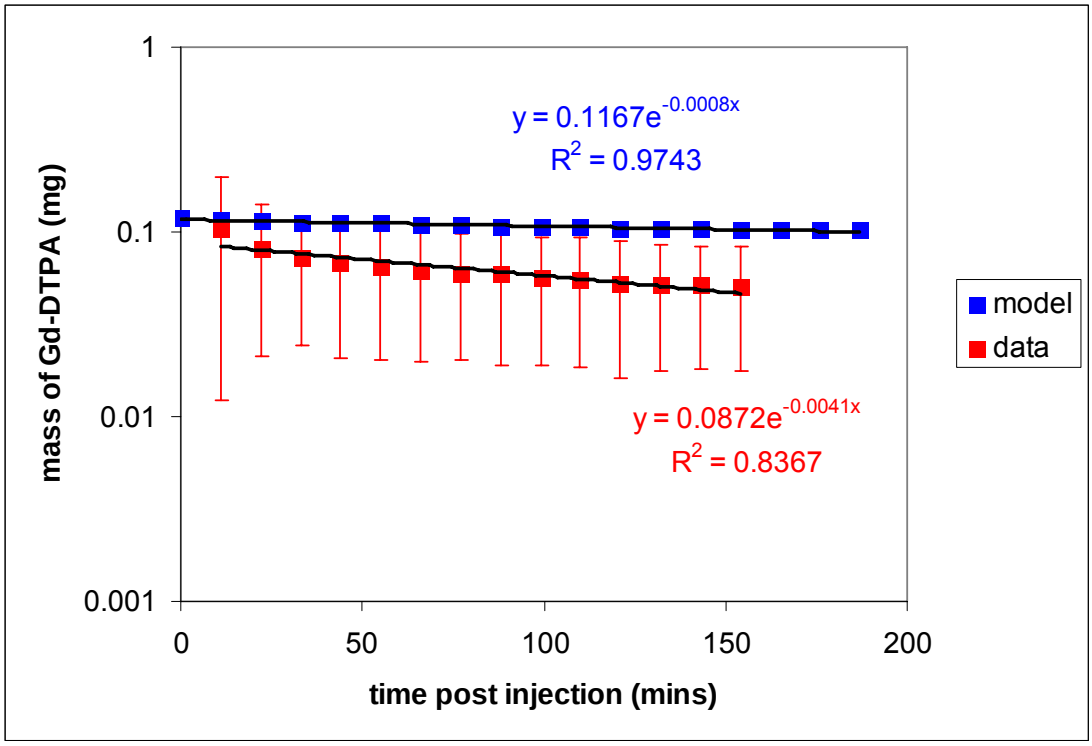

Figure 5-11. A comparison of the mass clearance of Gd-DTPA from the *post mortem* model and the MRI data.

Equations used in exponential regression also shown as $y=Ae^{-kx}$, where k is the mass clearance rate in min^{-1}.

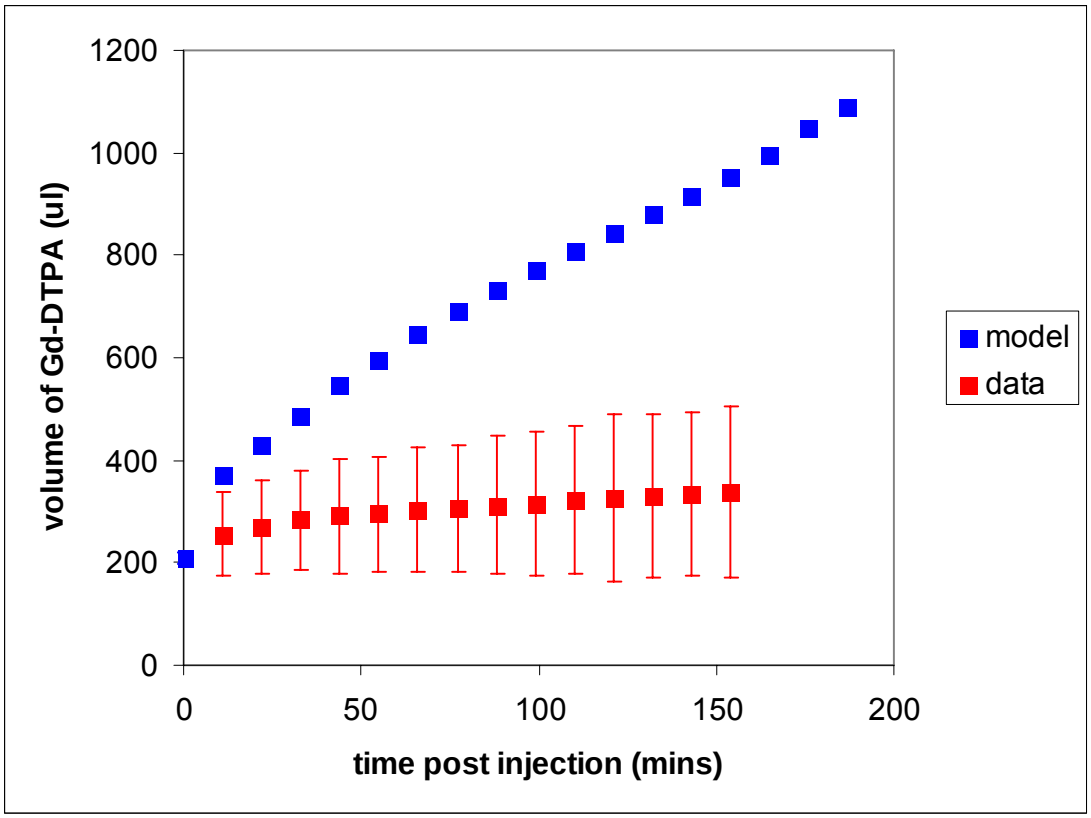

Figure 5-12. A comparison of the distribution volume of Gd-DTPA from the *post mortem* model and the MRI data.

Figure 5-12 shows the change in apparent distribution volume from the model and data results. The volume was determined in a similar manner to the mass calculation, by integrating over all subdomains at each time point only for those elements that had concentration values above the threshold. The volume increases significantly from the *post mortem* model results compared to the experimental MRI data.

5.3.2. In vivo

Figure 5-13 shows the change in concentration with time and space from the *in vivo* model simulation. Gd-DTPA concentration in the bolus rapidly decreases with time, similar to the trend seen from the *in vivo* MRI experiments. Low concentrations of Gd-DTPA can be seen penetrating into the adipose tissue, increasing the apparent volume occupied by Gd-DTPA. However, the rapid clearance of the choroid effectively prevents the visible accumulation of Gd-DTPA in the vitreous.

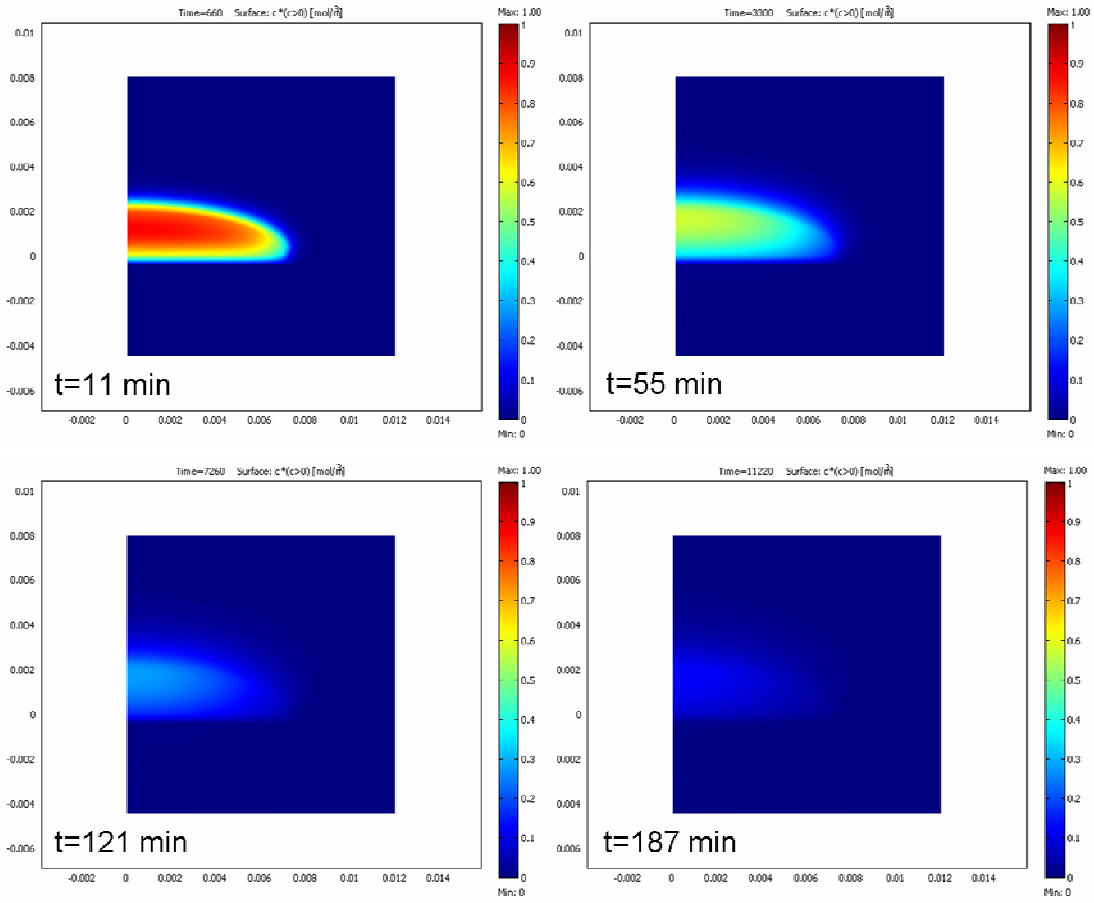

Figure 5-13. Concentration changes of Gd-DTPA with time and space in the *in vivo* model.

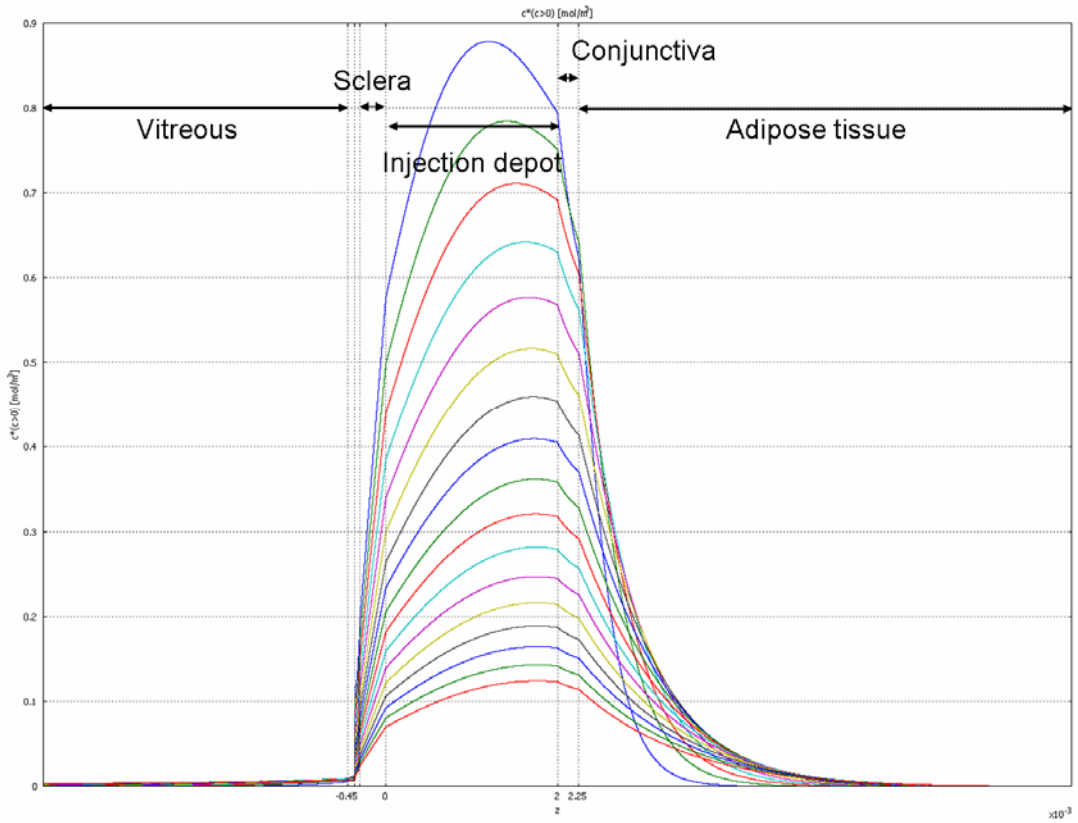

Figure 5-14. Concentration profile results from the *in vivo* model of Gd-DTPA through the center axis of symmetry, r=0.

The effect of choroidal clearance on preventing significant Gd-DTPA penetration to the retina and vitreous is more clearly seen from the concentration profiles in Figures 5-14 and 5-15. A steep concentration gradient is established in the sclera due to the rapid choroidal clearance. The RPE provides a high diffusional

barrier that dramatically reduces the concentration of Gd-DTPA in the retina and vitreous (Figure 5-15).

.

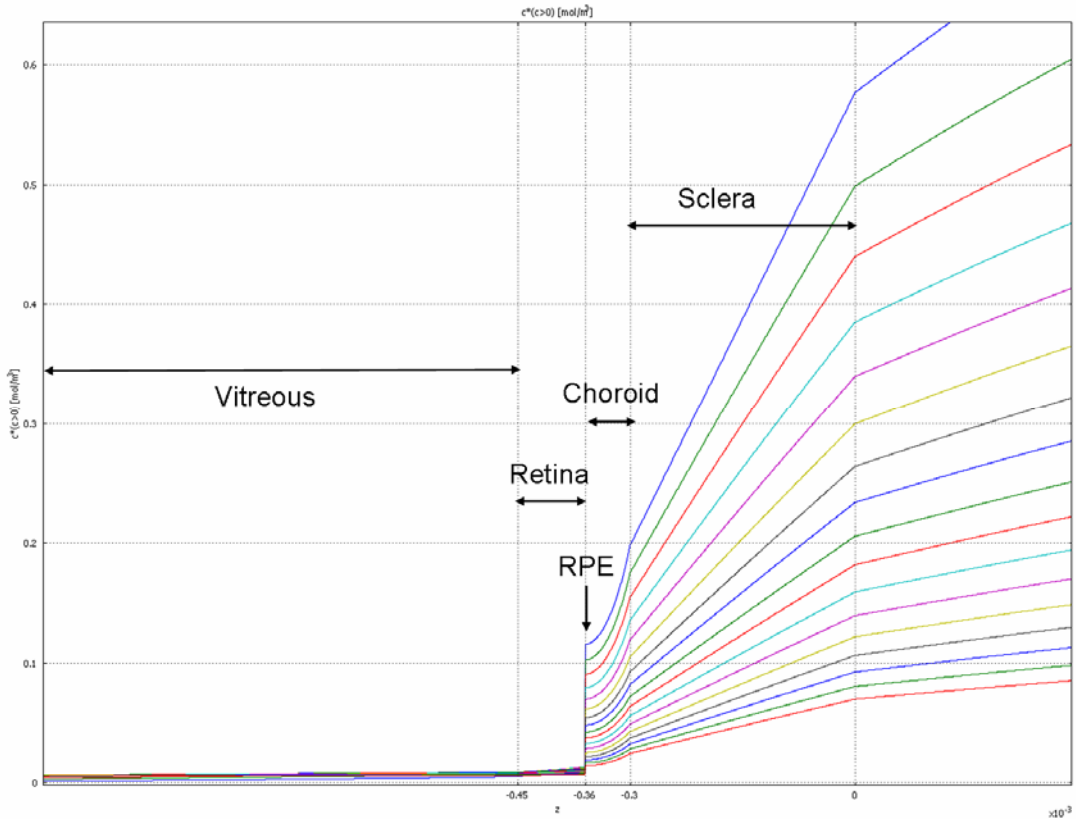

Figure 5-15. Increased magnification of concentration profiles shown in Figure 5-14.

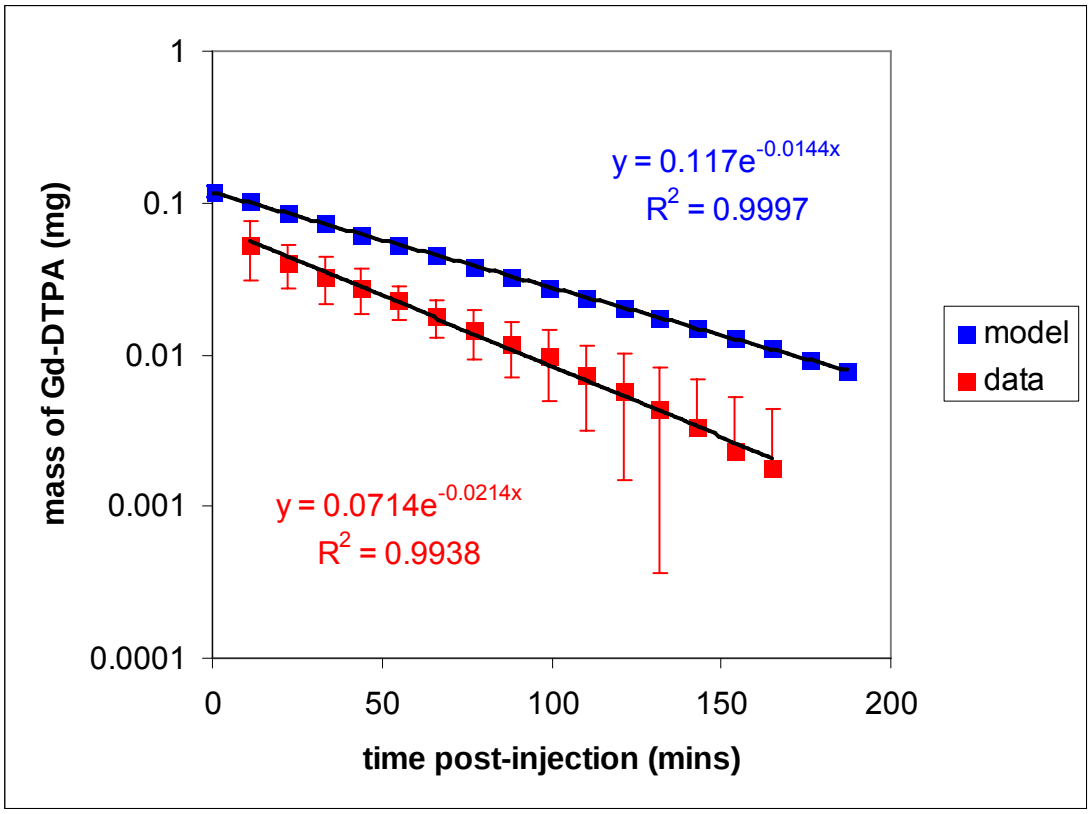

Figure 5-16. A comparison of the mass clearance of Gd-DTPA from the *in vivo* model and the MRI data.

Figure 5-16 shows the mass clearance plot comparing the model results to the MRI data. The model results follow the decreasing trend of MRI data in mass clearance. The k values from the model and MRI data are comparable (k=0.0144 and 0.0214 min^{-1}, respectively).

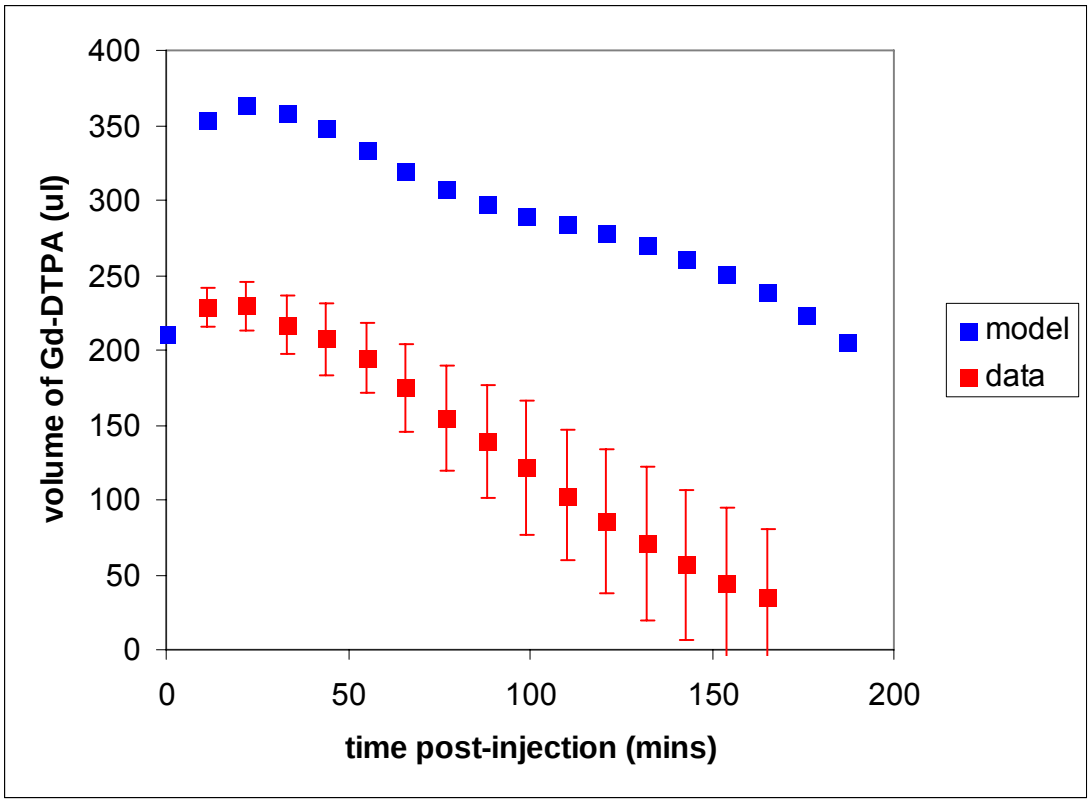

Figure 5-17. A comparison of the distribution volume of Gd-DTPA from the *in vivo* model and the MRI data.

Figure 5-17 compares the changes in apparent volume of the model and MRI data. The model predicts an initial increase in volume with a peak time at around 22 minutes before exhibiting decrease in volume. This trend is also displayed by the MRI data. The rate of volume decrease is similar for both the model and the MRI data but the model shows a much higher volume of distribution of Gd-DTPA.

5.3.3. Effect of thresholding

Analysis performed without thresholding in the *in vivo* model produces a k value (0.0132 min^{-1}) that is slightly lower than the k value determined after thresholding at 0.03 mM (0.0144 min^{-1}). The mass clearance rate is decreased when thresholding is not applied since elements with concentrations less than 0.03 mM are included in the concentration integration, increasing the total mass. After thresholding, the concentration values in the retina and vitreous are shown to be near zero (Figure 5-15), but more significant concentrations may actually be present in these tissues.

Figure 5-18 shows the individual tissue average concentrations of Gd-DTPA without thresholding *in vivo*. The plot indicates that the concentrations in the conjunctiva and sclera are one log less than the adjacent injection bolus. Average concentration levels in the choroid are about 2-3 log units below the injection concentration, and concentrations in the retina and vitreous are about 4 orders of magnitude below the injection concentration.

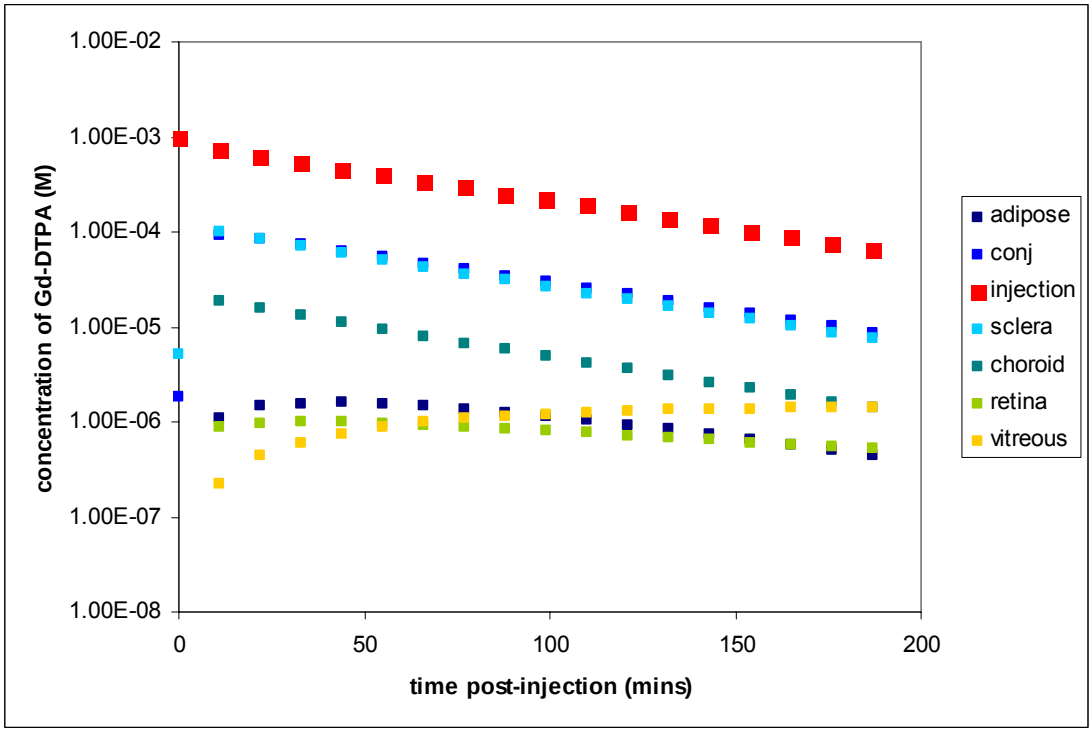

Figure 5-18. Individual average tissue concentrations of Gd-DTPA from the *in vivo* model.

5.3.4. Sensitivity analysis

A sensitivity analysis was performed by varying the diffusion coefficients and clearance constants in the *in vivo* model. All parameters were doubled in value (except run 5, where the permeability of the RPE is increased by an order of magnitude) and solved as a separate run. Table 5-7 summarizes the values varied in each run.

Run #	1	2	3	4	5	6	7
Subdomain	**Diffusion Coefficient (m^2/s)**						
sclera	2.60E-10	5.20E-10	2.60E-10	2.60E-10	2.60E-10	2.60E-10	2.60E-10
conjunctiva	2.20E-10	2.20E-10	2.20E-10	2.20E-10	2.20E-10	2.20E-10	2.20E-10
vitreous	5.30E-10	5.30E-10	5.30E-10	5.30E-10	5.30E-10	5.30E-10	5.30E-10
adipose	2.00E-10	2.00E-10	2.00E-10	2.00E-10	2.00E-10	2.00E-10	2.00E-10
choroid	2.20E-10	2.20E-10	4.40E-10	2.20E-10	2.20E-10	2.20E-10	2.20E-10
retina	2.10E-10	2.10E-10	2.10E-10	4.20E-10	2.10E-10	2.10E-10	2.10E-10
injection	5.30E-10	5.30E-10	5.30E-10	5.30E-10	5.30E-10	5.30E-10	5.30E-10
RPE	4.90E-13	4.90E-13	4.90E-13	4.90E-13	4.90E-12	4.90E-13	4.90E-13
Subdomain	**CL (s^{-1})**						
conjunctiva	-0.00041	-0.00041	-0.00041	-0.00041	-0.00041	-0.00041	-0.00082
adipose	-0.0003	-0.0003	-0.0003	-0.0003	-0.0003	-0.0003	-0.0003
choroid	-0.13	-0.13	-0.13	-0.13	-0.13	-0.26	-0.13

Table 5-7. Model parameters varied for sensitivity analysis.

Varied parameters are highlighted in blue.

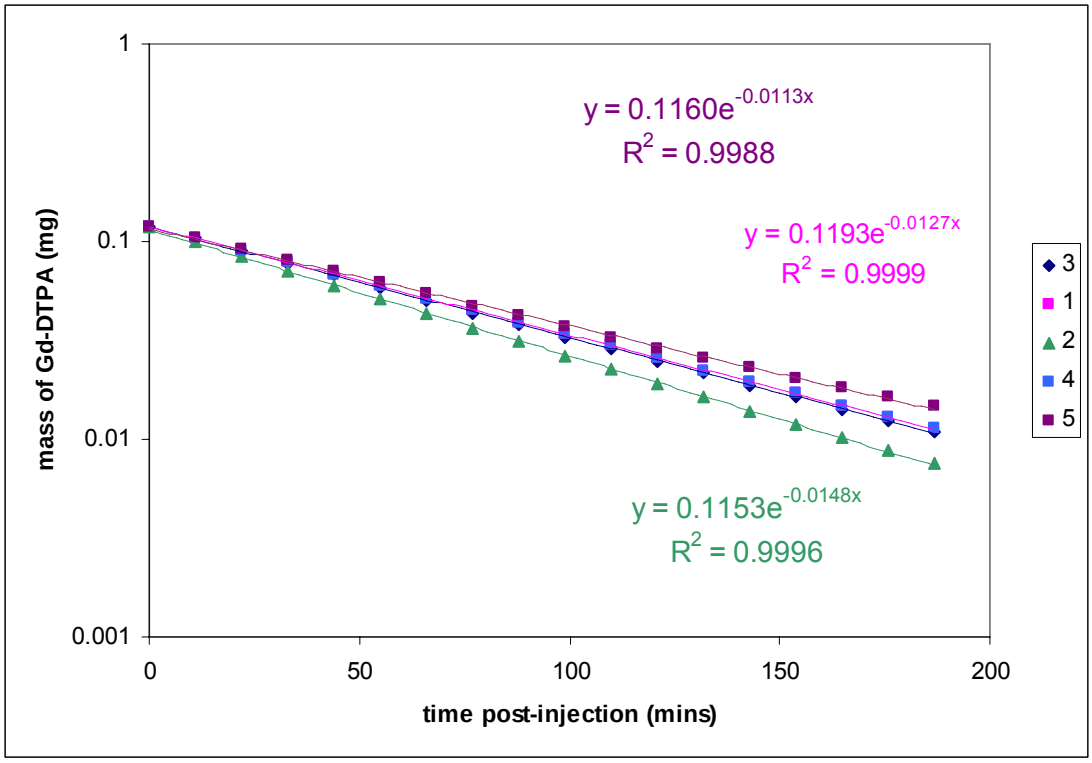

Figure 5-19. Effect of varying the diffusion coefficient of various tissues on mass clearance rate.

Regression lines and equations are given for runs 1, 2 and 5.

Mass clearance plots from runs 1-5 are shown in Figure 5-19. Changing the permeability of the choroid (run 3) and retina (run 4) did not significantly alter the mass clearance rate. Doubling the permeability of the sclera (run 2) resulted in the most significant change in k value (0.0148 min^{-1}). Increasing the permeability of the RPE (run 5) by an order of magnitude decreased the mass clearance rate (0.0113 min^{-1}), since this allows higher amounts of Gd-DTPA to accumulate in inner tissues such

as the retina and vitreous. This effect can be seen from the concentration profiles in Figure 5-20.

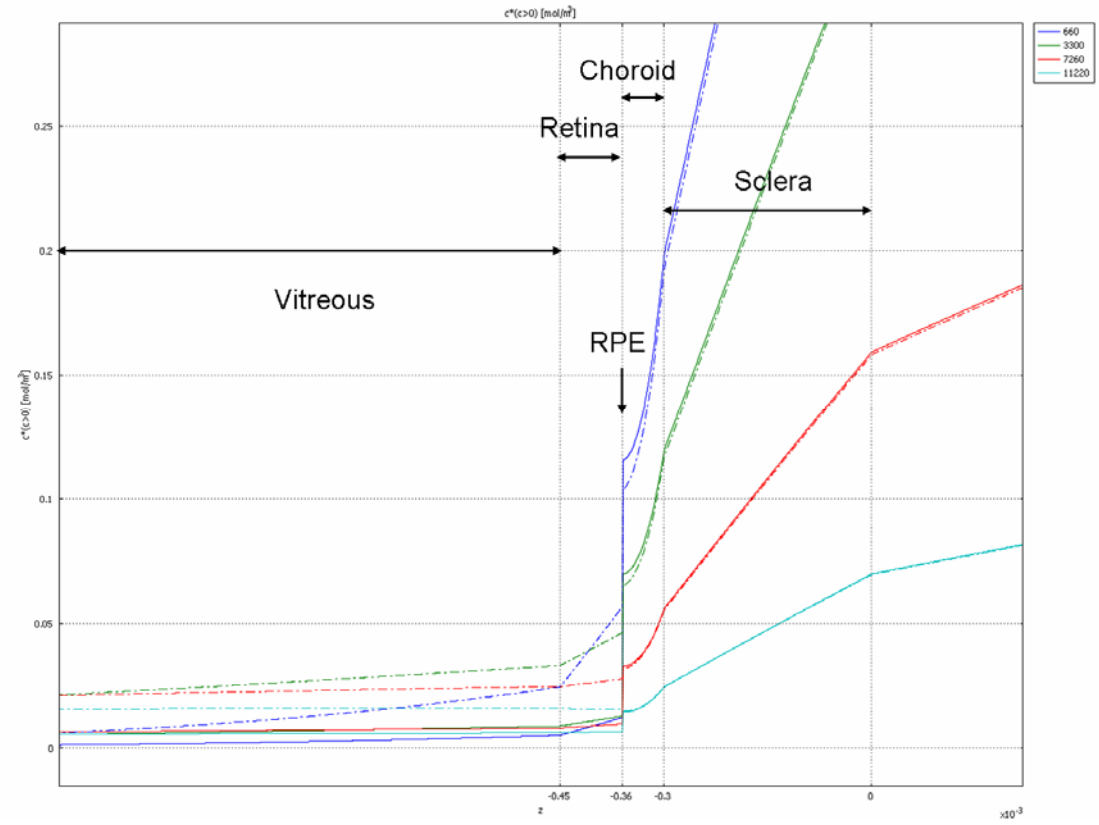

Figure 5-20. Effect of doubling RPE permeability on tissue concentration.

Solid lines correspond to run 1, dashed lines correspond to run 5. Represented times: 11, 55, 121, and 187 minutes post-injection.

Doubling either the choroidal or conjunctival clearance constant produced negligible changes in mass clearance rate. The k values were 0.137 and 0.139 min^{-1} for runs 6 and 7, respectively.

5.3.4. Conjunctival vs. choroidal clearance

The theoretical model can also be used to understand the effect of various transport barriers in the eye. The separate contribution of conjunctival and choroidal clearance in drug elimination was investigated by running the *in vivo* model with an absence of clearance in either the conjunctiva or the choroid. The resulting mass clearance values (k) are shown below in Table 5-8.

	k (min^{-1})
***In vivo* model**	0.0132
No conjunctival clearance model	0.0112
No choroidal clearance model	0.0020
***Post mortem* model**	0.0008

Table 5-8. Summary of mass clearance values (k) from model simulations.

Eliminating conjunctival clearance produces a slightly lower mass clearance value than the *in vivo* model result. Eliminating choroidal clearance drastically reduces the k value, resulting in a low clearance rate which is comparable to the *post*

mortem k value. These model simulations show that the choroidal clearance term needs to be included in order to produce results that resemble the *in vivo* results. Conjunctival clearance (without choroidal clearance) is not sufficient to clear the high amounts of drug from the subconjunctival depot as seen from *in vivo* studies. Therefore, *in vivo*, a significant fraction of the delivered amount of drug must be cleared by the choroid. The model indicates that the choroid plays a more significant role in the clearance of drugs after subconjunctival injection than the conjunctiva, which is in contrast to several current papers which suggest that the conjunctiva may play a more significant role [52,209].

5.3.5. Unidirectional Implant

A recent paper explored the use of a unidirectional implant that permitted NaF release toward the choroid exclusively [56]. Drug exposure to the conjunctival clearance mechanisms was minimized by the use of this unidirectional implant. Higher amounts of NaF were detected in the retina by use of *in vivo* fluorophotometry after delivery by the implant than compared to a bolus injection. To investigate the effect of unidirectionality on drug delivery to target tissues (choroid and retina), an impermeable boundary was established in the *in vivo* model by assigning a very low diffusion coefficient (10^{-20} m^2/s) over a 10 micron thickness at the interface between the injection depot and the conjunctiva.

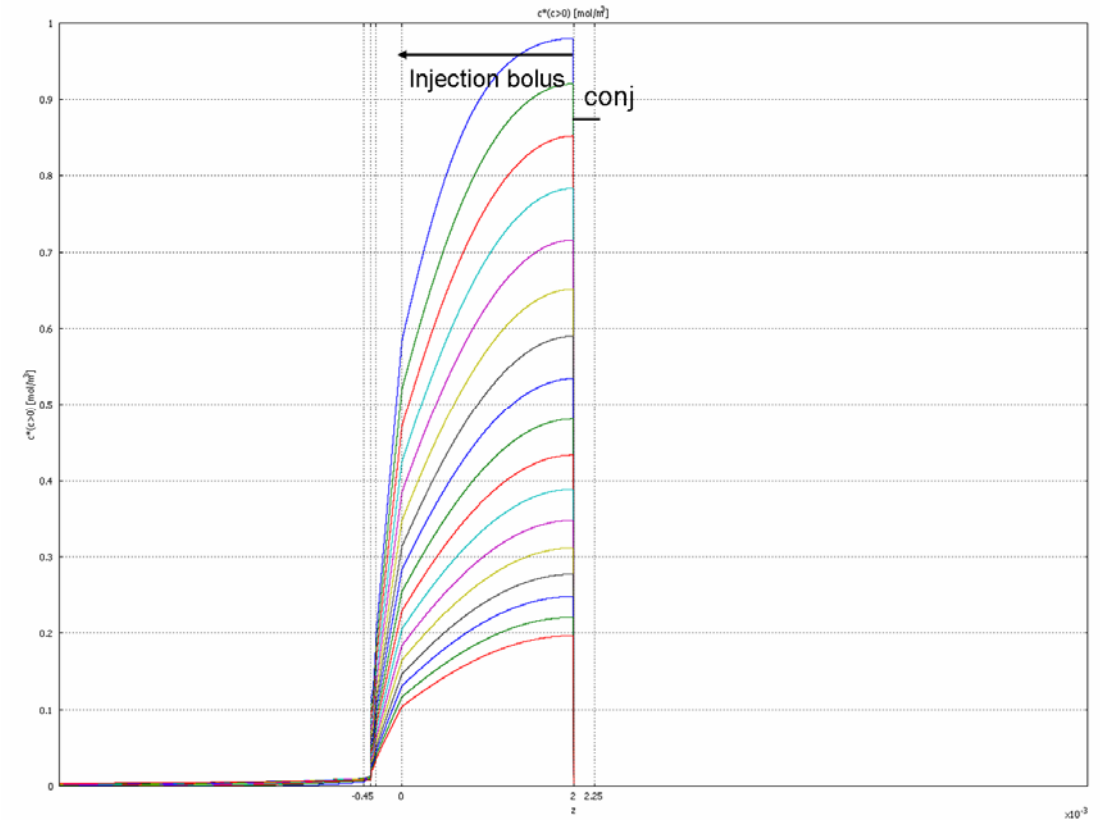

Figure 5-21. Concentration profiles from the unidirectional model simulation.

Figure 5-21 shows that by the implementation of the low diffusion coefficient at the boundary between the injection depot and the conjunctiva, Gd-DTPA is forced to penetrate toward the choroid and no concentrations of Gd-DTPA are detected in the conjunctiva. Despite the reduced exposure to the conjunctiva, steep gradients are established in the sclera and choroid and negligible concentrations of Gd-DTPA are found in the retina and vitreous.

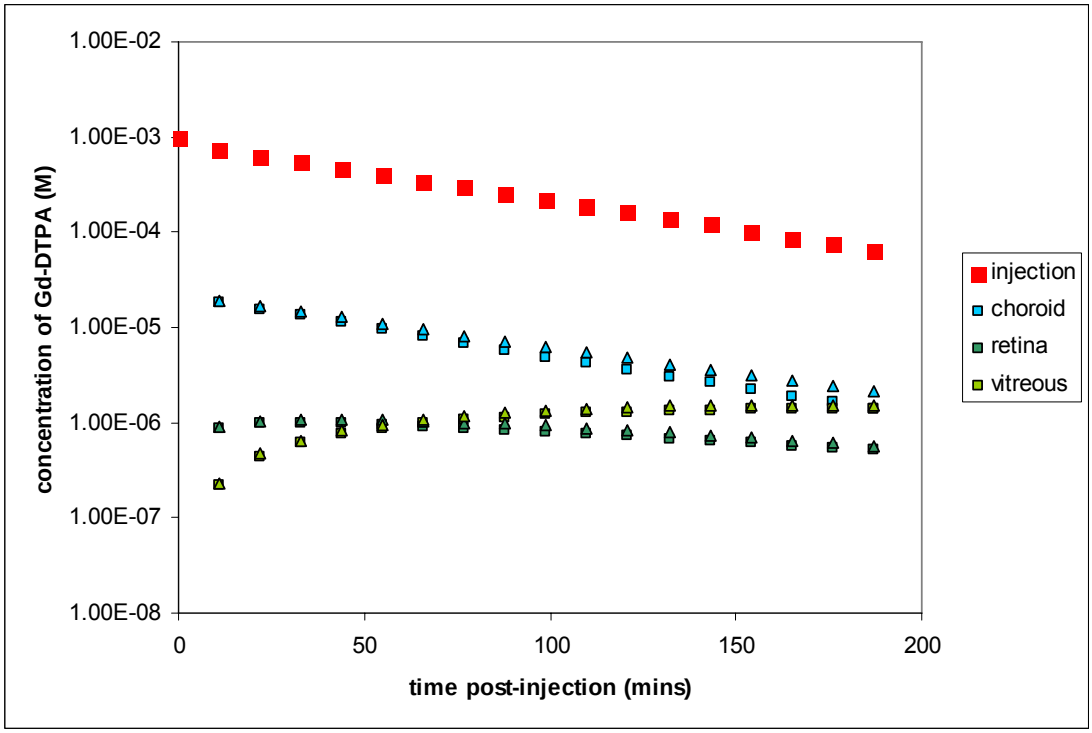

Figure 5-22. Comparison of average concentration levels in target tissues after delivery by unidirectional implant and bolus injection.

Triangles: unidirectional implant; squares: bolus injection

Figure 5-22 shows a comparison of the Gd-DTPA concentrations in target tissues (choroid and retina) after delivery by the unidirectional implant and by bolus injection. The plot shows that the concentration levels are almost identical in the target tissues in these delivery methods. The k value for the unidirectional implant is 0.0112 min^{-1}, which is the same as the k value determined from the model without conjunctival clearance (Table 5-8). Therefore, the use of a unidirectional implant will produce the same effect as selectively eliminating conjunctival clearance.

5.4. Discussion

5.4.1. Model vs. MRI results

The *post mortem* model predicted a decrease in total mass of Gd-DTPA in ocular tissues, but the k value is about 5 times less than that from the MRI results. The k value predicted by the *in vivo* model, however, is only about 1.5 times less than that from the MRI results. The *in vivo* k values from the model and MRI can be considered comparable, but the discrepancy in the *post mortem* k values is more significant.

One explanation for the large difference *post mortem* may be the effect of rigor mortis in *post mortem* scans. Immediately after death, rigor mortis decreases T_2 relaxation in tissues as they stiffen. As shown in Figure 5-23, as T_2 decreases, signal intensity also decreases. This may account for the more rapid "clearance" of Gd-DTPA in *post mortem* MRI scans, as Gd-DTPA present in surrounding tissues may not produce sufficient signal intensity to be detected on MR images.

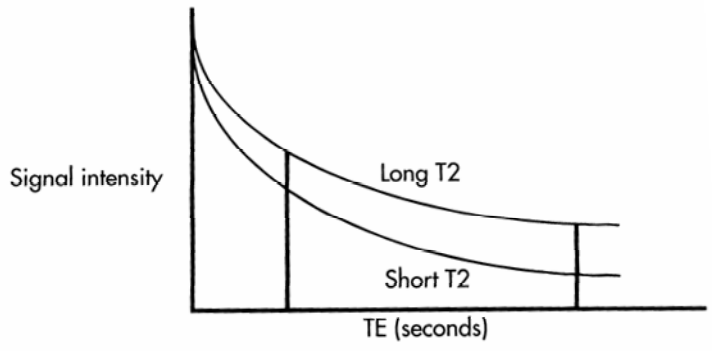

Figure 5-23. The effect of T_2 on signal intensity at a specified TE.
From reference [136].

In this research, signal intensities were used to determine the concentration and mass of Gd-DTPA. Therefore, the accuracy in the conversion of signal intensity to concentration will always have a major effect on the results. As discussed in previous chapters, the use of PBS phantoms may not correctly reflect the signal intensity changes with concentration in tissues. In the results from the *post mortem* model, a significant portion of Gd-DTPA concentration is detected in tissues outside the injection bolus. Some of the discrepancy between the model and data may be due to differences in relaxation rates in ocular tissues, resulting in an incorrect conversion of signal intensity from the use of a calibration curve based on PBS in tissue regions.

Another reason for the faster mass decrease in the MRI *post mortem* scans may be due to the effect of volume averaging. The MR images show average concentrations in each voxel and the finite element model shows average concentrations determined in each element. The voxel size in MR images is 0.703 mm × 0.179 mm × 0.703 mm and is relatively large compared to tissue thickness (conjunctiva is about 0.3 mm). Some voxels may lie in areas where they encompass 2 or more regions that have significantly different concentration values (especially at tissue boundaries). As the voxel assumes an average concentration value, if the average is sufficiently low, it may fall below the concentration threshold. This will result in fewer voxels that remain after thresholding, and will decrease the total amount of Gd-DTPA detected. As less voxels are found to be above the concentration threshold, a faster decrease in total mass will result. The decrease in the number of voxels will also decrease the apparent volume.

On the other hand, the finite element model is highly discretized and is composed of elements that are much smaller compared to the MR image voxels. Therefore, the model is better able to capture regions that have steep concentration gradients or regions that have low concentrations (but higher than 0.03 mM) of Gd-DTPA. The large apparent volume predicted by the model reflects the large area into which Gd-DTPA has diffused in the adipose tissue and vitreous, but is not detected by MRI.

The effect of volume averaging also applies to the *in vivo* MRI scans, and therefore the k values from these experiments may be an overestimate. Then there may actually be a smaller difference in k values from the model and MRI results, indicating that the model produces very reasonable results which are in line with the experimental data.

5.4.2. Concentration levels in individual tissues

When thresholding is applied to MR images, regions of low concentrations of Gd-DTPA cannot be observed. The *in vivo* model results without thresholding gives an estimate of the low concentration levels of Gd-DTPA that are found in various tissues including the retina and vitreous, where concentrations are typically very low. As shown in Figure 5-18, drug levels in the choroid are about 2-3 log units below the administered concentration and about 4-5 log units below the injection concentration in the retina and vitreous. The model can be useful in predicting the low concentration levels of drug in individual tissues, which may be more difficult with current MRI methods due to limitations in spatial and temporal resolution.

5.4.3. Sensitivity Analysis

Sensitivity analysis was performed by doubling the diffusion coefficients and clearance rate constants. Doubling the diffusion coefficient did not have a major effect on mass clearance rate except in the sclera, where the higher diffusion coefficient resulted in greater clearance, most likely through the choroid. Absorption enhancers have been proposed to increase transscleral drug delivery of drugs by increasing the permeability of the sclera [21,210,211], but their therapeutic efficacy for posterior segment disorders has not been demonstrated *in vivo*. Increasing the permeability of the RPE by one log unit permitted greater amounts of Gd-DTPA to accumulate in the retina and vitreous. Therefore, increasing the permeability of the RPE may be a more effective method for increasing drug delivery to the retina.

Doubling the clearance rate either in the conjunctiva or the choroid produced negligible changes in mass clearance rate. An explanation for the mostly insignificant changes in clearance rate resulting from the sensitivity analysis may be found by comparing the significance of drug elimination in each tissue due to tissue permeability (R_p) and tissue clearance rate (R_c).

The rate of drug elimination from a tissue is determined by the rate of permeation of the drug through the tissue (R_p): $\frac{D \times S}{\delta}$ (where D: tissue diffusion coefficient, S: surface area and δ: tissue thickness) and the rate of clearance by blood flow (R_c): $CL \times V$ (where CL: clearance rate determined from equation 4 and V: tissue

volume). Table 5-9 shows the calculated rates of R_p and R_c in the conjunctiva and choroid.

Tissue	$R_P = \frac{D \times S}{\delta}$	$R_C = CL \times V$
Conjunctiva	**0.021 g/min** (D: 2.2e-10 m^2/s S: 4.78e-4 m^2 δ: 0.0003 m)	**0.0029 g/min** (CL: 0.00041 s^{-1} V: 0.24 g)
Choroid	**0.10 g/min** (D: 2.2e-10 m^2/s S: 4.52e-4 m^2 δ: 0.00006 m)	**0.21 g/min** (CL: 0.13 s^{-1} V: 0.048 g)

Table 5-9. Comparison of R_P and R_C in the conjunctiva and choroid.

The values for R_p and R_c in the choroid are significantly higher than that in the conjunctiva. This indicates that drug clearance in the choroid is much more significant than clearance in the conjunctiva. The table also shows that the R_p and R_c values are similar in the choroid, but they differ by an order of magnitude in the conjunctiva. This shows that more drug molecules are removed from the conjunctiva by diffusion of the drug out of the tissue rather than by clearance through conjunctival blood vessels. Therefore, the lower value, R_c, is rate-limiting in the conjunctiva, and

in order to produce a significant increase in drug clearance, R_c must be increased as increases in R_p will not have an effect. In this sensitivity analysis, the effect of doubling CL was investigated, but greater changes in CL may be required to see significant increases in mass clearance rate.

In the choroid, diffusion of the drug out of the tissue and clearance of the drug through the choroidal circulation are both equally high in magnitude. Nevertheless, R_p is rate-limiting, and since in this sensitivity analysis R_c was altered, this did not produce a significant change in mass clearance rate.

This analysis provides useful information regarding the drug clearance mechanisms in the choroid and conjunctiva. The high permeability of the conjunctiva and choroid is advantageous in transscleral drug delivery since diffusion is the most significant method of intraocular drug transport. The low clearance rate in the conjunctiva is also beneficial, but the rapid clearance in the choroid will significantly decrease the bioavailability of drug in the eye. If drug clearance through the choroidal circulation can be decreased, a much greater yield in the retina will result. One method to decrease choroidal clearance is to increase the drug size by encapsulating the drug inside nano- or microparticles. Substantial increases in drug size will hinder the diffusion of drugs through ocular tissues, but will also decrease the diffusion of drugs into the choroidal vessels as well. Several recent studies have shown the successful delivery of particles to the retina after subconjunctival injection [12,13,212]. These particles have been found to have crossed the RPE barrier, possibly by endocytosis.

5.4.4. Conjunctival vs. choroidal clearance

The significance of conjunctival clearance in transscleral delivery has been described in several reports [52,105,209]. Therefore, it was of interest to investigate the impact of conjunctival clearance in the absence of choroidal blood flow. The model results and analysis from the previous section on the low R_c and R_p values in the conjunctiva demonstrate that the conjunctiva is responsible for clearing some of the drug, but is not as significant as clearance by the choroid. The results from the unidirectional implant show that having an impermeable boundary between the drug and the conjunctiva will help to decrease the rate of mass clearance. However, unidirectionality is not sufficient for delivering higher drug amounts to the choroid and retina. Using a sustained-release formulation in addition to a unidirectional implant may help to increase delivery of drugs to the posterior segment.

5.5. Conclusion

The model results *in vivo* and *post mortem* showed similar trends found from MRI experiments for subconjunctival delivery of Gd-DTPA by injection. Useful information regarding the contributions of various clearance mechanisms on drug elimination and delivery could be studied by analyzing the model results. The most significant barrier to successful transscleral drug delivery may be the choroidal circulation, and delivery methods that can overcome this barrier may yield significantly high drug levels in the retina.

Chapter 6: Summary and Recommendations for Future Work

6.1. Project Summary

Several objectives were achieved in this work. First, drug delivery by the transscleral route was assessed by using a pharmacokinetic imaging method, DCE-MRI. Sustained transscleral delivery was evaluated by using continuous infusions of Gd-DTPA either subconjunctivally or intrasclerally. Intrascleral infusion enabled Gd-DTPA to move to the macular region by traveling through the suprachoroidal space. Gd-DTPA was not detected in the choroid/retina after subconjunctival infusions. Sustained release delivery systems may yield more effective drug delivery to the retina after intrascleral administration rather than subconjunctival.

DCE-MRI was evaluated as a pharmacokinetic imaging tool for assessing drug delivery in the eye. There are current limitations in spatial and temporal resolution that need to be considered in order to correctly measure the desired outcomes by MR imaging. There is also some concern when trying to measure concentration levels in tissues since standardized tissue phantoms are currently lacking. Continued improvements in coil design, magnet systems, and MR sequences amongst other advances may help to further the capability and reliability of DCE-MRI as a pharmacokinetic imaging tool.

Despite current limitations in MR imaging, DCE-MRI was successfully used to investigate drug elimination kinetics after subconjunctival delivery. Basic concepts such as the rate of drug clearance and drug retention in the subconjunctival depot have not been investigated due to the difficulty in acquiring concentration

measurements *in vivo*. Using DCE-MRI, data was acquired for subconjunctival injections of Gd-DTPA and Gd-albumin and it was determined that lymphatic flow may not be a significant contributor to drug clearance. Larger injection volumes also decreased the rate of mass clearance and allowed for longer retention times of drug in the depot.

A distributed pharmacokinetic model for subconjunctival injection was built using the finite element method and the results compared with the experimental results from MRI. The model results were comparable to MRI results, and further analysis of the model yielded additional information regarding the contributions of various clearance mechanisms in the eye. Increasing the permeability of the RPE produced higher levels of drug in the retina compared to increasing the permeability of the sclera. In light of this model result and the experimental results from Chapter 3, efforts to increase the permeability of drug formulations through the RPE may yield more effective results in terms of delivery to the retina rather than utilizing sustained release formulations from the subconjunctival space. Also, the use of drug encapsulated particles may also allow greater delivery to the retina since an increase in drug size will decrease clearance by the choroidal circulation.

6.2. Recommendations for Future Work

For future study, the use of a second measurement technique is recommended to obtain data that cannot be acquired with MRI, due to the limitations in the DCE-MRI technique. MRI provides good anatomical information but lacks sensitivity at the molecular level. This can be investigated using another imaging modality in

conjunction with MRI such as PET or MRS. This will dramatically expand the capability of imaging tools for use in drug delivery as small drug targets can now be assessed *in vivo*.

The results from this work pertain only to hydrophilic substances since only Gd-DTPA and Gd-albumin have been investigated as model drugs. However, many ophthalmic drugs are lipophilic and are not water soluble. It would be of interest to investigate the effects of a lipophilic contrast agent and compare the results to this study. This is difficult to accomplish however, since water insoluble contrast agents are not manufactured as aqueous solubility is desired in the clinical setting. It would also be beneficial to image an actual drug molecule and not a contrast agent, since the drug and contrast agent may exhibit different behavior in terms of metabolism, absorption and clearance. It may be worthwhile to conduct a study to conjugate Gd or another paramagnetic ion to a drug molecule for MR imaging.

Similarly, the pharmacokinetic model may be adjusted to give results for lipophilic substances. The diffusion coefficients and clearance values can be altered to study the effect of larger therapeutic proteins as well. The current model only includes the effect of static barriers and clearance by blood flow. As discussed in Chapter 1, many other barriers exist, such as bulk fluid flows, metabolism and active transport. It would be more difficult to correctly account for these barriers in the model since very few experiments have been conducted to measure these effects. However, the increased use of *in vivo* imaging modalities may enable the ability to acquire parameters that can be used to build more accurate pharmacokinetic models. Advances in pharmacokinetic imaging tools in parallel with pharmacokinetic

modeling may help to address the enormous need for effective delivery methods in the eye.

Chapter 7: Appendix

Calculation of diffusion coefficients

1. Calculation of the diffusion coefficient of Gd-DTPA (590 Da) in water at 37°C

Using the correlation for dilute aqueous binary diffusion coefficients at 25°C (Handbook of Physics & Chemistry, 75th Ed. Pg. 6-253):

$$D_{\infty}^{25°C} \times 10^5 = 9.225 \times MW^{-0.494} \tag{1}$$

where D is in cm^2/s. For Gd-DTPA,

$$D_{\infty}^{25°C} \times 10^5 = 9.225 \times 590^{-0.494}$$

$$D_{\infty}^{25°C} = 3.96^{-10}\ m^2/s$$

The diffusion coefficient at 37°C can be determined using Trout's rule correction:

$$D_{\infty}^{37°C} = \left(\frac{T^{37°C} \cdot \mu^{25°C}}{T^{25°C} \cdot \mu^{37°C}} \right) D_{\infty}^{25°C} \tag{2}$$

$$D_{\infty}^{37°C} = \left(\frac{310.3 \cdot 0.8937}{298.3 \cdot 0.6947}\right) 3.96^{-10}\, m^2/s = 5.3^{-10}\, m^2/s$$

2. Calculation of the diffusion coefficient of Gd-DTPA in ocular tissues

The diffusion coefficient of solutes in brain tissue is estimated by:

$$D_e = \frac{D_{\infty}}{\lambda^2} \tag{3}$$

where λ=1.6 for brain tissue. Therefore,

$$D_e = \frac{5.3^{-10}\, m^2/s}{1.6^2} = 2.07^{-10}\, m^2/s$$

for Gd-DTPA in brain tissue. The volume void fraction of brain tissue is 0.21 [213]. The diffusion coefficients of other tissues can be calculated by a relation of the void fractions [188]:

$$D_e^a = \left(\frac{3-\phi_e^b}{3-\phi_e^a}\right) D_e^b \tag{4}$$

For example, the diffusion coefficient of Gd-DTPA in sclera is:

$$D_e^{sclera} = \left(\frac{3 - \phi_e^{brain}}{3 - \phi_e^{sclera}} \right) D_e^{brain} = \left(\frac{3 - 0.21}{3 - 0.8} \right) 2.07^{-10} = 2.63^{-10}\, m^2 / s$$

The remaining diffusion coefficients for various ocular tissues are tabulated in Table 5-3.

Bibliography

1. Ferris FL, 3rd, Tielsch JM: Blindness and visual impairment: a public health issue for the future as well as today. Arch Ophthalmol 2004;122:451-452.

2. Friedman DS, O'Colmain BJ, Munoz B, Tomany SC, McCarty C, de Jong PT, Nemesure B, Mitchell P, Kempen J: Prevalence of age-related macular degeneration in the United States. Arch Ophthalmol 2004;122:564-572.

3. Geroski DH, Edelhauser HF: Drug delivery for posterior segment eye disease. Invest Ophthalmol Vis Sci 2000;41:961-964.

4. Raghava S, Hammond M, Kompella UB: Periocular routes for retinal drug delivery. Expert Opin Drug Deliv 2004;1:99-114.

5. Lee SS, Yuan P, Robinson MR: Ocular Implants for Drug Delivery. in Bowlin GL, Wnek G (eds): Encyclopedia of Biomaterials and Biomedical Engineering. New York: Marcel Dekker, 2004, 1105-1118.

6. Lee VH, Robinson JR: Topical ocular drug delivery: recent developments and future challenges. J Ocul Pharmacol 1986;2:67-108.

7. Urtti A: Challenges and obstacles of ocular pharmacokinetics and drug delivery. Adv Drug Deliv Rev 2006;58:1131-1135.

8. Cunha-Vaz J: The blood-ocular barriers. Surv Ophthalmol 1979;23:279-296.

9. Hughes PM, Olejnik O, Chang-Lin JE, Wilson CG: Topical and systemic drug delivery to the posterior segments. Adv Drug Deliv Rev 2005;57:2010-2032.

10. Davis JL, Gilger BC, Robinson MR: Novel approaches to ocular drug delivery. Curr Opin Mol Ther 2004;6:195-205.

11. Ayalasomayajula SP, Kompella UB: Retinal delivery of celecoxib is several-fold higher following subconjunctival administration compared to systemic administration. Pharm Res 2004;21:1797-1804.

12. Ayalasomayajula SP, Kompella UB: Subconjunctivally administered celecoxib-PLGA microparticles sustain retinal drug levels and alleviate diabetes-induced oxidative stress in a rat model. Eur J Pharmacol 2005;511:191-198.

13. Kompella UB, Bandi N, Ayalasomayajula SP: Subconjunctival nano- and microparticles sustain retinal delivery of budesonide, a corticosteroid capable of inhibiting VEGF expression. Invest Ophthalmol Vis Sci 2003;44:1192-1201.

14. Gilbert JA, Simpson AE, Rudnick DE, Geroski DH, Aaberg TM, Jr., Edelhauser HF: Transscleral permeability and intraocular concentrations of cisplatin from a collagen matrix. J Control Release 2003;89:409-417.

15. Zignani M, Einmahl S, Baeyens V, Varesio E, Veuthey JL, Anderson J, Heller J, Tabatabay C, Gurny R: A poly(ortho ester) designed for combined ocular delivery of dexamethasone sodium phosphate and 5-fluorouracil:

subconjunctival tolerance and in vitro release. Eur J Pharm Biopharm 2000;50:251-255.

16. Wang G, Tucker IG, Roberts MS, Hirst LW: In vitro and *in vivo* evaluation in rabbits of a controlled release 5-fluorouracil subconjunctival implant based on poly(D,L-lactide-co-glycolide). Pharm Res 1996;13:1059-1064.

17. Kato A, Kimura H, Okabe K, Okabe J, Kunou N, Ogura Y: Feasibility of drug delivery to the posterior pole of the rabbit eye with an episcleral implant. Invest Ophthalmol Vis Sci 2004;45:238-244.

18. Okabe K, Kimura H, Okabe J, Kato A, Kunou N, Ogura Y: Intraocular tissue distribution of betamethasone after intrascleral administration using a non-biodegradable sustained drug delivery device. Invest Ophthalmol Vis Sci 2003;44:2702-2707.

19. Okabe J, Kimura H, Kunou N, Okabe K, Kato A, Ogura Y: Biodegradable intrascleral implant for sustained intraocular delivery of betamethasone phosphate. Invest Ophthalmol Vis Sci 2003;44:740-744.

20. Ambati J, Gragoudas ES, Miller JW, You TT, Miyamoto K, Delori FC, Adamis AP: Transscleral delivery of bioactive protein to the choroid and retina. Invest Ophthalmol Vis Sci 2000;41:1186-1191.

21. Okabe K, Kimura H, Okabe J, Kato A, Shimizu H, Ueda T, Shimada S, Ogura Y: Effect of benzalkonium chloride on transscleral drug delivery. Invest Ophthalmol Vis Sci 2005;46:703-708.

22. Bonini-Filho MA, Jorge R, Barbosa JC, Calucci D, Cardillo JA, Costa RA: Intravitreal injection versus sub-Tenon's infusion of triamcinolone acetonide for refractory diabetic macular edema: a randomized clinical trial. Invest Ophthalmol Vis Sci 2005;46:3845-3849.

23. Cardillo JA, Melo LA, Jr., Costa RA, Skaf M, Belfort R, Jr., Souza-Filho AA, Farah ME, Kuppermann BD: Comparison of intravitreal versus posterior sub-Tenon's capsule injection of triamcinolone acetonide for diffuse diabetic macular edema. Ophthalmology 2005;112:1557-1563.

24. Kim SH, Lutz RJ, Wang NS, Robinson MR: Transport Barriers in Transscleral Drug Delivery for Retinal Diseases. Ophthalmic Res 2007;39:244-254.

25. Ambati J, Adamis AP: Transscleral drug delivery to the retina and choroid. Prog Retin Eye Res 2002;21:145-151.

26. Kansara V, Mitra AK: Evaluation of an *ex vivo* model implication for carrier-mediated retinal drug delivery. Curr Eye Res 2006;31:415-426.

27. Prausnitz MR, Noonan JS: Permeability of cornea, sclera, and conjunctiva: a literature analysis for drug delivery to the eye. J Pharm Sci 1998;87:1479-1488.

28. Ambati J, Canakis CS, Miller JW, Gragoudas ES, Edwards A, Weissgold DJ, Kim I, Delori FC, Adamis AP: Diffusion of high molecular weight compounds through sclera. Invest Ophthalmol Vis Sci 2000;41:1181-1185.

29. Hamalainen KM, Kananen K, Auriola S, Kontturi K, Urtti A: Characterization of paracellular and aqueous penetration routes in cornea, conjunctiva, and sclera. Invest Ophthalmol Vis Sci 1997;38:627-634.

30. Boubriak OA, Urban JP, Akhtar S, Meek KM, Bron AJ: The effect of hydration and matrix composition on solute diffusion in rabbit sclera. Exp Eye Res 2000;71:503-514.

31. Ahmed I, Gokhale RD, Shah MV, Patton TF: Physicochemical determinants of drug diffusion across the conjunctiva, sclera, and cornea. J Pharm Sci 1987;76:583-586.

32. Edwards A, Prausnitz MR: Fiber matrix model of sclera and corneal stroma for drug delivery to the eye. AIChE 1998;44:214-225.

33. Pitkänen L, Ranta VP, Moilanen H, Urtti A: Permeability of retinal pigment epithelium: effects of permeant molecular weight and lipophilicity. Invest Ophthalmol Vis Sci 2005;46:641-646.

34. Moore DJ, Hussain AA, Marshall J: Age-related variation in the hydraulic conductivity of Bruch's membrane. Invest Ophthalmol Vis Sci 1995;36:1290-1297.

35. Cruysberg LP, Nuijts RM, Geroski DH, Koole LH, Hendrikse F, Edelhauser HF: In vitro human scleral permeability of fluorescein, dexamethasone-fluorescein, methotrexate-fluorescein and rhodamine 6G and the use of a

coated coil as a new drug delivery system. J Ocul Pharmacol Ther 2002;18:559-569.

36. Cheruvu NP, Kompella UB: Bovine and porcine transscleral solute transport: influence of lipophilicity and the choroid-bruch's layer. Invest Ophthalmol Vis Sci 2006;47:4513-4522.

37. Maurice DM, Polgar J: Diffusion across the sclera. Exp Eye Res 1977;25:577-582.

38. Dunlevy JR, Rada JA: Interaction of lumican with aggrecan in the aging human sclera. Invest Ophthalmol Vis Sci 2004;45:3849-3856.

39. Kao JC, Geroski DH, Edelhauser HF: Transscleral permeability of fluorescent-labeled antibiotics. J Ocul Pharmacol Ther 2005;21:1-10.

40. Shuler RK, Jr., Dioguardi PK, Henjy C, Nickerson JM, Cruysberg LP, Edelhauser HF: Scleral permeability of a small, single-stranded oligonucleotide. J Ocul Pharmacol Ther 2004;20:159-168.

41. Cruysberg LP, Franklin AJ, Sanders J, Self C, Yuan P, Csaky KG, Robinson MR, Kohn EC, Edelhauser HF: Effective transscleral delivery of two retinal anti-angiogenic molecules: carboxyamido-triazole (CAI) and 2-methoxyestradiol (2ME2). Retina 2005;25:1022-1031.

42. Hussain AA, Rowe L, Marshall J: Age-related alterations in the diffusional transport of amino acids across the human Bruch's-choroid complex. J Opt Soc Am A Opt Image Sci Vis 2002;19:166-172.

43. Prince JH, Diesem CD, Eglitis I, Ruskell GL: The Rabbit. in Prince JH (ed): Anatomy and Histology of the Eye and Orbit in Domestic Animals. Charles C Thomas, 1960, 268.

44. Prince JH, Diesem CD, Eglitis I, Ruskell GL: The Dog. in Prince JH (ed): Anatomy and Histology of the Eye and Orbit in Domestic Animals. 1960, 73.

45. Prince JH, Diesem CD, Eglitis I, Ruskell GL: The Eyelids. in Prince JH (ed): Anatomy and Histology of the Eye and Orbit in Domestic Animals. Charles C Thomas, 1960, 46-47.

46. Sugar HS, Riazi A, Schaffner R: The bulbar conjunctival lymphatics and their clinical significance. Trans Am Acad Ophthalmol Otolaryngol 1957;61:212-223.

47. Gausas RE, Gonnering RS, Lemke BN, Dortzbach RK, Sherman DD: Identification of human orbital lymphatics. Ophthal Plast Reconstr Surg 1999;15:252-259.

48. Singh D: Conjunctival lymphatic system. J Cataract Refract Surg 2003;29:632-633.

49. Collin HB: The ultrastructure of conjunctival lymphatic anchoring filaments. Exp Eye Res 1969;8:102-105.

50. Gruntzig J, Schicha H, Kiem J, Becker V, Feinendegen LE: [Studies on the lymph drainage of the eye 5. Quantitative registration of the lymph drainage from the subconjunctival space with a radioactive tracer (author's transl)]. Klin Monatsbl Augenheilkd 1978;172:872-876.

51. Collin HB: Lymphatic drainage of 131-I-albumin from the vascularized cornea. Invest Ophthalmol 1970;9:146-155.

52. Robinson MR, Lee SS, Kim H, Kim S, Lutz RJ, Galban C, Bungay PM, Yuan P, Wang NS, Kim J, Csaky KG: A rabbit model for assessing the ocular barriers to the transscleral delivery of triamcinolone acetonide. Exp Eye Res 2006;82:479-487.

53. Amrite AC, Kompella UB: Size-dependent disposition of nanoparticles and microparticles following subconjunctival administration. J Pharm Pharmacol 2005;57:1555-1563.

54. Maurice DM, Ota Y: The kinetics of subconjunctival injections. Jpn. J. Ophthalmol 1978;22:95-100.

55. Robinson MR, Lee SS, Kim H, Kim S, Lutz RJ, Galban C, Bungay PM, Yuan P, Wang NS, Kim J, Csaky KG: A rabbit model for assessing the ocular barriers to the transscleral delivery of triamcinolone acetonide. Exp Eye Res 2005;82:479-487.

56. Pontes de Carvalho RA, Krausse ML, Murphree AL, Schmitt EE, Campochiaro PA, Maumenee IH: Delivery from episcleral exoplants. Invest Ophthalmol Vis Sci 2006;47:4532-4539.

57. Park J, Bungay PM, Lutz RJ, Augsburger JJ, Millard RW, Sinha Roy A, Banerjee RK: Evaluation of coupled convective-diffusive transport of drugs administered by intravitreal injection and controlled release implant. J Control Release 2005;105:279-295.

58. Kim H, Lizak MJ, Tansey G, Csaky KG, Robinson MR, Yuan P, Wang NS, Lutz RJ: Study of ocular transport of drugs released from an intravitreal implant using magnetic resonance imaging. Ann Biomed Eng 2005;33:150-164.

59. Sasaki H, Kashiwagi S, Mukai T, Nishida K, Nakamura J, Nakashima M, Ichikawa M: Drug absorption behavior after periocular injections. Biol Pharm Bull 1999;22:956-960.

60. Bill A: The aqueous humor drainage mechanism in the cynomolgus monkey (Macaca irus) with evidence for unconventional routes. Invest Ophthalmol 1965;4:911-919.

61. Inomata H, Bill A: Exit sites of uveoscleral flow of aqueous humor in cynomolgus monkey eyes. Exp Eye Res 1977;25:113-118.

62. Krohn J, Bertelsen T: Light microscopy of uveoscleral drainage routes after gelatine injections into the suprachoroidal space. Acta Ophthalmol Scand 1998;76:521-527.

63. Krohn J, Bertelsen T: Corrosion casts of the suprachoroidal space and uveoscleral drainage routes in the human eye. Acta Ophthalmol Scand 1997;75:32-35.

64. Bill A: The Drainage of Albumin from the Uvea. Exp Eye Res 1964;75:179-187.

65. Bill A: Movement of albumin and dextran through the sclera. Arch Ophthalmol 1965;74:248-252.

66. Fautsch MP, Johnson DH: Aqueous humor outflow: what do we know? Where will it lead us? Invest Ophthalmol Vis Sci 2006;47:4181-4187.

67. Bill A: Uveoscleral drainage of aqueous humor: physiology and pharmacology. Prog Clin Biol Res 1989;312:417-427.

68. Aihara M, Lindsey JD, Weinreb RN: Aqueous humor dynamics in mice. Invest Ophthalmol Vis Sci 2003;44:5168-5173.

69. Toris CB, Yablonski ME, Wang YL, Camras CB: Aqueous humor dynamics in the aging human eye. Am J Ophthalmol 1999;127:407-412.

70. Inomata H, Bill A, Smelser GK: Unconventional routes of aqueous humor outflow in Cynomolgus monkey (Macaca irus). Am J Ophthalmol 1972;73:893-907.

71. Machemer R: The importance of fluid absorption, traction, intraocular currents, and chorioretinal scars in the therapy of rhegmatogenous retinal detachments. XLI Edward Jackson memorial lecture. Am J Ophthalmol 1984;98:681-693.

72. Marmor MF: Mechanisms of retinal adhesion. Progress In Retinal Research 1993;12:179-204.

73. Bill A: A method to determine osmotically effective albumin and gammaglobulin concentrations in tissue fluids, its application to uvea and a note on effects of capillary "leaks" on tissue fluid dynamics. Acta Physiol Scand 1968;73:511-522.

74. Bill A: Blood circulation and fluid dynamics in the eye. Physiol Rev 1975;55:383-417.

75. Emi K, Pederson JE, Toris CB: Hydrostatic pressure of the suprachoroidal space. Invest Ophthalmol Vis Sci 1989;30:233-238.

76. Mannermaa E, Vellonen KS, Urtti A: Drug transport in corneal epithelium and blood-retina barrier: Emerging role of transporters in ocular pharmacokinetics. Adv Drug Deliv Rev 2006;58:1136-1163.

77. Dey S, Mitra AK: Transporters and receptors in ocular drug delivery: opportunities and challenges. Expert Opin Drug Deliv 2005;2:201-204.

78. Attar M, Shen J, Ling KH, Tang-Liu D: Ophthalmic drug delivery considerations at the cellular level: drug-metabolising enzymes and transporters. Expert Opin Drug Deliv 2005;2:891-908.

79. Kennedy BG, Mangini NJ: P-glycoprotein expression in human retinal pigment epithelium. Mol Vis 2002;8:422-430.

80. Steuer H, Jaworski A, Elger B, Kaussmann M, Keldenich J, Schneider H, Stoll D, Schlosshauer B: Functional characterization and comparison of the outer blood-retina barrier and the blood-brain barrier. Invest Ophthalmol Vis Sci 2005;46:1047-1053.

81. Aukunuru JV, Sunkara G, Bandi N, Thoreson WB, Kompella UB: Expression of multidrug resistance-associated protein (MRP) in human retinal pigment epithelial cells and its interaction with BAPSG, a novel aldose reductase inhibitor. Pharm Res 2001;18:565-572.

82. Cunha-Vaz JG, Maurice DM: The active transport of fluorescein by the retinal vessels and the retina. J Physiol 1967;191:467-486.

83. Maenpaa H, Gegelashvili G, Tahti H: Expression of glutamate transporter subtypes in cultured retinal pigment epithelial and retinoblastoma cells. Curr Eye Res 2004;28:159-165.

84. Miyamoto Y, Del Monte MA: Na(+)-dependent glutamate transporter in human retinal pigment epithelial cells. Invest Ophthalmol Vis Sci 1994;35:3589-3598.

85. Hillenkamp J, Hussain AA, Jackson TL, Cunningham JR, Marshall J: Taurine uptake by human retinal pigment epithelium: implications for the transport of small solutes between the choroid and the outer retina. Invest Ophthalmol Vis Sci 2004;45:4529-4534.

86. Sellner PA: The blood-retinal barrier: leucine transport by the retinal pigment epithelium. J Neurosci 1986;6:2823-2828.

87. Sellner PA: The movement of organic solutes between the retina and pigment epithelium. Exp Eye Res 1986;43:631-639.

88. Hillenkamp J, Hussain AA, Jackson TL, Constable PA, Cunningham JR, Marshall J: Compartmental analysis of taurine transport to the outer retina in the bovine eye. Invest Ophthalmol Vis Sci 2004;45:4099-4105.

89. Kundaiker S, Hussain AA, Marshall J: Component characteristics of the vectorial transport system for taurine in isolated bovine retinal pigment epithelium. J Physiol 1996;492 (Pt 2):505-516.

90. Zhang N, Kannan R, Okamoto CT, Ryan SJ, Lee VH, Hinton DR: Characterization of brimonidine transport in retinal pigment epithelium. Invest Ophthalmol Vis Sci 2006;47:287-294.

91. Ito A, Yamaguchi K, Tomita H, Suzuki T, Onogawa T, Sato T, Mizutamari H, Mikkaichi T, Nishio T, Suzuki T, Unno M, Sasano H, Abe T, Tamai M: Distribution of rat organic anion transporting polypeptide-E (oatp-E) in the rat eye. Invest Ophthalmol Vis Sci 2003;44:4877-4884.

92. Kumar G: Drug metabolizing enzyme systems in the eye. in Reddy I (ed): Ocular Therapeutics and Drug Delivery: A Multi-Disciplinary Approach. Technomic Publishing Company, Inc., 1996, 149-167.

93. Schwartzman ML, Masferrer J, Dunn MW, McGiff JC, Abraham NG: Cytochrome P450, drug metabolizing enzymes and arachidonic acid metabolism in bovine ocular tissues. Curr Eye Res 1987;6:623-630.

94. Shichi H, Nebert DW: Drug metabolism in ocular tissues. in Gram TE (ed): Extrahepatic Metabolism of Drugs and Other Foreign Compounds. MTP Press Limited, 1980, 333-363.

95. Duvvuri S, Majumdar S, Mitra AK: Role of metabolism in ocular drug delivery. Curr Drug Metab 2004;5:507-515.

96. Shichi H, Atlas SA, Nebert DW: Genetically regulated aryl hydrocarbon hydroxylase induction in the eye: possible significance of the drug-metabolizing enzyme system for the retinal pigmented epithelium-choroid. Exp Eye Res 1975;21:557-567.

97. Shichi H: Microsomal electron transfer system of bovine retinal pigment epithelium. Exp Eye Res 1969;8:60-68.

98. Wrighton SA, Thummel KE: CYP3A. in Levy RH, Thummel KE, Trager WF, et al. (eds): Metabolic Drug Interactions. Philadelphia: Lippincott Williams & Wilkins, 2000, 115-133.

99. Marshall J: The ageing retina: physiology or pathology. Eye 1987;1 (Pt 2):282-295.

100. Diment S, Eidelman M, Rodriguez GM, Orlow SJ: Lysosomal hydrolases are present in melanosomes and are elevated in melanizing cells. J Biol Chem 1995;270:4213-4215.

101. Hayasaka S: Lysosomal enzymes in ocular tissues and diseases. Surv Ophthalmol 1983;27:245-258.

102. Hayasaka S, Shiono T: alpha-Fucosidase, alpha-mannosidase and beta-N-acetylglucosaminidase of the bovine retinal pigment epithelium. Exp Eye Res 1982;34:565-569.

103. Lloyd JB: Lysosome membrane permeability: implications for drug delivery. Adv Drug Deliv Rev 2000;41:189-200.

104. Lloyd JB: Studies on the permeability of rat liver lysosomes to carbohydrates. Biochem J 1969;115:703-707.

105. Kim H, Robinson MR, Lizak MJ, Tansey G, Lutz RJ, Yuan P, Wang NS, Csaky KG: Controlled drug release from an ocular implant: an evaluation

using dynamic three-dimensional magnetic resonance imaging. Invest Ophthalmol Vis Sci 2004;45:2722-2731.

106. Li SK, Molokhia SA, Jeong EK: Assessment of subconjunctival delivery with model ionic permeants and magnetic resonance imaging. Pharm Res 2004;21:2175-2184.

107. Olsen TW, Feng X, Wabner K, Conston SR, Sierra DH, Folden DV, Smith ME, Cameron JD: Cannulation of the suprachoroidal space: a novel drug delivery methodology to the posterior segment. Am J Ophthalmol 2006;142:777-787.

108. Matthews JN, Altman DG, Campbell MJ, Royston P: Analysis of serial measurements in medical research. Bmj 1990;300:230-235.

109. Barza M, Kane A, Baum JL: Regional differences in ocular concentration of gentamicin after subconjunctival and retrobulbar injection in the rabbit. Am J Ophthalmol 1977;83:407-413.

110. Tsuji A, Tamai I, Sasaki K: Intraocular penetration kinetics of prednisolone after subconjunctival injection in rabbits. Ophthalmic Res 1988;20:31-43.

111. McCartney HJ, Drysdale IO, Gornall AG, Basu PK: An Autoradiographic Study Of The Penetration Of Subconjunctivally Injected Hydrocortisone Into The Normal And Inflamed Rabbit Eye. Invest Ophthalmol 1965;4:297-302.

112. Kim TW, Lindsey JD, Aihara M, Anthony TL, Weinreb RN: Intraocular distribution of 70-kDa dextran after subconjunctival injection in mice. Invest Ophthalmol Vis Sci 2002;43:1809-1816.

113. Barza M, Kane A, Baum J: Intraocular penetration of gentamicin after subconjunctibal and retrobulbar injection. Am J Ophthalmol 1978;85:541-547.

114. Langer O, Muller M: Methods to assess tissue-specific distribution and metabolism of drugs. Curr Drug Metab 2004;5:463-481.

115. Lanao JM, Fraile MA: Drug tissue distribution: study methods and therapeutic implications. Curr Pharm Des 2005;11:3829-3845.

116. Fischman AJ, Alpert NM, Babich JW, Rubin RH: The role of positron emission tomography in pharmacokinetic analysis. Drug Metab Rev 1997;29:923-956.

117. Fischman AJ, Alpert NM, Rubin RH: Pharmacokinetic imaging: a noninvasive method for determining drug distribution and action. Clin Pharmacokinet 2002;41:581-602.

118. Newman SP, Wilding IR: Imaging techniques for assessing drug delivery in man. Pharm Sci Technolo Today 1999;2:181-189.

119. Cherry SR: Fundamentals of positron emission tomography and applications in preclinical drug development. J Clin Pharmacol 2001;41:482-491.

120. Hustinx R, Eck SL, Alavi A: Potential applications of PET imaging in developing novel cancer therapies. J Nucl Med 1999;40:995-1002.

121. Dolovich M, Labiris R: Imaging drug delivery and drug responses in the lung. Proc Am Thorac Soc 2004;1:329-337.

122. Brunner M, Langer O, Dobrozemsky G, Muller U, Zeitlinger M, Mitterhauser M, Wadsak W, Dudczak R, Kletter K, Muller M: [18F]Ciprofloxacin, a new positron emission tomography tracer for noninvasive assessment of the tissue distribution and pharmacokinetics of ciprofloxacin in humans. Antimicrob Agents Chemother 2004;48:3850-3857.

123. Langer O, Mitterhauser M, Brunner M, Zeitlinger M, Wadsak W, Mayer BX, Kletter K, Muller M: Synthesis of fluorine-18-labeled ciprofloxacin for PET studies in humans. Nucl Med Biol 2003;30:285-291.

124. Hee MR, Izatt JA, Swanson EA, Huang D, Schuman JS, Lin CP, Puliafito CA, Fujimoto JG: Optical coherence tomography of the human retina. Arch Ophthalmol 1995;113:325-332.

125. Puliafito CA, Hee MR, Lin CP, Reichel E, Schuman JS, Duker JS, Izatt JA, Swanson EA, Fujimoto JG: Imaging of macular diseases with optical coherence tomography. Ophthalmology 1995;102:217-229.

126. Fujimoto JG: Optical coherence tomography for ultrahigh resolution *in vivo* imaging. Nat Biotechnol 2003;21:1361-1367.

127. Ettl A, Kramer J, Daxer A, Koornneef L: High resolution magnetic resonance imaging of neurovascular orbital anatomy. Ophthalmology 1997;104:869-877.

128. Richardson JC, Bowtell RW, Mader K, Melia CD: Pharmaceutical applications of magnetic resonance imaging (MRI). Adv Drug Deliv Rev 2005;57:1191-1209.

129. Berkowitz BA, Sato Y, Wilson CA, de Juan E: Blood-retinal barrier breakdown investigated by real-time magnetic resonance imaging after gadolinium-diethylenetriaminepentaacetic acid injection. Invest Ophthalmol Vis Sci 1991;32:2854-2860.

130. Arrindell EL, Wu JC, Wolf MD, Nanda S, Han DP, Wong EC, Abrams GW, Mieler WF, Hyde JS: High-resolution magnetic resonance imaging evaluation of blood-retinal barrier integrity following transscleral diode laser treatment. Arch Ophthalmol 1995;113:96-102.

131. Berkowitz BA, Roberts R, Luan H, Peysakhov J, Mao X, Thomas KA: Dynamic contrast-enhanced MRI measurements of passive permeability through blood retinal barrier in diabetic rats. Invest Ophthalmol Vis Sci 2004;45:2391-2398.

132. Plehwe WE, McRobbie DW, Lerski RA, Kohner EM: Quantitative magnetic resonance imaging in assessment of the blood-retinal barrier. Invest Ophthalmol Vis Sci 1988;29:663-670.

133. Ranta VP, Urtti A: Transscleral drug delivery to the posterior eye: prospects of pharmacokinetic modeling. Adv Drug Deliv Rev 2006;58:1164-1181.

134. Kim SH, Galban CJ, Lutz RJ, Dedrick RL, Csaky KG, Lizak MJ, Wang NS, Tansey G, Robinson MR: Assessment of subconjunctival and intrascleral drug delivery to the posterior segment using dynamic contrast-enhanced magnetic resonance imaging. Invest Ophthalmol Vis Sci 2007;48:808-814.

135. Huk WJ, Gademann G: Magnetic resonance imaging (MRI): method and early clinical experiences in diseases of the central nervous system. Neurosurg Rev 1984;7:259-280.

136. Lufkin RB: The MRI manual. ed 2nd, St. Louis, Mosby, 1998.

137. Gibby WA: MR contrast agents: an overview. Radiol Clin North Am 1988;26:1047-1058.

138. Berkowitz BA, Roberts R, Luan H, Bissig D, Bui BV, Gradianu M, Calkins DJ, Vingrys AJ: Manganese-enhanced MRI studies of alterations of intraretinal ion demand in models of ocular injury. Invest Ophthalmol Vis Sci 2007;48:3796-3804.

139. Kim SH, Csaky KG, Wang NS, Lutz RJ: Drug Elimination Kinetics Following Subconjunctival Injection Using Dynamic Contrast-Enhanced Magnetic Resonance Imaging. Pharm Res 2007.

140. Wehrli FW, Kanal E: Orbital imaging: factors determining magnetic resonance imaging appearance. Radiol Clin North Am 1987;25:419-427.

141. Reisfeld B, Blackband S, Calhoun V, Grossman S, Eller S, Leong K: The use of magnetic resonance imaging to track controlled drug release and transport in the brain. Magn Reson Imaging 1993;11:247-252.

142. Gomori JM, Grossman RI, Shields JA, Augsburger JJ, Joseph PM, DeSimeone D: Ocular MR imaging and spectroscopy: an *ex vivo* study. Radiology 1986;160:201-205.

143. Ambati J, Canakis CS, Miller JW, Gragoudas ES, Edwards A, Weissgold DJ, Kim I, Delori FC, Adamis AP: Diffusion of high molecular weight compounds through sclera. Invest Ophthalmol Vis Sci 2000;41:1181-1185.

144. Poukens V, Glasgow BJ, Demer JL: Nonvascular contractile cells in sclera and choroid of humans and monkeys. Invest Ophthalmol Vis Sci 1998;39:1765-1774.

145. Barathi A, Thu MK, Beuerman RW: Dimensional growth of the rabbit eye. Cells Tissues Organs 2002;171:276-285.

146. Bill A, Sperber G, Ujiie K: Physiology of the choroidal vascular bed. Int Ophthalmol 1983;6:101-107.

147. Bellows AR, Chylack LT, Jr., Hutchinson BT: Choroidal detachment. Clinical manifestation, therapy and mechanism of formation. Ophthalmology 1981;88:1107-1115.

148. Poole TA, Sudarsky RD: Suprachoroidal implantation for the treatment of retinal detachment. Ophthalmology 1986;93:1408-1412.

149. Mittl RN, Tiwari R: Suprachoroidal injection of sodium hyaluronate as an 'internal' buckling procedure. Ophthalmic Res 1987;19:255-260.

150. Stearns L, Boortz-Marx R, Du Pen S, Friehs G, Gordon M, Halyard M, Herbst L, Kiser J: Intrathecal drug delivery for the management of cancer pain: a multidisciplinary consensus of best clinical practices. J Support Oncol 2005;3:399-408.

151. Allen PJ, Nissan A, Picon AI, Kemeny N, Dudrick P, Ben-Porat L, Espat J, Stojadinovic A, Cohen AM, Fong Y, Paty PB: Technical complications and durability of hepatic artery infusion pumps for unresectable colorectal liver metastases: an institutional experience of 544 consecutive cases. J Am Coll Surg 2005;201:57-65.

152. Mehta V, Langford RM: Acute pain management for opioid dependent patients. Anaesthesia 2006;61:269-276.

153. Einmahl S, Savoldelli M, D'Hermies F, Tabatabay C, Gurny R, Behar-Cohen F: Evaluation of a novel biomaterial in the suprachoroidal space of the rabbit eye. Invest Ophthalmol Vis Sci 2002;43:1533-1539.

154. Olsen TW, Feng X, Wabner K, Conston SR, Sierra D, Chang TS, Smith M, Cameron JD: Microcannulation and Pharmacokinetics of Triamcinolone in the Suprachoroidal Space: A Novel Drug Delivery System to the Macula and Optic Nerve. Invest Ophthalmol Vis Sci 2006;47:ARVO E-Abstract 3882.

155. Gilger BC, Salmon JH, Wilkie DA, Cruysberg LP, Kim J, Hayat M, Kim H, Kim S, Yuan P, Lee SS, Harrington SM, Murray PR, Edelhauser HF, Csaky KG, Robinson MR: A novel bioerodible deep scleral lamellar cyclosporine implant for uveitis. Invest Ophthalmol Vis Sci 2006;In Press.

156. Luan H, Roberts R, Sniegowski M, Goebel DJ, Berkowitz BA: Retinal thickness and subnormal retinal oxygenation response in experimental diabetic retinopathy. Invest Ophthalmol Vis Sci 2006;47:320-328.

157. Alm A, Bill A, Young FA: The effects of pilocarpine and neostigmine on the blood flow through the anterior uvea in monkeys. A study with radioactively labeled microspheres. Exp Eye Res 1973;15:31-36.

158. Bill A, Stjernschantz J: Cholinergic vasoconstrictor effects in the rabbit eye: vasomotor effects of pentobarbital anesthesia. Acta Physiol Scand 1980;108:419-424.

159. Peiffer RL, Pohm-Thorsen L, Corcoran K: Models in Ophthalmology and Vision Research. in Manning PJ, Ringler DH, Newcomer CE (eds): The Biology of the Laboratory Rabbit. San Diego: Academic Press, 1994, 409-433.

160. Taylor JS, Reddick WE: Evolution from empirical dynamic contrast-enhanced magnetic resonance imaging to pharmacokinetic MRI. Adv Drug Deliv Rev 2000;41:91-110.

161. Roberts TP: Physiologic measurements by contrast-enhanced MR imaging: expectations and limitations. J Magn Reson Imaging 1997;7:82-90.

162. Wilson CA, Benner JD, Berkowitz BA, Chapman CB, Peshock RM: Transcorneal oxygenation of the preretinal vitreous. Arch Ophthalmol 1994;112:839-845.

163. Wilson CA, Berkowitz BA, Sato Y, Ando N, Handa JT, de Juan E, Jr.: Treatment with intravitreal steroid reduces blood-retinal barrier breakdown due to retinal photocoagulation. Arch Ophthalmol 1992;110:1155-1159.

164. Viglianti BL, Abraham SA, Michelich CR, Yarmolenko PS, MacFall JR, Bally MB, Dewhirst MW: *In vivo* monitoring of tissue pharmacokinetics of liposome/drug using MRI: illustration of targeted delivery. Magn Reson Med 2004;51:1153-1162.

165. Basilion JP, Yeon S, Botnar R: Magnetic resonance imaging: utility as a molecular imaging modality. Curr Top Dev Biol 2005;70:1-33.

166. Gaudio PA: A review of evidence guiding the use of corticosteroids in the treatment of intraocular inflammation. Ocul Immunol Inflamm 2004;12:169-192.

167. Morris RJ, McLeod D, Gregor ZJ: Subconjunctival injections of antibiotics are used increasingly at the conclusion of intraocular and extraocular procedures. Eye 1989;3 (Pt 6):860-861.

168. Weijtens O, Feron EJ, Schoemaker RC, Cohen AF, Lentjes EG, Romijn FP, van Meurs JC: High concentration of dexamethasone in aqueous and vitreous after subconjunctival injection. Am J Ophthalmol 1999;128:192-197.

169. Kalina PH, Erie JC, Rosenbaum L: Biochemical quantification of triamcinolone in subconjunctival depots. Arch Ophthalmol 1995;113:867-869.

170. Maurice DM, Ota Y: The kinetics of subconjunctival injections. Jpn J Ophthalmol 1978;22:95-100.

171. Suomalainen VP: Comparison of retinal lesions produced by transscleral krypton laser photocoagulation, transpupillar krypton laser photocoagulation and cryocoagulation. Acta Ophthalmol (Copenh) 1993;71:224-229.

172. Friedrichsen EJ, Chevez-Barrios P, Keener M, Garcia CA: Immunohistochemical comparison of transscleral continuous wave 1064-Nd:YAG laser retinopexy and cryoretinopexy. Retina 1994;14:51-58.

173. Supersaxo A, Hein WR, Steffen H: Effect of molecular weight on the lymphatic absorption of water-soluble compounds following subcutaneous administration. Pharm Res 1990;7:167-169.

174. McLennan DN, Porter CJH, Charman SA: Subcutaneous drug delivery and the role of the lymphatics. Drug Discovery Today: Technologies 2005;2:89.

175. Samuels LD: Lymphoscintigraphy. Lymphology 1987;20:4-9.

176. Nawaz MK, Hamad MM, Abdel-Dayem HM, Sadek S, Eklof BG: Tc-99m human serum albumin lymphoscintigraphy in lymphedema of the lower extremities. Clin Nucl Med 1990;15:794-799.

177. Pain SJ, Nicholas RS, Barber RW, Ballinger JR, Purushotham AD, Mortimer PS, Peters AM: Quantification of lymphatic function for investigation of lymphedema: depot clearance and rate of appearance of soluble macromolecules in blood. J Nucl Med 2002;43:318-324.

178. Warner GF, Dobson EL, Pace N, Johnston ME, Finney CR: Studies of human peripheral blood flow; the effect of injection volume on the intramuscular radiosodium clearance rate. Circulation 1953;8:732-734.

179. Sund RB, Schou J: The Determination Of Absorption Rates From Rat Muscles: An Experimental Approach To Kinetic Descriptions. Acta Pharmacol Toxicol (Copenh) 1964;21:313-325.

180. Blaser J, Rieder HL, Luthy R: Interface-area-to-volume ratio of interstitial fluid in humans determined by pharmacokinetic analysis of netilmicin in small and large skin blisters. Antimicrob Agents Chemother 1991;35:837-839.

181. Hirano K, Ichihashi T, Yamada H: Studies on the absorption of practically water-insoluble drugs following injection V: Subcutaneous absorption in rats from solutions in water immiscible oils. J Pharm Sci 1982;71:495-500.

182. Marra M, Gukasyan HJ, Raghava S, Kompella UB: 2nd Ophthalmic Drug Development and Delivery Summit. Expert Opin Drug Deliv 2007;4:77-85.

183. Atkinson AJ: Principles of clinical pharmacology. San Diego, Calif., Academic Press, 2001.

184. Bakri SJ, Snyder MR, Reid JM, Pulido JS, Singh RJ: Pharmacokinetics of intravitreal bevacizumab (Avastin). Ophthalmology 2007;114:855-859.

185. Lee TW, Robinson JR: Drug delivery to the posterior segment of the eye: some insights on the penetration pathways after subconjunctival injection. J Ocul Pharmacol Ther 2001;17:565-572.

186. Lee TW, Robinson JR: Drug delivery to the posterior segment of the eye II: development and validation of a simple pharmacokinetic model for subconjunctival injection. J Ocul Pharmacol Ther 2004;20:43-53.

187. Lee TW, Robinson JR: Drug delivery to the posterior segment of the eye III: the effect of parallel elimination pathway on the vitreous drug level after subconjunctival injection. J Ocul Pharmacol Ther 2004;20:55-64.

188. Mac Gabhann F, Demetriades AM, Deering T, Packer JD, Shah SM, Duh E, Campochiaro PA, Popel AS: Protein transport to choroid and retina following

periocular injection: theoretical and experimental study. Ann Biomed Eng 2007;35:615-630.

189. Friedrich S, Cheng YL, Saville B: Drug distribution in the vitreous humor of the human eye: the effects of intravitreal injection position and volume. Curr Eye Res 1997;16:663-669.

190. Friedrich S, Cheng YL, Saville B: Finite element modeling of drug distribution in the vitreous humor of the rabbit eye. Ann Biomed Eng 1997;25:303-314.

191. Marmor MF, Wolfensberger TJ: The retinal pigment epithelium: function and disease. New York, Oxford University Press, 1998.

192. Koornneef L: Details of the orbital connective tissue system in the adult. Acta Morphol Neerl Scand 1977;15:1-34.

193. Fatt I, Hedbys BO: Flow of water in the sclera. Exp Eye Res 1970;10:243-249.

194. Linde B, Chisolm G: The interstitial space of adipose tissue as determined by single injection and equilibration techniques. Acta Physiol Scand 1975;95:383-390.

195. Tsuboi S, Fujimoto T, Uchihori Y, Emi K, Iizuka S, Kishida K, Manabe R: Measurement of retinal permeability to sodium fluorescein in vitro. Invest Ophthalmol Vis Sci 1984;25:1146-1150.

196. Albanese RA, Banks HT, Evans MV, Potter LK: Physiologically based pharmacokinetic models for the transport of trichloroethylene in adipose tissue. Bull Math Biol 2002;64:97-131.

197. Dickinson AJ, Gausas RE: Orbital lymphatics: do they exist? Eye 2006;20:1145-1148.

198. Welling PG: Pharmacokinetics: processes and mathematics. Washington, DC, American Chemical Society, 1986.

199. Kety SS: The theory and applications of the exchange of inert gas at the lungs and tissues. Pharmacol Rev 1951;3:1-41.

200. Renkin EM: Effects of blood flow on diffusion kinetics in isolated, perfused hindlegs of cats; a double circulation hypothesis. Am J Physiol 1955;183:125-136.

201. Crone C: The Permeability Of Capillaries In Various Organs As Determined By Use Of The 'Indicator Diffusion' Method. Acta Physiol Scand 1963;58:292-305.

202. Bill A, Tornquist P, Alm A: Permeability of the intraocular blood vessels. Trans Ophthalmol Soc U K 1980;100:332-336.

203. Hogan MJ, Alvarado JA, Weddell JE: Histology of the human eye; an atlas and textbook [by] Michael J. Hogan, Jorge A. Alvarado [and] Joan Esperson Weddell. Philadelphia, Saunders, 1971.

204. Tornquist P, Alm A, Bill A: Permeability of ocular vessels and transport across the blood-retinal-barrier. Eye 1990;4 (Pt 2):303-309.

205. Watson PD: Permeability of cat skeletal muscle capillaries to small solutes. Am J Physiol 1995;268:H184-193.

206. Rowland M, Tozer TN: Clinical pharmacokinetics, concepts and applications. Philadelphia, Lea & Febiger, 1980.

207. Ueda H, Horibe Y, Kim KJ, Lee VH: Functional characterization of organic cation drug transport in the pigmented rabbit conjunctiva. Invest Ophthalmol Vis Sci 2000;41:870-876.

208. Paaske WP, Nielsen SL: Capillary permeability in adipose tissue. Acta Physiol Scand 1976;98:116-122.

209. Ghate D, Brooks W, McCarey BE, Edelhauser HF: Pharmacokinetics of intraocular drug delivery by periocular injections using ocular fluorophotometry. Invest Ophthalmol Vis Sci 2007;48:2230-2237.

210. Kim JW, Lindsey JD, Wang N, Weinreb RN: Increased human scleral permeability with prostaglandin exposure. Invest Ophthalmol Vis Sci 2001;42:1514-1521.

211. Weinreb RN: Enhancement of scleral macromolecular permeability with prostaglandins. Trans Am Ophthalmol Soc 2001;99:319-343.

212. Amrite AC, Ayalasomayajula SP, Cheruvu NP, Kompella UB: Single periocular injection of celecoxib-PLGA microparticles inhibits diabetes-induced elevations in retinal PGE2, VEGF, and vascular leakage. Invest Ophthalmol Vis Sci 2006;47:1149-1160.

213. Nicholson C: Diffusion and related transport mechanisms in brain tissue. Reports On Progress In Physics 2001;64:815-884.